Exponential asymptotics and homoclinic snaking

Andrew Dean, MMath

Thesis submitted to the University of Nottingham

for the degree of Doctor of Philosophy

December 2012

Abstract

There is much current interest in systems exhibiting homoclinic snaking, in which solution curves of localised patterns snake back and forth within a narrow region of parameter space. Such solutions comprise superimposed, back-to-back stationary fronts, each front connecting a homogeneous and a patterned state. These fronts are pinned to the underlying pattern within the snaking region; elsewhere, they become travelling waves and cannot form localised solutions. Application of standard asymptotic techniques near bifurcation can only produce a stationary front at the centre of the snaking region; this is the Maxwell point, where patterned and homogeneous states are equally energetically favourable. Such methods fail to capture the pinning mechanism because it is an exponentially small effect, and must be studied using exponential asymptotics. Deriving the late terms in the asymptotic expansion and observing that it is divergent, we truncate optimally after the least term. The resultant remainder is exponentially small and governed by an inhomogeneous differential equation. Rescaling this equation near Stokes lines—lines in the complex plane at which forcing is maximal—we observe a smooth but rapid increase from zero to exponentially small in the coefficient of an exponentially growing complementary function as Stokes lines are crossed. Requiring that unbounded terms vanish fixes the phase of the underlying pattern relative to the leading-order front. Furthermore, matching two fronts together produces a set of formulae describing the snaking bifurcation diagram. We successfully apply this method to continuous and discrete systems. In the former, we also show how symmetric solutions comprising two localised patches form figure-of-eight isolas in the bifurcation diagram. In the latter, we investigate snaking behaviour of a one-dimensional localised solution rotated into a square lattice, and find that the snaking region vanishes when the tangent of the angle of orientation is irrational.

Acknowledgements

The writing of this thesis has proved a mammoth task, one which I would not have achieved without the help and support of so many people. I would first like to thank my supervisors, Paul Matthews, Stephen Cox and John King, for their immensely valuable advice, brilliant insight, willingness to proof-read and patient good humour throughout my studies. My friends and family are a constant source of joy in my life; to them I offer a heartfelt thank you. My most effusive thanks I reserve for my beautiful wife, who has supported and encouraged me every step of the way. Anna, thank you for your love, compassion and unwavering belief in me. This thesis is dedicated to you.

Contents

CHAPTER 1

Introduction

Patterns are ubiquitous throughout nature. From convection to animal coat markings to neural firing, vastly disparate physical situations often produce qualitatively very similar results. This observation has motivated the field of theoretical research known as pattern formation. Mathematically speaking, this concerns the emergence of spatially periodic structures in a previously homogeneous system as a control parameter is increased. One particularly famous physical example is Rayleigh-Bénard convection, in which a layer of fluid is heated from below. When the temperature gradient across the fluid is low, heat is conducted from the lower to the upper boundary and there is no bulk flow of fluid. However, once the temperature gradient increases past a certain value, fluid at the lower boundary begins to rise. As it rises, it cools and becomes more dense, in turn causing it to sink. This competition between rising and sinking fluid thus forms a patterned state of spatially repeating convective rolls. Other theoretical and physical examples of pattern formation abound in the literature; a good starting point is the review by Cross and Hohenberg [33]. An introduction to the more common analytical methods used can be found in the book by Hoyle [46].

There has been considerable focus in recent years on localised patterns [18, 37, 52], in which a patterned region is embedded within the homogeneous state, rather than filling the whole domain. Under certain conditions, a multiplicity of these exists within a

well-defined parameter range. The interweaving solution curves 'snake' back and forth within this parameter range via successive saddle-node bifurcations, the width of the localised patch increasing as the curve is traversed. The two snaking curves represent symmetric solutions, and are connected by a succession of 'rungs', or branches of asymmetric solutions. Hence the phenomenon is often referred to as a 'snakes-and-ladders' bifurcation [14]. The alternative nomenclature 'homoclinic snaking' is also used, drawing an analogy between the profile of the localised solution and the homoclinic orbits of dynamical systems theory [96].

Localised patterns and homoclinic snaking have been observed in numerous experimental and theoretical contexts, including optics [26, 42, 73, 86, 92, 99, 100], convection in binary mixtures [3, 71], ferrofluids [75], Couette flow [81], reaction-diffusion systems [60, 91], vibrated granular layers [88, 95], magnetoconvection [8, 34], buckling problems [47], mathematical neuroscience [30, 58, 59, 80] and convection with temperature-dependent viscosity [82]. A specific example of the phenomenon is shown in figure 1.1, with a close-up of the snakes-and-ladders structure, and example patterns from various points in the diagram are shown in figure 1.2. The two figures are the results of numerical computations of a well-known paradigm of pattern formation, the Swift-Hohenberg equation (SHE),

$$\frac{\partial u}{\partial t} = ru - \left(1 + \frac{\partial^2}{\partial x^2}\right)^2 u + su^3 - u^5, \tag{1.0.1}$$

given here in its one-dimensional form with cubic and quintic nonlinearities; variants of (1.0.1) abound in the literature. Originally conceived as a simple model of hydrodynamic fluctuations in convection [84], the SHE is also relevant to nonlinear optics, mathematical neuroscience and structural mechanics, but is nowadays most commonly studied in its own right as a generic model of pattern formation [33]. Indeed, one of the most extensively studied examples of homoclinic snaking is in the SHE [13]; to our knowledge, the first study of localised states in the specific variant (1.0.1) was performed by Sakaguchi and Brand [78], although they did not discuss the snaking effect.

Model equations such as the SHE have the advantage that they are simple enough to be amenable to relatively detailed analysis, while retaining the same qualitative pattern-forming features observed in more realistic systems or experiments. This is in contrast to pattern-forming systems in general, and those exhibiting homoclinic snaking in particular, which are invariably modelled by rather more complicated systems. It is therefore instructive to study generic pattern-forming processes by means of model equations; hence the prevalence of the SHE in the literature. Such work provides significant insight into the mechanisms whereby patterns come into being, which would be impossible to come by should analysis be confined only to more physically realistic, but also more complicated, systems. For this reason, our focus throughout the thesis shall be on homoclinic snaking in model equations.

We shall now describe the snakes-and-ladders bifurcation structure in more detail, concentrating on the simplest, and hence most widely studied, case of spatial oscillations which are localised in one spatial direction only. Of course, many of the examples above are inherently two- or three-dimensional, if not also time-dependent, but for the sake of simplicity we shall only mention these in passing. Much of the current understanding is due to work by Burke and Knobloch [12–14], the bulk of which has been carried out numerically in various forms of the SHE, underpinned by an intuitive picture given by Pomeau [74]. This picture was formalised in a dynamical systems context by Woods and Champneys [96], and more recently by Beck *et al*. [4]. Further insight was provided by the analysis of Kozyreff and Chapman [56], in which the method of exponential asymptotics was used to describe explicitly the exponentially small effects responsible for the snaking bifurcation diagram; we shall expound upon this in more detail later. Some results are available in higher dimensions, most notably for localised hexagons, spots and rings on the plane [2, 61, 62, 68, 69, 90], and oscillons, objects which are localised in space and oscillatory in time [16, 38]; on the whole, however, current understanding of higher-dimensional phenomena is much less well developed than in

the one-dimensional case.

In the one-dimensional SHE, for example as in figure 1.1, the solution curves originate at a pair of subcritical pitchfork bifurcations from the spatially periodic branch. The bifurcation point is near the origin, arbitrarily close as the domain length tends towards infinity, where the set of allowable wavenumbers becomes a continuum. These secondary solution branches form slightly modulated spatial oscillations, which increase in amplitude as r decreases, while at the same time becoming more and more localised. When the amplitude is equal to that of the stable, constant amplitude branch, the curves turn over via a saddle-node bifurcation and begin to snake. The two curves interweave, repeatedly turning back at successive saddle-nodes. The position of the saddle-nodes rapidly tends to one of two asymptotes in parameter space, so the branches occupy a well-defined parameter range. Close to each saddle-node is a secondary pitchfork bifurcation, producing the so-called 'rungs' which link the snakes [14]. The snakes describe localised patterns which preserve some symmetry of the governing system, while the ladders consist of asymmetric solutions. For example, equation (1.0.1) is invariant under $u \to -u$ and $x \to -x$. In this case, each snake actually represents a pair of solution curves related by the symmetry $u \to -u$; one pair comprises even solutions and the other odd. As the snakes are traversed, a new pair of humps is added for each fold, one hump at each end of the patterned region. In this way the localised patch grows in extent as the snaking curve is traversed. Other growth mechanisms have also been observed; for example, in parametrically driven systems localised solutions grow according to a central defect which inserts an additional hump, pushing existing humps outward [64]. Although initially unstable, the snaking solutions become stable at the first saddle-node, after which they alternate between stability and instability with each successive saddle-node [13]. The ladders are always unstable in one dimension, although this no longer necessarily holds in two dimensions [2]. Similar snakes-and-ladders structures to those of the SHE are also observed in more physically

realistic applications [3, 47, 81, 99].

The localised patterns which form the snakes-and-ladders bifurcation can be thought of as superpositions of two back-to-back fronts connecting the homogeneous state to the patterned, as seen in figure 1.2, for example; this of course requires both states to be stable solutions of the pertinent system. Such a bistable region can be seen in figure 1.1, in this case due to a subcritical pitchfork bifurcation at $r = 0$ to small-amplitude spatial oscillations, followed by a saddle-node at some $r < 0$ at which the patterned solution branch turns over and becomes stable. The snaking bifurcation diagram then occupies a much narrower parameter range within the bistable region. Snaking is not seen throughout the entire bistability region because bistability itself is not sufficient; the two different solutions must be almost equally 'energetically preferred', in some sense. In variational systems such as the SHE, this is easily understood in terms of a Lyapunov functional, or 'energy' [13, 78]. Stable solutions correspond to minima of this functional, and so a front connecting two stable states will in general move so that the state with lower energy 'wins out' over the other; if the two states have equal energy the front will remain stationary. This suggests a more general way to describe such a phenomenon which does not rely upon a variational structure, and can be traced back to Pomeau [74]. In a bistable system, a travelling wave solution may be sought between the two states. When the velocity of the wave is non-zero, one pattern is preferred over the other, and the less favoured vanishes. However, a point exists where the wave velocity is zero and there is no preference, corresponding to the two states in a variational system possessing equal energy. In this case the solution is a stationary front and both patterns persist. Such a point is known as the Maxwell point.

At the Maxwell point, localised patterns may therefore be constructed from two back-to-back fronts; away from the Maxwell point, fronts become travelling waves and the localised patch either expands to fill the domain or contracts and is destroyed, depending upon which state is preferred by the system [12, 78]. However, for a small

enough perturbation of the system from the Maxwell point, fronts lack sufficient velocity to overcome the energy barrier posed by the underlying spatial oscillations and are 'pinned' to the underlying pattern [74]. This pinning occurs by means of an interaction between the slow scale of the pattern amplitude and the fast scale of its frequency, resulting in a fixing of the phase [12, 39, 56]. Thus localised patterns exist within a small region [78] centred on the Maxwell point, organised into a snakes-and-ladders bifurcation structure [13]. We note that snaking also occurs in discrete systems [26, 85, 99, 100]. In this case an energy barrier is posed by the underlying lattice; sufficiently close to the Maxwell point a front cannot overcome this barrier and becomes pinned, fixing its origin with respect to the lattice [40, 51].

We have heretofore not mentioned the effects of boundaries on snaking, and implicitly assumed an infinite system in which the width of a localised patch can increase indefinitely. This is obviously not the case when a system is finite, and in general the snakes exit the snaking region when the localised patch is close to filling the domain and reconnect onto a branch of uniform amplitude oscillations [6, 36]. However, even distant boundaries can have a marked effect on the snaking structure. With periodic boundaries (or Neumann boundaries, which can be embedded in a periodic domain of twice the length), the situation is similar to that in an infinite domain, and in fact provide a good approximation to behaviour on the real line provided the localised patch is sufficiently far from the boundaries. Under more general conditions without translational invariance, the position of the pattern relative to the boundaries becomes an important consideration and follows a complicated bifurcation sequence as the pattern width varies [55].

In fact, boundary conditions can have even more profound consequences than these. Although we have thus far discussed the snaking bifurcation diagram in the context of a bistable system, bistability is not strictly a requisite for snaking to occur. This was first observed by Mercader *et al*. in binary fluid convection with physically realistic bound-

ary conditions [71], and later studied in the SHE by Houghton and Knobloch [45]. If non-Neumann boundary conditions are imposed (such as $u_x = \pm\beta u$ and $u_{xxx} = 0$ on the boundaries $x = \pm D$, as in [45]), there is no uniform amplitude branch since it violates the boundary conditions. Therefore the system is not bistable and there is no uniform amplitude branch for the snaking curve to reconnect to when the localised patch approaches the domain boundaries. Two possible scenarios were observed in [45]. First, the snaking curve may leave the snaking region to the right; the pattern amplitude then begins to increase, modulated slightly at the boundaries in order to accommodate the imposed conditions, and the solution branch propagates indefinitely. Alternatively, a snaking curve may turn back over and retrace its steps, sometimes several times, before reconnecting to the trivial branch. That said, the systems under consideration in [45] and [71] do exhibit bistability between the zero and uniform amplitude solution branches under different boundary conditions, and so these examples of homoclinic snaking without bistability are not completely unrelated to the snaking picture described above.

We should at this point note that not all localised patterns snake. For example, non-snaking localisations have been observed in systems which are coupled to an advected field [76, 77] or a conservation law [32, 66]; in both cases the localised patterns are not constructed from back-to-back fronts and so arise due to a different mechanism than that discussed above. A trivial example of localised solutions which do not snake in the SHE are those constructed from fronts connecting two constant solutions; the absence of spatial oscillations means there is no structure for the fronts to pin to, hence no snaking [2].

We have thus far considered only the simplest systems exhibiting homoclinic snaking. These are reversible in x, variational in time and conservative in space; (1.0.1) is a typical example. However, snaking is also observed in systems without such properties [11, 99]. In irreversible systems, which do not obey the symmetry $x \to -x$, the snakes-

and-ladders diagram either breaks up into stacks of figure-of-eight isolas or forms two criss-crossing snakes [54, 79]; if the conservative nature of the system is also broken the resultant localised states drift [11]. There remains much to be done in elucidating the nonvariational and nonconservative cases, with current understanding limited to initial normal-form analyses of this much more complicated problem [10].

Even in simple one dimensional systems like (1.0.1), the snaking region is rather complex. As multi-pulse solutions can be thought of as superpositions of multiple patches of spatial oscillations, the ideas discussed so far can readily be extended to cover them [15]. Many such solutions exist, infinitely many on an infinite domain, each with their own solution curve. Depending on the symmetries of the solution, and the gap between localised patches, these are described by separate snakes, or isolas in the style of a figure of eight. Furthermore, the snaking width is not necessarily constant, and has been observed under certain conditions to decay exponentially as the localised patch increases in extent, a situation known as collapsed snaking [2, 64, 99, 100]. The situation is even worse in two dimensions, with multiple snaking widths and even more isolas [61, 62].

In an effort to further elucidate the snaking process, there have been several attempts over the past two decades to apply analytical methods to the problem. One approach which has been especially fruitful in the one-dimensional case is that of spatial dynamics, in which the steady version of (1.0.1), for example, is thought of as a fourth-order dynamical system, or a system of four first-order ordinary differential equations in the elements of $\mathbf{u} = (u, u_x, u_{xx}, u_{xxx})$ [31, 47, 96]. In this formulation the spatial variable x takes the role traditionally reserved for time. If the origin ($\mathbf{u} = \mathbf{0}$) has both stable and unstable manifolds, and there exists a heteroclinic connection from the origin to a periodic orbit, then the reversibility of the SHE in x guarantees the existence of a homoclinic connection from the origin via said periodic orbit [4]. A localised pattern can therefore be described in terms of an orbit which departs the origin on its unsta-

ble manifold and circles a periodic solution a certain number of times before returning along its stable manifold. Thus localised spatial oscillations can be constructed.

Although extremely useful in elucidating the snakes-and-ladders structure in phase space, such analysis is only able to provide a conceptual explanation of the phenomenon. In addition, there does not seem to be any way to extend dynamical systems techniques to higher dimensions or non-autonomous systems, although some progress can be made when stripes are localised in one direction only [2], and other analytic techniques have been employed to study radially symmetric spots and target patterns [61, 68].

The method of multiple scales provides one promising avenue of research, and has proven very successful in describing other patterns, such as rolls and hexagons close to onset [33]. Crucially, it is not limited to one-dimensional problems. Indeed, since localised solutions have been observed in the Ginzburg-Landau equation [41], various attempts have been made to include the phase-locking responsible for homoclinic snaking within existing calculations. The shortcoming of conventional multiple-scales analysis is that it fails to capture the snaking region, as front solutions can be found only at the Maxwell point. Because the inherent assumption within the method of multiple scales is that the fast and slow scales are independent, the phase-locking of one scale to the other can never be derived by this approach alone. Moreover, the snaking region is in fact exponentially small and therefore unobservable by conventional asymptotic methods based purely on algebraically small terms.

Initial attempts to overcome these difficulties focused on the inclusion of the phase locking between the two scales within the conventional multiple-scales analysis at algebraic orders [5, 28]. The leading-order solution is written, as usual, to be of the form $A(X)e^{ix+i\phi} + A^*(X)e^{-ix-i\phi}$, where x is the fast scale, X the slow scale, ϕ some constant phase and the asterisk represents the complex conjugate. At some order in the multiple-scales expansion a solvability condition determining $A(X)$ is found by imposing that

secular, or resonant, terms vanish. This is in agreement with the usual multiple-scales theory. At this point, some authors [5, 28] have tried to include non-secular terms in the solvability condition, i.e. terms such as e^{3ix}, e^{5ix}, etc. Rescaling the fast scale in terms of the slow, these become exponentially small corrections, and in this way an equation describing the position of a front or the distance between back-to-back fronts can be derived, with constant solutions existing within an exponentially small parameter range.

However, such a method gives rise only to one snaking curve, whereas numerical computations have invariably shown two. Additionally, an algebraically small prefactor in the exponentially small width of the snaking region is missed. The most telling argument against this method, though, is that there is little justification for shoehorning non-secular terms into the solvability condition [29, 57]. While this remains a worthwhile attempt to take account of the pinning mechanism, and does provide some insight into how the pinning region may be created, the key step that produces the desired results is unfounded. The effects of phase-locking are not felt at algebraic orders; one must go beyond all orders to find them.

The method of exponential asymptotics, or asymptotics beyond-all-orders, arises when studying divergent asymptotic expansions, such as those produced by singular perturbation problems [1, 7, 21, 72]. Divergent expansions must be truncated; by truncating optimally after the least term, the resultant remainder can be shown to be exponentially small. Crucial information governing the leading-order solution is encoded within the remainder—in the present concern of homoclinic snaking, the phase of the underlying pattern relative to the front is fixed beyond all orders in this manner [22, 39, 40, 56].

The method was initially motivated by, and is intimately related to, Stokes' phenomenon. This is the observation that asymptotic expansions of certain integrals, for example integral representations of the error function or Airy function [7, 72], contain contributions whose coefficient (the Stokes multiplier) abruptly changes from zero to

non-zero as certain lines in the complex plane (the Stokes lines) are crossed. Thus a continuous function appears to be given by a discontinuous asymptotic expansion. In fact, a careful analysis of exponentially small terms in the tail of the asymptotic expansion shows that this change in coefficient is not discontinuous at all. Instead, the coefficient varies smoothly and rapidly within a narrow layer centred on the Stokes layer. This rapid variation is only observable through appropriate rescaling; away from the Stokes line the coefficient appears to be piecewise constant. This was first shown, in the context of the complex error function, by Berry [7], and later made rigorous by McLeod [70]. The smooth variation of the coefficient between zero and non-zero values was found to take place via an error function; this is the usual, although not generic [19], form the smoothing takes.

The method was soon applied to differential equations, and found to be useful in elucidating problems involving water-waves [87, 89], shocks [20], flow past submerged steps [24, 25, 63] and travelling waves in discrete [51] and continuous [1] systems. In such applications, Stokes' phenomenon manifests as the 'switching on' of certain contributions to the remainder of an asymptotic expansion solution, in the sense that their coefficients vary smoothly from zero to non-zero (albeit exponentially small) as Stokes lines are crossed. For example, in flow past a submerged step, exponentially small surface waves exist downstream, but not upstream, of the step. Such behaviour cannot be observed using asymptotic techniques based solely on algebraically small quantities.

The first rigorous asymptotic analysis of the snaking phenomenon was carried out by Kozyreff and Chapman [22, 56] in the context of the SHE with quadratic and cubic nonlinearities, following the beyond-all-orders techniques of [1]. Extension of these methods to other snaking problems forms the subject matter of this thesis; some of our results have either been published [39] or are under review [40]. Similar ideas involving Fourier transforms have been used in [93, 94] following the methods developed in [17, 97, 98]; some outstanding technicalities are addressed in [49]. However, although the

subject of these studies is localised wavepackets, and phase-locking is observed, the objects under consideration take the form of sech-like profiles, rather than back-to-back fronts. Consequently, the analysis is relevant to slowly modulated patterns before the onset of snaking, not the snaking solutions themselves. Moreover, it is not clear from the methods used precisely what the phase-locking mechanism is; the method first used by Kozyreff and Chapman is more transparent.

Briefly, the method is as follows. The observation that a leading-order front solution is singular at certain points in the complex plane, coupled with the fact that the perturbation problem is singular (i.e. that the highest derivative does not contribute at leading order) leads to the conclusion that the asymptotic expansion is divergent and must be truncated. If the point of truncation is chosen to be at the least term, the resultant remainder turns out to be exponentially small. Evaluating the remainder therefore allows exponentially small effects to be analysed explicitly. The forcing of the remainder equation is exponentially small but maximal at Stokes lines. By rescaling near the Stokes lines, the switching on of an exponentially growing complementary function is observed, with the undesirable consequence of a non-uniform asymptotic expansion. This can only be avoided by fixing the phase of the underlying oscillations in terms of a deviation from the Maxwell point; real solutions exist only within an exponentially small parameter range. Thus the phase-locking mechanism giving rise to the existence of fronts in parameter range centred on the Maxwell point is observed. Furthermore, by matching two back-to-back fronts, a set of equations can be derived which describes the full snakes-and-ladders bifurcation diagram.

The main drawback of the work by Kozyreff and Chapman is the lack of a quantitative comparison with numerical results. This is due to the fact that although the exponentially small scaling of the Stokes multiplier can be derived analytically, it remains defined in terms of an analytically undeterminable $\mathrm{O}(1)$ constant. This is a consequence of the linear nature of higher-order contributions to the asymptotic calculation,

and also appears in the similar methods based on Fourier transforms, e.g. [93, 98]. However, there does exist a recurrence relation from which the Stokes multiplier may be determined to a good degree of accuracy, if solved to a high enough iteration. In the quadratic-cubic SHE this is computationally very expensive, and so Kozyreff and Chapman relied instead on a numerical best-fit approximation. Thus their numerical comparison is not entirely convincing. In the problems studied in later chapters, and others, e.g. [1, 51], such compromises are unnecessary as the recurrence relation is relatively cheap to solve to high order, and rigorous numerical checks may be carried out.

In the following chapters we shall employ the method of exponential asymptotics in the analysis of various snaking scenarios. We begin in Chapter 2 by describing Stokes' phenomenon in more detail, and provide an introduction to the exponential asymptotic method via the particular example of the exponential integral. In Chapter 3 we describe how the method of multiple scales may be used to analyse pattern-formation in the SHE, and illustrate why such conventional methods fail to capture snaking behaviour. Then, in Chapter 4 we apply exponential asymptotics to the cubic-quintic SHE to derive a full asymptotic description of a stationary front solution; in particular, we are able to observe explicitly the pinning of the front to the underlying spatial oscillations, and thus obtain a formula for the width of the snaking region. This allows us to match back-to-back fronts together in Chapter 5, resulting in a set of formulae describing the full snakes-and-ladders bifurcation diagram. We also extend this process to match two localised patches together to form multi-pulse solutions, and show how these form isolas in the bifurcation diagram. At this point we switch our focus from continuous systems to discrete ones. Chapter 6 comprises an exponential asymptotic study of steady solutions to a differential-difference equation on a square lattice which are localised in a single spatial direction. Through a similar approach to that used in Chapters 4-5, we are able to derive the full snakes-and-ladders bifurcation diagram; in

particular, we show that the width of the snaking region is zero if the tangent of the angle of orientation of the solution is irrational, and is non-zero but exponentially small otherwise. This is done for a reasonably general form of the differential-difference equation; in Chapter 7 we apply our general results to specific examples and discuss some complexities in the calculation of the Stokes multiplier. Finally, we conclude in Chapter 8, and discuss possible avenues for further work.

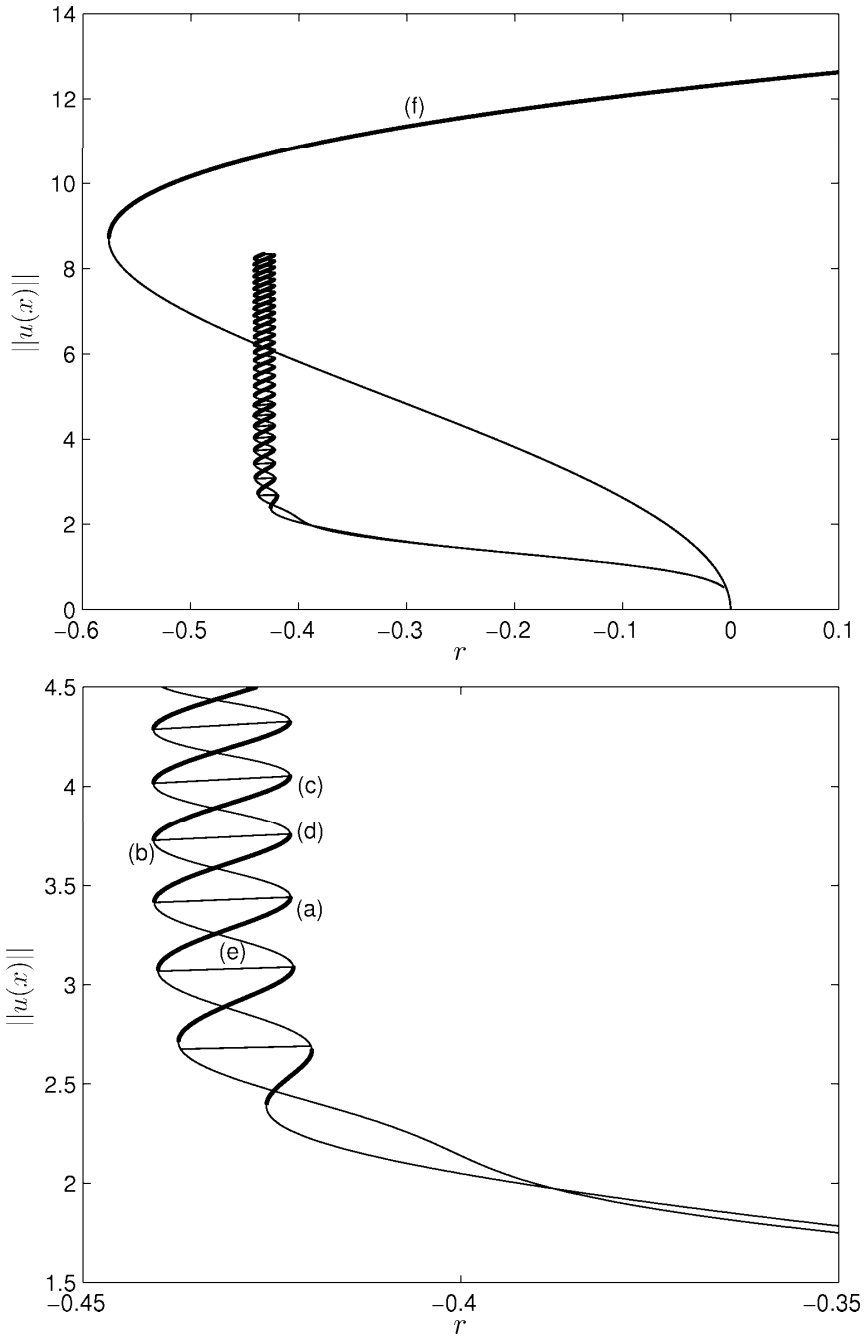

Figure 1.1: *Top: the snakes-and-ladders bifurcation diagram for (1.0.1) with $s = 1.6$, achieved numerically using pseudo-spectral methods on a periodic domain of length 50π, where $||\cdot||$ is the L^2 norm. Bottom: close-up of the bottom of the snaking region. The thick lines indicate stable solutions, and the thin lines indicate unstable solutions; stability of the localised solutions is not indicated in the upper panel. The labels (a)-(f) correspond to the solutions plotted in figure 1.2. Note only the first eight rungs are shown in the upper panel.*

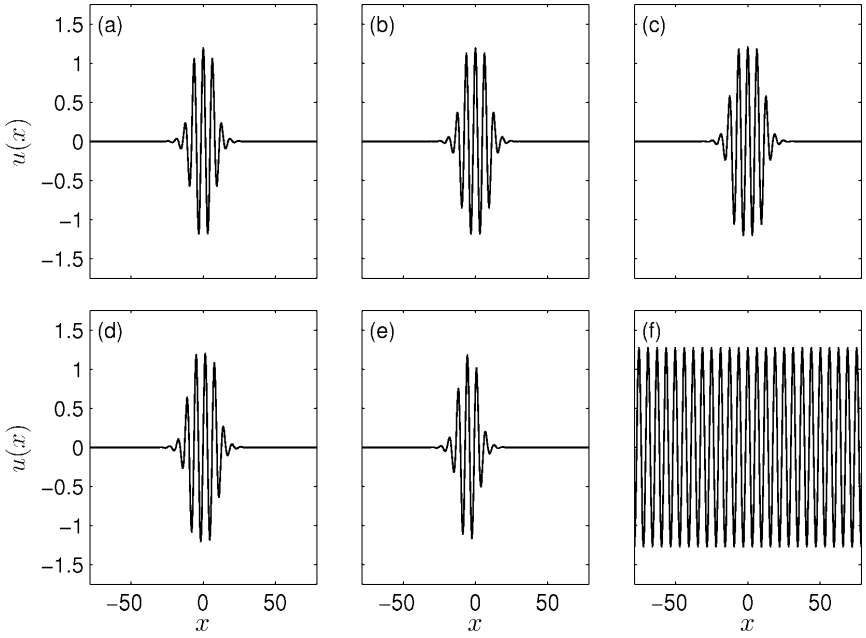

Figure 1.2: *Examples of solutions to (1.0.1) with* $s = 1.6$*, achieved numerically using pseudo-spectral methods on a periodic domain of length* 50π*. The label of each pattern indicates the point at which it can be found in the bifurcation diagram shown in figure 1.1.*

CHAPTER 2

Stokes' phenomenon and the method of exponential asymptotics

In this chapter we shall discuss Stokes' phenomenon in greater detail, and illustrate how the method of exponential asymptotics may be employed to analyse problems in which it occurs. Stokes' phenomenon concerns the behaviour of divergent asymptotic expansions, in which different contributions are dominant in different regions of the complex plane. At certain lines in the complex plane, known as Stokes lines, a subdominant contribution experiences an abrupt increase from zero to non-zero in its coefficient (the Stokes multiplier). In the common parlance of such problems, we say the subdominant term has been 'switched on' by the Stokes line. Although it remains exponentially small, the subdominant term then grows until an anti-Stokes line is reached, at which point the previously dominant term is switched on. While it is exponentially smaller than the dominant one, the subdominant term is impossible to observe using conventional asymptotic methods, as these only account for algebraically small behaviour; hence the development of exponential asymptotics [1, 7, 21, 70, 72] in order to analyse exponentially small behaviour explicitly. We note that some authors swap the definitions of Stokes and anti-Stokes lines given here, and advise that close attention be paid to context in order to avoid confusion. We shall now illustrate this behaviour

by means of an instructive example, the exponential integral.

2.1 Stokes' phenomenon in the exponential integral

The exponential integral is defined as

$$Ei(z) = \int_{-\infty}^{z} \frac{e^t}{t} \mathrm{d}t, \tag{2.1.1}$$

where we choose the contour of integration in the complex plane to avoid the singularity of the integrand at $t = 0$. Now, consider what happens as z moves round the origin. Increasing Arg (z) by 2π, we have

$$Ei(ze^{2\pi i}) = \int_{-\infty}^{z} \frac{e^t}{t} \mathrm{d}t + \oint_{z}^{ze^{2\pi i}} \frac{e^t}{t} \mathrm{d}t. \tag{2.1.2}$$

The first integral on the right-hand side is just $Ei(z)$; hence

$$Ei(ze^{2\pi i}) - Ei(z) = 2\pi i, \tag{2.1.3}$$

where we have used the residue theorem to evaluate the integral around the closed contour $z \to ze^{2\pi i}$. Thus we observe an apparent discontinuity in $Ei(z)$, due to the singularity at the origin of the integrand. In fact, the contribution $2\pi i$ is 'switched on' as a Stokes line is crossed; we shall illustrate this presently. At this point we note that $Ei(z)$ has a logarithmic singularity at $z = 0$ and so a branch cut is required to avoid multi-valuedness. We choose this to be the negative real axis, and restrict $-\pi <$ Arg $(z) \leq \pi$. Note this does not alter the result (2.1.3); the situation is more complicated than a simple branch cut.

The cause of the apparent discontinuity in (2.1.1) can be made clear by employing the method of steepest descents as $|z| \to \infty$. Defining $z = \rho e^{i\theta}$ and performing the change of variables $t = \rho\tau$ in (2.1.1), we have

$$Ei(z) = \int_{-\infty}^{e^{i\theta}} \frac{e^{\rho\tau}}{\tau} \mathrm{d}\tau. \tag{2.1.4}$$

With $\tau = x + iy$ and $(x, y) \in \mathbb{R}^2$, it is easy to see that the lines of steepest descent of the exponent $\rho\tau$ are those of constant y. Because the integrand decays exponentially quickly as $x \to -\infty$ for any fixed y, we do not need to worry about the imaginary part of the lower limit of integration. Hence we can deform the contour of integration on to the horizontal line $y = \sin\theta$, yielding

$$Ei(z) = \int_{-\infty+i\sin(\theta)}^{\cos(\theta)+i\sin(\theta)} \frac{e^{\rho\tau}}{\tau} \mathrm{d}\tau. \tag{2.1.5}$$

The integral is now on the line of steepest descent of the exponent (see the left-hand panel of figure 2.1), and we are able to employ Laplace's method to derive an asymptotic solution. However, there is a caveat, due to the singularity of the integrand at $\tau = 0$. If $\Re(z) > 0$, the line of steepest descent crosses the singularity as $\Im(z)$ increases past zero. Thus, when $\theta > 0$ we must ensure the contour of integration still passes below the singularity. This is achieved by including a 'detour' around the origin; when the line $y = \sin\theta$ reaches the imaginary axis, we require it to first go vertically down to near the origin, circle it once via a closed loop and return vertically up the imaginary axis before continuing to the end-point $e^{i\theta}$, as shown in figure 2.1. The two vertical contours cancel, and so we are left with

$$Ei(z) = 2\pi i H(\theta) + \int_{-\infty+i\sin(\theta)}^{\cos(\theta)+i\sin(\theta)} \frac{e^{\rho\tau}}{\tau} \mathrm{d}\tau, \tag{2.1.6}$$

where we have evaluated the closed integral around the origin in the same manner as in (2.1.2) and (2.1.3). Here H is the Heaviside step function

$$H(t) = \begin{cases} 1 & t > 0, \\ 0 & t < 0; \end{cases} \tag{2.1.7}$$

recall z is restricted to $-\pi < \theta \leq \pi$ due to the branch cut along the negative real axis. Thus the line $\theta = 0$ defines the Stokes line, switching on the contribution $2\pi i$ as it is crossed. Note that it is unclear at this point what happens on the Stokes line, as the discontinuity prevents a simple analytic continuation. We shall for the moment suppose that $\theta \neq 0$, and return to this point later.

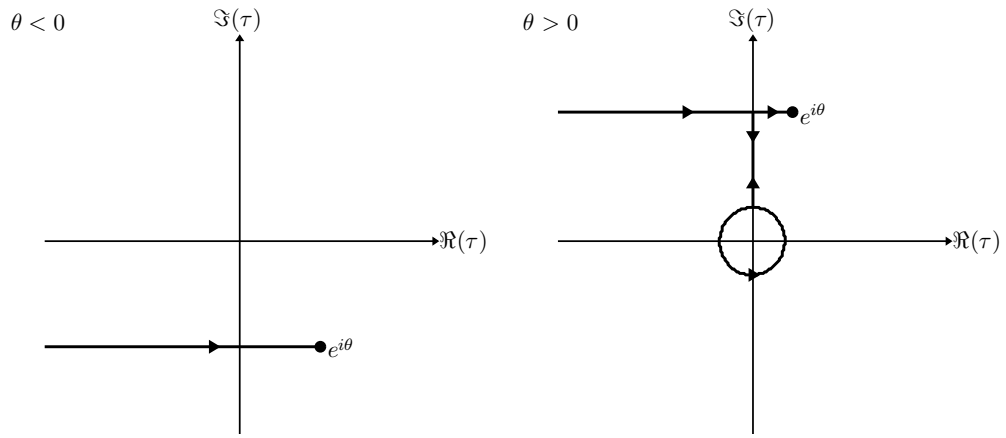

Figure 2.1: *Steepest descent contours for the integral (2.1.4). When $\theta < 0$, the contour is simply the line $\Im(\tau) = \sin\theta$ (left). However, as θ increases past zero, the contour passes over the singularity of the integrand at $\tau = 0$, and so must be deformed as in the right-hand panel. The contours along the imaginary axis cancel, but the closed contour around the origin contributes a term $2\pi i$ to (2.1.4), yielding the result (2.1.6).*

We may now evaluate the integral in (2.1.6) using Laplace's method. Writing $\tau = x + e^{i\theta}$, we can see that it is dominated by the region near $x = 0$, giving

$$\begin{aligned} Ei(z) &= 2\pi i H(\theta) + e^z \int_{-\infty}^{0} \frac{e^{\rho x}}{x + e^{i\theta}} \mathrm{d}x \\ &\sim 2\pi i H(\theta) + e^z e^{-i\theta} \int_{-\infty}^{0} e^{\rho x} \sum_{n=0}^{\infty} (-1)^n e^{-in\theta} x^n \mathrm{d}x \\ &\sim 2\pi i H(\theta) + \frac{e^z}{z} \sum_{n=0}^{\infty} \frac{n!}{z^n}. \end{aligned} \tag{2.1.8}$$

Thus we have derived an asymptotic series solution for the exponential integral. We can now see that the anti-Stokes line is defined by the line $\theta = \frac{\pi}{2}$, as beyond this line the series contribution to (2.1.8) is exponentially small and the contribution $2\pi i$ is dominant. Note, however, that the series in (2.1.8) is divergent; this must therefore be truncated if the solution is to be meaningful. We shall show in the next section that the change in the constant term is not discontinuous, as suggested by (2.1.8), but is in fact smooth and rapid in a narrow region around the Stokes line; this variation is encoded within the remainder of the truncated series.

2.1.1 Error function smoothing of the remainder

As (2.1.8) is divergent, we truncate the series after N terms, yielding

$$Ei(z) \sim \frac{e^z}{z} \sum_{n=0}^{N-1} \frac{n!}{z^n} + R_N(z), \tag{2.1.9}$$

for some remainder $R_N(z)$ to be determined. Note the discontinuous term $2\pi i H(\theta)$ appearing in (2.1.8) has been incorporated into $R_N(z)$. We shall show presently that R_N varies smoothly but rapidly from zero to $2\pi i$ as the Stokes line $\theta = 0$ is crossed, thus 'smoothing out' the discontinuity. Away from the Stokes line, R_N is equal to $2\pi i H(\theta)$.

We shall analyse the remainder by means of the differential equation

$$\frac{\mathrm{d}^2 f}{\mathrm{d}z^2} + \left(\frac{1}{z} - 1\right) \frac{\mathrm{d}f}{\mathrm{d}z} = 0, \tag{2.1.10}$$

following the method of [72], therein applied to the error function and other examples. This has solution

$$f(z) = AEi(z) + B, \tag{2.1.11}$$

for some constants A and B. As $Ei(z)$ is a solution of (2.1.10), substitution of (2.1.9) therefore provides a differential equation for R_N. Solving this will enable us to derive explicitly the switching on of the contribution $2\pi i$ at the Stokes line.

We first verify that the asymptotic series (2.1.9) satisfies (2.1.10), up to an error due to truncation. Differentiating (2.1.9) once, we have

$$\begin{aligned} \frac{\mathrm{d}Ei}{\mathrm{d}z} &= \frac{e^z}{z} \sum_{n=0}^{N-1} \left(\frac{n!}{z^n} - \frac{(n+1)!}{z^{n+1}} \right) + \frac{\mathrm{d}R_N}{\mathrm{d}z} \\ &= \frac{e^z}{z} \left(1 - \frac{N!}{z^N} \right) + \frac{\mathrm{d}R_N}{\mathrm{d}z}; \end{aligned} \tag{2.1.12}$$

hence

$$\frac{\mathrm{d}^2 Ei}{\mathrm{d}z^2} = \frac{e^z}{z} \left(1 - \frac{1}{z} - \frac{N!}{z^N} + \frac{(N+1)!}{z^{N+1}} \right) + \frac{\mathrm{d}^2 R_N}{\mathrm{d}z^2}, \tag{2.1.13}$$

and substituting (2.1.9) into (2.1.10) yields

$$\frac{\mathrm{d}^2 R_N}{\mathrm{d}z^2} + \left(\frac{1}{z} - 1\right) \frac{\mathrm{d}R_N}{\mathrm{d}z} = -N e^z \frac{N!}{z^{N+2}}. \tag{2.1.14}$$

(2.1.14) simplifies considerably if we truncate the expansion (2.1.9) optimally, i.e. after the least term. Comparing successive terms in (2.1.9), we see that the series begins to diverge when

$$\left|\frac{N!}{z^N}\frac{z^{N-1}}{(N-1)!}\right| \sim 1, \tag{2.1.15}$$

giving

$$N \sim |z| + \nu, \tag{2.1.16}$$

where ν is added to ensure N is an integer, and is bounded as $|z| \to \infty$. Writing $z = \rho e^{i\theta}$ and employing Stirling's approximation for large factorials

$$n! \sim \sqrt{2\pi} n^{n+1/2} e^{-n}, \qquad n \to \infty, \tag{2.1.17}$$

we see that the right-hand side (RHS) of (2.1.14) becomes

$$\begin{aligned}
\text{RHS} &\sim -\sqrt{2\pi} e^z \frac{N^{N+3/2} e^{-N}}{z^{N+2}} \\
&\sim -\sqrt{2\pi} e^{\rho e^{i\theta}} \frac{(\rho+\nu)^{\rho+\nu+3/2} e^{-\rho-\nu}}{\rho^{\rho+\nu+2} e^{i(\rho+\nu+2)\theta}} \\
&= -\sqrt{\frac{2\pi}{\rho}} \exp\left[\rho\left(e^{i\theta}-1\right) + \left(\rho+\nu+\frac{3}{2}\right)\ln\left(1+\frac{\nu}{\rho}\right) - i(\rho+\nu+2)\theta - \nu\right] \\
&\sim -\sqrt{\frac{2\pi}{\rho}} \exp\left[\rho\left(e^{i\theta}-1\right) - i(\rho+\nu+2)\theta\right].
\end{aligned} \tag{2.1.18}$$

Thus the forcing of (2.1.14) is exponentially small except at $\theta = 0$, the Stokes line. To capture the effects of maximal forcing, we scale close to the Stokes line and write $\theta = \eta\hat{\theta}$ for $|\eta| \ll 1$, where the exact scaling is to be determined. This gives

$$\text{RHS} \sim -\sqrt{\frac{2\pi}{\rho}} \exp\left[-\frac{1}{2}\rho\eta^2\hat{\theta}^2\right], \tag{2.1.19}$$

suggesting the scaling $\eta = 1/\sqrt{\rho}$. Thus we obtain

$$\text{RHS} \sim -\sqrt{\frac{2\pi}{\rho}} e^{-\hat{\theta}^2/2}. \tag{2.1.20}$$

We are now in a position to derive the leading-order change as R_N crosses the Stokes line. From (2.1.20), we see that maximal change occurs in the azimuthal direction, and

so hold ρ constant and write

$$\frac{\mathrm{d}}{\mathrm{d}z} = -\frac{ie^{-i\theta}}{\rho}\frac{\mathrm{d}}{\mathrm{d}\theta} \sim -\frac{i}{\sqrt{\rho}}\frac{\mathrm{d}}{\mathrm{d}\hat{\theta}}. \tag{2.1.21}$$

Hence the leading-order contribution to (2.1.14) is

$$\frac{\mathrm{d}R_N}{\mathrm{d}\hat{\theta}} \sim i\sqrt{2\pi}e^{-\hat{\theta}^2/2}. \tag{2.1.22}$$

This has solution

$$R_N \sim \pi i\left(1 + \mathrm{erf}\left(\frac{\hat{\theta}}{\sqrt{2}}\right)\right), \tag{2.1.23}$$

where $\mathrm{erf}\,(z)$ is the error function, defined to be

$$\mathrm{erf}\,(z) = \frac{2}{\sqrt{\pi}}\int_0^z e^{-t^2}\mathrm{d}t. \tag{2.1.24}$$

We have chosen the constant of integration in (2.1.23) to be πi in order to conform with our earlier observation that the singularity at $t = 0$ in (2.1.1) produces a contribution $2\pi i$ when $\theta > 0$, but not when $\theta < 0$, as in (2.1.6). Thus we have shown how the constant contribution to $Ei(z)$ varies smoothly but rapidly from zero to $2\pi i$ via an error function as the Stokes line is crossed. Note that we can now analytically continue (2.1.9) to also hold at $\theta = 0$, where we see that $R_N = \pi i$, or half the change in $Ei(z)$ across the Stokes line.

2.1.2 An alternative method: integration by parts

As an aside, we mention an alternative method to derive an asymptotic series solution to (2.1.1); integration by parts. After N integrations, (2.1.1) reads

$$Ei(z) \sim \frac{e^z}{z}\sum_{n=0}^{N-1}\frac{n!}{z^n} + I_N(z), \tag{2.1.25}$$

where

$$I_N(z) = N!\int_{-\infty}^{z}\frac{e^t}{t^{N+1}}\mathrm{d}t. \tag{2.1.26}$$

(2.1.25) is an asymptotic series as $|z| \to \infty$, and is in fact precisely the series as that derived earlier using the method of steepest descents (2.1.9), except in this case the remainder is given explicitly as $I_N(Z)$. However, if we differentiate I_N once with respect to θ, we have

$$\frac{\mathrm{d}I_N}{\mathrm{d}\theta} = ie^z \frac{N!}{z^N}; \tag{2.1.27}$$

by optimally truncating as in (2.1.16) and rescaling near the Stokes line, this simplifies to give (2.1.22), and the result (2.1.23) follows. Although this method may seem simpler, the longer process of solving (2.1.1) using steepest descents has allowed us to describe the switching on of the contribution $2\pi i$ as the Stokes line is crossed in an intuitive manner as being due to the crossing of a singularity by a contour of steepest descent. Furthermore, it is instructive to derive the error function smoothing of the remainder by solving its differential equation (2.1.14), since the method is similar for problems which do not have an integral representation.

2.2 Exponential asymptotics

The error function smoothing of Stokes discontinuities was first derived by Berry [7], and later made rigorous in [70]. Berry's analysis was applied to the error function itself (2.1.24), using a different method to that presented here. We note that, unlike the exponential integral (2.1.1), the integrand of the error function is not singular. In this case, Stokes' phenomenon occurs due to the line of steepest descents intersecting the saddle point of the integrand. This forces a discontinuous change in the contour of integration analogous to figure 2.1, also switching on a subdominant contribution.

We have thus far discussed Stokes' phenomenon in the context of asymptotic approximation of integrals, and defined Stokes lines as when the line of steepest descents intersects a singularity (or saddle point) of the integrand, thus switching on a subdominant contribution. However, the phenomenon also occurs in asymptotic solutions to

differential equations, without an integral representation. In such cases the method of analysing the remainder via its differential equation described in Section 2.1.1 is especially useful, as it provides a clear and explicit derivation of the smooth switching on of terms otherwise hidden in the exponentially small remainder [72]. Motivated by this method, we are able to interpret Stokes lines as lines in the complex plane at which the forcing of the remainder equation is maximal, i.e. those lines at which the remainder experiences greatest variation.

Stokes' phenomenon occurs when an asymptotic expansion is divergent. Two ingredients are sufficient for divergence in a differential equation: a singular perturbation, so that the highest derivative does not contribute at leading-order, and a solution with (usually complex) singularities. These two properties produce an asymptotic expansion which is divergent in the form of a factorial over a power [1, 21]; this generic form of the divergence allows the derivation of an asymptotic formula for late terms in the expansion, which is necessary as an explicit solution for the nth term is usually unobtainable. Truncation of the asymptotic series and substitution into the original differential equation then produces an equation for the remainder, with forcing due to the truncation error. Then, truncating optimally as in Section 2.1.1 and rescaling near the lines of maximal forcing (the Stokes lines) allows the derivation of the leading-order contribution to the remainder, showing explicitly the switching on of a particular complementary function to the remainder equation. This invariably yields crucial information regarding the solution which would otherwise be hidden behind the dominant terms in the asymptotic expansion.

We shall use this method throughout the thesis to analyse various homoclinic snaking problems, in a similar manner to [22, 51]. We shall find that the terms which are switched on at Stokes lines are exponentially growing. Requiring that these unbounded terms vanish results in a solvability condition on the leading-order solution, yielding the pinning mechanism by which stationary fronts exist away from the Maxwell point.

This pinning can only take place within an exponentially small parameter range, providing a formula for the width of the snaking region. Furthermore, matching exponentially growing and decaying terms in back-to-back fronts produces an asymptotic description of the full snakes-and-ladders bifurcation diagram.

CHAPTER 3

Multiple scales analysis of the cubic-quintic Swift-Hohenberg equation

The Swift-Hohenberg equation (SHE) [84] is the archetypal model of pattern formation [33]. Due to its relative amenability to analysis and prevalence in the literature, perhaps the most extensive studies of localised patterns and homoclinic snaking have been carried out in the SHE and its variants [10, 13, 14, 39, 56, 78]. We shall continue in this tradition and focus on the cubic-quintic SHE in one dimension, namely

$$\frac{\partial u}{\partial t} = ru - \left(1 + \frac{\partial^2}{\partial x^2}\right)^2 u + su^3 - u^5; \tag{3.0.1}$$

the methods described are equally applicable to generalisations of (3.0.1), as well as other pattern-forming problems. The bifurcation diagram of (3.0.1) with $s = 1.6$ is shown in figure 1.1, and example solutions in figure 1.2. The trivial solution $u \equiv 0$ loses stability at $r = 0$ via a subcritical pitchfork bifurcation to constant amplitude spatial oscillations. This solution branch turns over at a subsequent saddle-node at some $r < 0$, providing a region of bistability between the zero and patterned states. Localised patterns form a snakes-and-ladders bifurcation structure within the bistable

region. The same bifurcation diagram is observed for all $s > 0$; however, if $s \leq 0$ the pitchfork is supercritical and there is no region of bistability, and hence no snaking.

Figure 1.1 is the product of numerical computations, as are many studies of snaking behaviour [13, 14]. We desire to study snaking analytically; to begin with, we shall describe in this chapter how the much simpler behaviour of constant amplitude spatial oscillations can be studied using the method of multiple scales. Then we shall discuss why the conventional method fails to capture snaking behaviour, and hence why it must be extended to incorporate exponentially small effects [22, 39, 56]. This shall pave the way for a more complete asymptotic description of the SHE via the method of exponential asymptotics [7], incorporating the snakes-and-ladders bifurcation observed numerically, to be carried out in the next two chapters.

To see why the method of multiple scales is the correct one to use, first linearise (3.0.1) around $u \equiv 0$ by writing $u \sim \epsilon e^{\sigma t + ikx}$ for some constant $0 < \epsilon \ll 1$ and neglecting terms smaller than $\mathrm{O}(\epsilon)$. Thus we obtain the growth rate equation

$$\sigma = r - (1 - k^2)^2. \tag{3.0.2}$$

As r increases, σ first vanishes when $r = 0$ and $|k| = 1$, indicating that the trivial solution first loses stability to spatial oscillations with wavenumber ± 1. Assuming $|r| \ll 1$ and writing $k = \pm 1 + \hat{k}$ with $|\hat{k}| \ll 1$ then gives

$$\sigma = r - 4\hat{k}^2 + \mathrm{O}(\hat{k}^3), \tag{3.0.3}$$

suggesting that the dynamics close to bifurcation take place on the slow scales $x = \mathrm{O}\left(r^{-1/2}\right)$ and $t = \mathrm{O}\left(r^{-1}\right)$, as well as the fast scale $x = \mathrm{O}(1)$. Thus we expect a solution in the form of slowly modulated spatial oscillations with wavenumber ± 1.

We therefore perform a multiple-scales analysis of (3.0.1) by rescaling its parameters (3.0.1) as

$$r = \epsilon^4 r_4, \quad s = \epsilon^2 s_2. \tag{3.0.4}$$

Defining the slow scales

$$X = \epsilon^2 x, \quad T = \epsilon^4 t, \tag{3.0.5}$$

with

$$u(x,t) = \epsilon U(x, X, T). \tag{3.0.6}$$

(3.0.1) then becomes

$$\epsilon^4 \frac{\partial U}{\partial T} = \epsilon^4 r_4 U - \left[\left(1 + \frac{\partial^2}{\partial x^2} \right)^2 + 4\epsilon^2 \left(1 + \frac{\partial^2}{\partial x^2} \right) \frac{\partial^2}{\partial x \partial X} + \epsilon^4 \left(2 + 6\frac{\partial^2}{\partial x^2} \right) \frac{\partial^2}{\partial X^2} + 4\epsilon^6 \frac{\partial^4}{\partial x \partial X^3} + \epsilon^8 \frac{\partial^4}{\partial X^4} \right] U + \epsilon^4 s_2 U^3 - \epsilon^4 U^5. \tag{3.0.7}$$

We may now seek an asymptotic solution in the form of a power series,

$$U(x, X, T) = U_0(x, X, T) + \epsilon^2 U_1(x, X, T) + \epsilon^4 U_2(x, X, T) + \cdots, \tag{3.0.8}$$

by equating terms in (3.0.7) at each order in ϵ^2. Note the above scalings have been chosen in order to ensure the correct balance of terms in the subsequent calculation. In particular, setting $s = \mathrm{O}\left(\epsilon^2\right)$ ensures that the asymptotic regime incorporates the bistable nature of (3.0.1), and hence also the snaking region.

Equating terms at $\mathrm{O}\left(1\right)$ provides the leading-order contribution

$$0 = -\left(1 + \frac{\partial^2}{\partial x^2} \right)^2 U_0, \tag{3.0.9}$$

with solution

$$U_0 = A_0(X, T) e^{ix} + A_0^*(X, T) e^{-ix}, \tag{3.0.10}$$

where the asterisk represents complex conjugation. Hence the solution takes the expected form of slowly modulated spatial oscillations with wavenumber ± 1. The amplitude A_0 is determined by applying a solvability condition, which we shall now derive by continuing the calculation to higher orders in ϵ^2.

At $\mathrm{O}\left(\epsilon^2\right)$, we simply have

$$0 = -\left(1 + \frac{\partial^2}{\partial x^2} \right)^2 U_1, \tag{3.0.11}$$

so

$$U_1 = A_1(X,T)e^{ix} + A_1^*(X,T)e^{-ix} \tag{3.0.12}$$

Then, $\mathrm{O}\left(\epsilon^4\right)$ terms yield

$$\left(1+\frac{\partial^2}{\partial x^2}\right)^2 U_2 = -\frac{\partial U_0}{\partial T} + r_4 U_0 - \left(2+6\frac{\partial^2}{\partial x^2}\right)\frac{\partial^2 U_0}{\partial X^2} + s_2 U_0^3 - U_0^5, \tag{3.0.13}$$

with the usual homogeneous solution

$$U_2 = A_2(X,T)e^{ix} + A_2^*(X,T)e^{-ix}. \tag{3.0.14}$$

To determine the particular integral, we note the right-hand side of (3.0.13) takes the form

$$C_5 e^{5ix} + C_3 e^{3ix} + C_1 e^{ix} + C_1^* e^{-ix} + C_3^* e^{-3ix} + C_5^* e^{-5ix}, \tag{3.0.15}$$

where the C_k are function of X and T. Although the forcing terms which are proportional to e^{kix} for $k = \pm 3, \pm 5$ can be accounted for by the particular integral

$$\left(1-k^2\right)^{-2} C_k e^{kix}, \tag{3.0.16}$$

those proportional to $e^{\pm ix}$ are problematic, as $e^{\pm ix}$ are the complementary functions of (3.0.13). Hence these forcing terms are resonant and lead to a particular integral which is unbounded as $x \to \pm\infty$. Because we require that $\epsilon^2 U_2$ remains $\mathrm{O}\left(\epsilon^2\right)$ for all x in order to retain a uniform asymptotic expansion, we must fix $C_1 = 0$, thus eliminating secular terms. Considering (3.0.10) and (3.0.13), this requires that

$$\frac{\partial A_0}{\partial T} = r_4 A_0 + 4\frac{\partial^2 A_0}{\partial X^2} + 3s_2|A_0|^2 A_0 - 10|A_0|^4 A_0. \tag{3.0.17}$$

(3.0.17) is often referred to as the 'solvability condition'; solving it determines the slow-scale dynamics of the leading-order solution (3.0.10).

3.1 Constant amplitude solutions

We shall first consider constant solutions to (3.0.17), which correspond to solutions of (3.0.1) in the form of spatial oscillations with constant amplitude. Setting $A_0 = W_0 e^{i\phi}$,

where W_0 and ϕ are real constants, (3.0.17) gives us

$$0 = r_4 W_0 + 3s_2 W_0^3 - 10W_0^5. \tag{3.1.1}$$

We also have ϕ arbitrary, which is due to the invariance of (3.0.17) under rotations $A_0 \to A_0 e^{i\phi}$. (3.1.1) has up to five distinct solutions, given by

$$W_0 = 0, \pm\sqrt{W_+}, \pm\sqrt{W_-}, \tag{3.1.2}$$

where

$$W_\pm = \frac{3}{20}s_2 \pm \frac{1}{20}\sqrt{9s_2^2 + 40r_4}. \tag{3.1.3}$$

Note that we may consider $W_0 \geq 0$ without loss of generality, as $W_0 < 0$ may be recovered from (3.0.17) via the symmetry $A_0 \to -A_0$. While the trivial solution exists for all r_4 and s_2, the other four solutions are only viable in certain parameter ranges, which may be determined by enforcing $W_\pm$ real and positive. Doing so, we find that if $s_2 > 0$ then $A_0 = \pm\sqrt{W_+}e^{i\phi}$ is a solution in the range $r_4 \geq -9s_2^2/40$, and $A_0 = \pm\sqrt{W_-}e^{i\phi}$ in the range $-9s_2^2/40 \leq r_4 < 0$. On the other hand, if $s_2 \leq 0$ then $A_0 = \pm\sqrt{W_+}e^{i\phi}$ is a solution for $r_4 > 0$, but $A_0 = \pm\sqrt{W_-}e^{i\phi}$ ceases to be a valid solution.

We can analyse the bifurcation structure of these constant amplitude solutions by performing a linear stability analysis of (3.0.17). To this end, we set $A_0 = (W_0 + a_0(X,T) + ib_0(X,T))e^{i\phi}$, where W_0 is one of the solutions in (3.1.2) and a_0 and b_0 are real and of small magnitude. Substituting into (3.0.17), linearising and equating real and imaginary parts yields

$$\frac{\partial a_0}{\partial T} = \frac{\partial^2 a_0}{\partial X^2} + \left(r_4 + 9s_2W_0^2 - 50W_0^4\right)a_0, \tag{3.1.4}$$

$$\frac{\partial b_0}{\partial T} = \frac{\partial^2 b_0}{\partial X^2} + \left(r_4 + 3s_2W_0^2 - 10W_0^4\right)b_0. \tag{3.1.5}$$

As W_0 satisfies (3.1.1), writing $a_0 = \hat{a}_0 e^{\sigma_1 T + ik_1 X}$, $b_0 = \hat{b}_0 e^{\sigma_2 T + ik_2 X}$ gives

$$\sigma_1 = -k_1^2 + \left(6s_2W_0^2 - 40W_0^4\right), \tag{3.1.6}$$

$$\sigma_2 = -k_2^2, \tag{3.1.7}$$

and we see that the imaginary part of small perturbations always decays. Considering first the trivial solution, $A_0 \equiv 0$ is unstable to perturbations with small wavenumber; this corresponds to the linear stability analysis carried out at the beginning of the chapter, in which we saw that the solution $u \equiv 0$ to the original equation (3.0.1) is unstable to perturbations with wavenumber close to ± 1. The other constant amplitude solutions are given by $W_0^2 = W_\pm$, which give

$$6s_2 W_\pm - 40W_\pm^2 = -\frac{1}{10}\sqrt{9s_2^2 + 40r_4}\left(\sqrt{9s_2^2 + 40r_4} \pm 3s_2\right). \tag{3.1.8}$$

In the relevant parameter ranges satisfying existence of $W_\pm$, this quantity is negative for the choice $W_0^2 = W_+$, but positive for $W_0^2 = W_-$. Thus $A_0 = \pm\sqrt{W_+}e^{i\phi}$ is always linearly stable, while $A_0 = \pm\sqrt{W_-}e^{i\phi}$ is always linearly unstable.

We can now describe the bifurcation structure of constant amplitude solutions. The trivial solution loses stability at $r_4 = 0$ via a pitchfork bifurcation, which is supercritical for $s_2 \leq 0$ and subcritical for $s_2 > 0$. In the latter case, there is a secondary saddle-node bifurcation at $r_4 = -9s_2^2/40$, at which the solution branch turns over and becomes stable. We compare our asymptotic analysis with numerical computations in figure 3.1, which were obtained by solving (3.0.1) on a periodic domain of length $D = 10\pi$ using a Fourier pseudo-spectral method. We see that the numerical bifurcation diagram is faithfully reproduced by the asymptotic calculation, albeit with decreasing accuracy as r_4 increases. This discrepancy is simply because the present analysis is only valid close to bifurcation, described asymptotically by the limit $\epsilon \to 0$.

3.2 Front solutions

Having successfully described the bifurcation structure of constant amplitude solutions using the method of multiple scales, we shall now discuss how the same method may be applied to front solutions, the building blocks of localised patterns. First, we have seen that the SHE (3.0.1) is bistable only when s is positive, and so shall fix $s > 0$

henceforth. Then, within the bistable region we may seek a front which connects the patterned state to the trivial state. These correspond to steady solutions of the amplitude equation (3.0.17) which connect $A_0 = \sqrt{W_+}e^{i\phi}$ to $A_0 \equiv 0$; solutions connecting $A_0 = -\sqrt{W_+}e^{i\phi}$ to $A_0 \equiv 0$ are given simply by exploiting the invariance of (3.0.17) under the reflection $A_0 \to -A_0$.

Writing $A_0 \equiv W_0(X)e^{i\phi_0(X)}$ in (3.0.17) gives us

$$0 = r_4 W_0 + 4\frac{\mathrm{d}^2 W_0}{\mathrm{d}X^2} - 4W_0\left(\frac{\mathrm{d}\phi_0}{\mathrm{d}X}\right)^2 + 3s_2 W_0^3 - 10W_0^5, \tag{3.2.1}$$

$$0 = 2\frac{\mathrm{d}W_0}{\mathrm{d}X}\frac{\mathrm{d}\phi_0}{\mathrm{d}X} + W_0\frac{\mathrm{d}^2\phi_0}{\mathrm{d}X^2}, \tag{3.2.2}$$

and we impose the boundary conditions

$$W_0 \to \sqrt{W_+} \text{ as } X \to -\infty, \tag{3.2.3}$$

$$W_0 \to 0 \text{ as } X \to \infty. \tag{3.2.4}$$

Multiplying (3.2.2) by W_0 and integrating we obtain

$$\frac{\mathrm{d}\phi_0}{\mathrm{d}X} = \frac{C}{W_0^2} \tag{3.2.5}$$

for some constant C. However, upon substitution into (3.2.1), we see that we must have $C = 0$ in order to satisfy the boundary condition at $X = \infty$. Thus ϕ_0 must be constant, and we set $\phi_0 = \phi$; again, the arbitrary phase ϕ arises due to the invariance of (3.0.17) under rotations.

Multiplying (3.2.1) by $\mathrm{d}W_0/\mathrm{d}X$ and integrating, we have

$$0 = \frac{1}{2}r_4 W_0^2 + 2\left(\frac{\mathrm{d}W_0}{\mathrm{d}X}\right)^2 + \frac{3}{4}s_2 W_0^4 - \frac{5}{3}W_0^6, \tag{3.2.6}$$

where we have again set the constant of integration to zero in order to satisfy the boundary condition at $X = \infty$. In order to satisfy the boundary condition at $X = -\infty$, $\sqrt{W_+}$ must satisfy the X-independent versions of (3.2.1) and (3.2.6), yielding

$$0 = \sqrt{W_+}\left(r_4 + 3s_2 W_+ - 10W_+^2\right), \tag{3.2.7}$$

$$0 = W_+\left(\frac{1}{2}r_4 + \frac{3}{4}s_2 W_+ - \frac{5}{3}W_+^2\right). \tag{3.2.8}$$

As $W_+ \neq 0$, this equation pair has solution

$$r_4 = r_{M,1} := -\frac{27}{160}s_2^2, \quad W_+ = \sqrt{-\frac{3}{10}r_{M,1}}, \tag{3.2.9}$$

where we have chosen the positive square root in compliance with the boundary condition at $X = -\infty$; the negative root corresponds to the solution $-A_0(X)$. Note that the value given for W_+ is simply (3.1.3) with $r_4 = r_{M,1}$.

Setting $r_4 = r_{M,1}$, rearrangement of (3.2.6) provides the integral

$$\int \frac{\mathrm{d}W_0}{W_0(9s_2/40 - W_0^2)} = \sqrt{\frac{5}{6}} \int \mathrm{d}X, \tag{3.2.10}$$

where we have chosen the positive square root to ensure $W_0 \to 0$ as $X \to \infty$. This has solution

$$W_0 = \left(\frac{3}{10}\right)^{1/4} \frac{\sqrt{\mu}}{\sqrt{1 + e^{\mu X}}} =: A_f(X), \tag{3.2.11}$$

where $\mu = \sqrt{-r_{M,1}}$. Note we have set the constant of integration to zero as it simply corresponds to a change of origin, and (3.0.17) is invariant under translations in X.

We can think of $A_0 = A_f(X)e^{i\phi}$ as a travelling wave with zero wavespeed. Indeed, for $r_4 > r_{M,1}$ the equivalent solution is a travelling wave in which the non-zero amplitude 'wins out' over the trivial state, while for $r_4 < r_{M,1}$ the converse occurs. However, the foregoing calculation does not provide the whole picture. According to our leading-order analysis, stationary fronts exist only at the Maxwell point $r \sim \epsilon^4 r_{M,1}$, which leads to the erroneous conclusion that localised patterns comprising back-to-back fronts also only exist at the Maxwell point. This is in clear contradiction to numerical results such as that shown in figure 1.1, which indicate that localised solutions to (3.0.1) form a snakes-and-ladders structure centred on the Maxwell point.

There is a clue as to how to resolve this discrepancy in the symmetries of the SHE (3.0.1) and its amplitude equation (3.0.17). Inspection of (3.0.17) indicates that the solution (4.1.7) is unique up to a change in origin, a change of sign of X and a change of sign of A_0. Each of these symmetries corresponds to a symmetry of the SHE, as (3.0.1) is

invariant under translations and reflections in x and reflections in u. However, (3.0.17) also has a fourth symmetry, given by the arbitrary phase ϕ; any rotation of a particular solution to (3.0.17) also provides a solution. Due to the form of the leading-order solution $U_0 = A_0 e^{ix} + A_0^* e^{-ix}$, this is equivalent to the translation $x \to x + \phi$, and appears due to (3.0.7) being invariant under (independent) translations in both x and X. This fourth symmetry is somewhat unexpected, as it has no counterpart in (3.0.1), and is an artefact of the multiple-scales approach. In fact, the apparent arbitrariness of the phase is illusory, as it is the fixing of this phase which provides the locking mechanism that generates snaking bifurcations. That said, the method of multiple scales alone is insufficient to derive ϕ, as it remains arbitrary to all algebraic orders. Exponentially small, or beyond-all-orders, terms in the tail of the asymptotic expansion must be considered, which requires the method of exponential asymptotics; the application of this method to the present problem and the subsequent fixing of ϕ provides the subject matter of the following chapter.

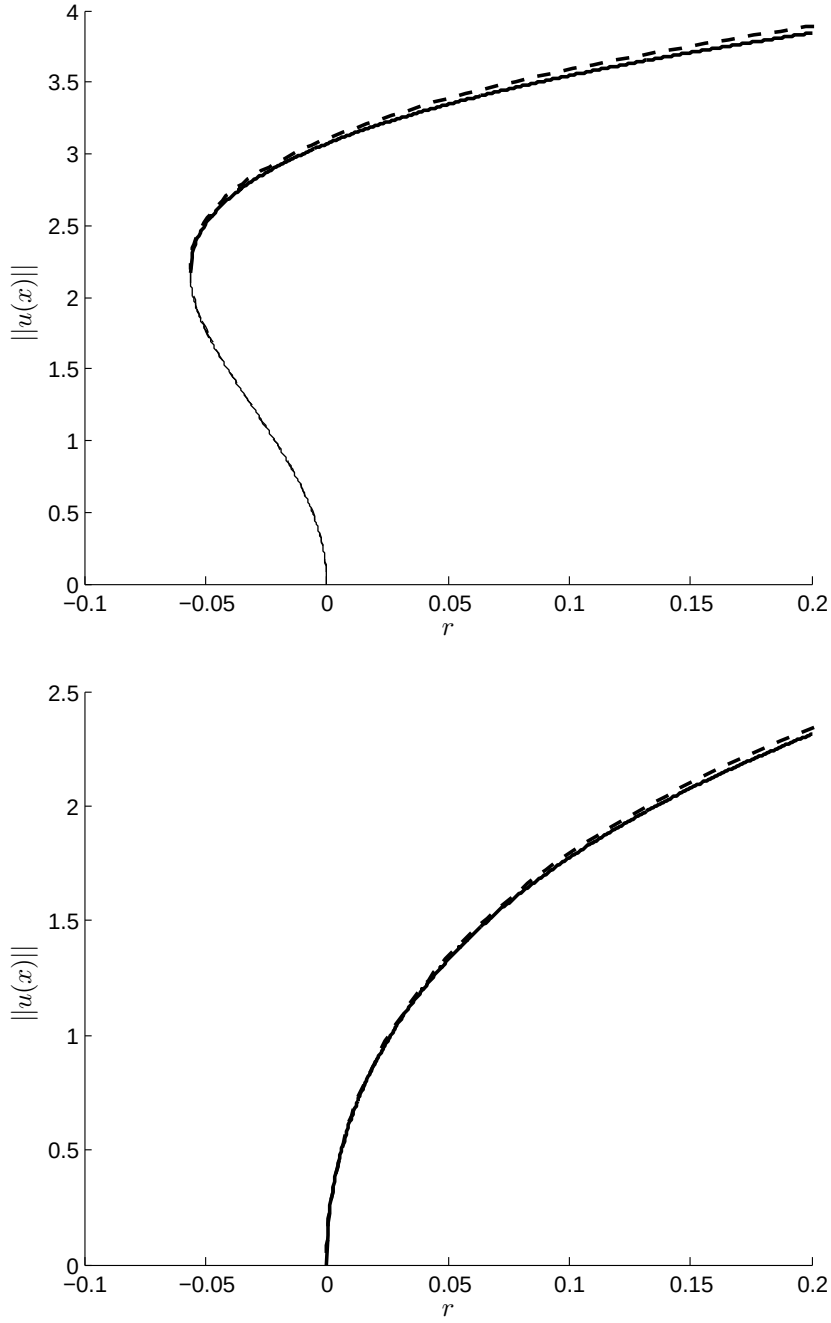

Figure 3.1: *Numerical (broken lines) and asymptotic (solid lines) bifurcation diagrams of constant amplitude solutions to (3.0.1). The left-hand panel shows the subcritical case with* $s = 0.5$*, and the right-hand panel shows the supercritical case with* $s = -0.5$*. Stable solutions are indicated by thick lines, and unstable by thin lines.* $||\cdot||$ *is the* L^2 *norm.*

CHAPTER 4

Homoclinic snaking in the cubic-quintic Swift-Hohenberg equation

The purpose of the present chapter is to apply the ideas of exponential asymptotics to the cubic-quintic Swift-Hohenberg equation (SHE)

$$\frac{\partial u}{\partial t} = ru - \left(1 + \frac{\partial^2}{\partial x^2}\right)^2 u + su^3 - u^5, \tag{4.0.1}$$

in order to derive an analytical formula which describes the snaking bifurcation diagram in the small-amplitude limit near the pattern-forming bifurcation at $r = 0$. To begin with, the focus is upon stationary fronts, the building blocks of localised patterns. Once these are understood fully, localised patterns may be constructed at will. This we do in the next chapter.

The observation that the leading-order front solution (3.2.11) of the SHE has singularities in the complex plane, coupled with the fact that the perturbation problem (3.0.7) is singular in the slow scale, leads to the conclusion that the subsequent asymptotic expansion is divergent and should be truncated [51]. Truncating the asymptotic expansion in an optimal fashion ensures that the remainder is exponentially small, and

results in an inhomogeneous equation from which the remainder may be determined. The forcing of the remainder equation is maximal at certain lines in the complex plane, known as Stokes lines. By rescaling in the neighbourhood of the intersections between these Stokes lines and the real axis, the coefficient of a complementary function is seen to vary from zero to non-zero as they are crossed. This 'switching on' is shown to take place smoothly by means of an error function, as is usual [7]. As the complementary function is exponentially growing, the requirement that this vanish provides a relationship between the phase of the pattern and the distance from the Maxwell point, thus giving a formula for the width of the region in which fronts (and localised patterns built from superpositions of fronts) are stationary. Moreover, the growing exponential terms allow two distant fronts to be matched together, leading to a set of equations describing the full snakes-and-ladders bifurcation structure.

This was first done by Kozyreff and Chapman in the SHE with quadratic and cubic nonlinearities [56]; the present calculation is similar. However, we are able to provide a more convincing numerical comparison, since we are able to calculate the Stokes multiplier through iteration of a recurrence relation. Kozyreff and Chapman rely instead upon a best fit approximation, rendering their comparison somewhat inexact. Indeed, our ability to provide a quantitative comparison between analytical and numerical results is one of the novel aspects of the present work.

4.1 Leading-order analysis

Recall that in the Chapter 3 we studied spontaneous pattern formation in the SHE (4.0.1) near the onset of instability by introducing the small parameter $0 < \epsilon \ll 1$ and applying the multiple-scales ansatz $u(x,t) = \epsilon U(x,X)$, $X = \epsilon^2 x$. Note that we are only concerned with stationary solutions in this chapter and so shall neglect time-dependence throughout. Rescaling by defining $r = \epsilon^4 r_4$, $s = \epsilon^2 s_2$ in order to obtain the

correct balance of terms, (4.0.1) therefore becomes

$$0 = \epsilon^4 r_4 U - \left[\left(1+\frac{\partial^2}{\partial x^2}\right)^2 + 4\epsilon^2\left(1+\frac{\partial^2}{\partial x^2}\right)\frac{\partial^2}{\partial x \partial X} + \epsilon^4\left(2+6\frac{\partial^2}{\partial x^2}\right)\frac{\partial^2}{\partial X^2} + 4\epsilon^6\frac{\partial^4}{\partial x \partial X^3} + \epsilon^8\frac{\partial^4}{\partial X^4}\right] U + \epsilon^4 s_2 U^3 - \epsilon^4 U^5. \tag{4.1.1}$$

A formal asymptotic analysis may now be carried out by expanding U in powers of ϵ^2 as

$$U(x,X) = \sum_{n=0}^{N-1} \epsilon^{2n} U_n(x,X) + R_N(x,X). \tag{4.1.2}$$

Note that (4.1.1) is the steady version of (3.0.7). However, whereas in that calculation we neglected terms smaller than $\mathrm{O}\left(\epsilon^2\right)$ in the asymptotic expansion of U (3.0.8), we now include higher-order terms explicitly. In particular, we include a remainder term R_N. This is because the expansion (4.1.2) is divergent when the leading-order solution U_0 is a front, and must be truncated. If this truncation is optimal then the remainder R_N will be exponentially small; the point of truncation N is as yet unknown. We shall discuss these facts in more detail shortly.

As discussed in Section 3.2 the previous chapter, the leading-order solution to (4.1.1) takes the form of slowly modulated spatial oscillations given by

$$U_0(x,X) = A_0(X)e^{ix} + A_0^*(X)e^{-ix}, \tag{4.1.3}$$

where the asterisk denotes the complex conjugate and the envelope A_0 is determined by a solvability condition arising at $\mathrm{O}\left(\epsilon^4\right)$. This appears in the form of the Ginzburg-Landau equation

$$0 = r_4 A_0 + 4\frac{\mathrm{d}^2 A_0}{\mathrm{d}X^2} + 3s_2|A_0|^2 A_0 - 10|A_0|^4 A_0, \tag{4.1.4}$$

given in unsteady form in (3.0.17). This admits a stationary front solution at

$$r_4 = r_{M,1} := -\frac{27}{160}s_2^2, \tag{4.1.5}$$

given by

$$A_0(X) = A_f(X)e^{i\phi}, \tag{4.1.6}$$

where

$$A_f(X) = \left(\frac{3}{10}\right)^{1/4} \frac{\sqrt{\mu}}{\sqrt{1+e^{\mu X}}}, \tag{4.1.7}$$

as defined in(3.2.11), with $\mu = \sqrt{-r_{M,1}}$ as found in (3.2.9). Thus $\epsilon^4 r_{M,1}$ provides a first approximation to the (unscaled) Maxwell point r_M. The real constant ϕ represents the phase of the underlying oscillations, arbitrary to all algebraic orders. By analysing the exponentially small remainder R_N in (4.1.2), we shall fix ϕ and hence derive the exponentially small parameter region in which stationary fronts exist. Note that the fact that A_f is real for real X makes the present calculation more straightforward in some respects than, for example, the quadratic-cubic SHE studied in [22].

Successive correction terms to the Maxwell point r_M may be found by writing

$$r = \sum_{n=4}^{N-1} \epsilon^{2n} r_{2n} + \epsilon^4 \delta r, \tag{4.1.8}$$

where δr is exponentially small, and continuing the calculation to higher orders. Requiring that the solution remain bounded at each order then fixes each of the r_{2n}. This has been done up to $\mathrm{O}\left(\epsilon^{14}\right)$, giving

$$\begin{aligned} r_6 &= r_{10} = r_{14} = 0, \\ r_8 &= r_{M,2} := \frac{1377}{81920000} s_2^4, \\ r_{12} &= r_{M,3} := \frac{106677}{10485760000000} s_2^6. \end{aligned} \tag{4.1.9}$$

We omit the details for the sake of brevity. Thus we have a three term expression for the Maxwell point, namely

$$r_M = \epsilon^4 r_{M,1} + \epsilon^8 r_{M,2} + \epsilon^{12} r_{M,3} + \mathrm{O}\left(\epsilon^{16}\right). \tag{4.1.10}$$

This will prove useful when we come to compare analytical and numerical results in Section 4.8. Note that every algebraic perturbation of the Maxwell point is fixed in terms of s_2, and so the exponentially small snaking region cannot be expressed using algebraic corrections alone. Thus we truncate the expansion of r (4.1.8) at the same point as the expansion of U (4.1.2), and denote the resultant remainder by δr. We derive

in Section 4.7 a condition expressing the phase ϕ of the pattern in terms of δr; hence δr provides a bifurcation parameter through which we are able to describe the snaking region.

4.2 Setting up the beyond-all-orders calculation

In light of the importance of the seemingly arbitrary phase ϕ, it is helpful to introduce

$$\tilde{x} = x + \phi, \tag{4.2.1}$$

and rewrite

$$U(x, X) = \sum_{n=0}^{N-1} \epsilon^{2n} U_n(\tilde{x}, X) + R_N(\tilde{x}, X), \tag{4.2.2}$$

$$U_0(\tilde{x}, X) = A_f(X) e^{i\tilde{x}} + A_f(X) e^{-i\tilde{x}}; \tag{4.2.3}$$

recall $A_f(X)$ is real for real X. Solutions at higher order in ϵ^2 can thus be found in terms of modulated sums of the harmonics $e^{ki\tilde{x}}$, for integer k. In this way ϕ is retained implicitly within the calculation until it can be determined.

4.2.1 The remainder equation

Given the truncated expansion (4.1.2), we can easily write down the equation for the remainder R_N by linearising the steady version of (4.1.1) around $\sum_{n=0}^{N-1} \epsilon^{2n} U_n$. This gives

$$\begin{aligned} \epsilon^4 \left(r_{M,1} + \cdots\right) R_N - \left(1 + \frac{\partial^2}{\partial \tilde{x}^2} + 2\epsilon^2 \frac{\partial^2}{\partial \tilde{x} \partial X} + \epsilon^4 \frac{\partial^2}{\partial X^2}\right)^2 R_N \\ + \epsilon^4 \left(3 s_2 U_0^2 - 5 U_0^4 + \cdots\right) R_N \sim -\epsilon^4 \delta r \left(U_0 + \cdots\right) + \textit{forcing due to truncation}. \end{aligned} \tag{4.2.4}$$

There are two components to the forcing on the right-hand side of (4.2.4). The first is due to the (exponentially small) deviation from the Maxwell point, and is given to

leading order by $-\delta r U_0$. The second is denoted here as 'forcing due to truncation', and consists of those terms which are smaller than $\mathrm{O}\left(\epsilon^{2N-2}\right)$ and therefore are not accounted for by terms of algebraic order in ϵ^2 in the expansion (4.1.2). Because (4.2.4) is linear, we can ignore this as yet unknown forcing for the moment, and are able to make valuable progress using our current knowledge. Note that, while R_N and δr are both exponentially small, there is an additional scaling of ϵ^4 in the first term of the right-hand side of (4.2.4), which is necessary for the forcing due to δr to contribute to the leading-order solvability condition, as shown in (4.2.8).

(4.2.4) remains a multiple-scales problem, and so we can solve it in the same manner as used to find U_0. Hence we expand R_N as

$$R_N = R_{N,0} + \epsilon R_{N,1} + \epsilon^2 R_{N,2} + \epsilon^3 R_{N,3} + \epsilon^4 R_{N,4} + \cdots . \tag{4.2.5}$$

where each of the $R_{N,j}$ are functions of $\tilde{x}$ and X. Note that the expansion of R_N is in powers of ϵ rather than ϵ^2. As will become apparent in Section 4.6, a rescaling of X will prove necessary in order to fully capture the effects of the as yet unknown forcing, which results in odd powers of ϵ appearing in (4.2.4), and so the remainder must be expanded in powers of ϵ if this is to be accounted for.

For now, equating terms at $\mathrm{O}\left(1\right)$ gives

$$\left(1 + \frac{\partial^2}{\partial \tilde{x}^2}\right)^2 R_{N,0} = 0, \tag{4.2.6}$$

with solution

$$R_{N,0} = S_0(X)e^{i\tilde{x}} + S_0^*(X)e^{-i\tilde{x}}, \tag{4.2.7}$$

where the asterisk denotes complex conjugation. Proceeding to higher orders in ϵ, we find that $R_{N,1}$, $R_{N,2}$ and $R_{N,3}$ are of a similar form. Finally, a solvability condition is reached at $\mathrm{O}\left(\epsilon^4\right)$, which requires that

$$r_{M,1}S_0 + 4\frac{\mathrm{d}^2 S_0}{\mathrm{d}X^2} + 6s_2 A_f^2 S_0 + 3s_2 A_f^2 S_0^* - 30A_f^4 S_0 - 20A_f^4 S_0^* = -\delta r A_f. \tag{4.2.8}$$

This has solution

$$R_{N,0}(\tilde{x},X) = \Bigg[D_1 A_f'(X) + iD_2 A_f(X) + D_3 A_f'(X) \int^X \frac{1}{A_f'(s)^2}\mathrm{d}s + iD_4 A_f(X) \int^X \frac{1}{A_f(s)^2}\mathrm{d}s + \delta r P(X) \Bigg] e^{i\tilde{x}} + \text{c.c.}, \tag{4.2.9}$$

where the D_j are arbitrary real constants and the particular integral P is

$$P(X) := -\frac{1}{8} A_f'(X) \int^X \frac{A_f(s)^2}{A_f'(s)^2}\mathrm{d}s. \tag{4.2.10}$$

The first pair of complementary functions, which are bounded in X, can be found by splitting S_0 into its real and imaginary parts and noting that A_f satisfies (4.1.7). The second pair, which are unbounded, can then readily be found using the method of reduction of order, and the particular integral P, also unbounded, by the method of variation of parameters.

Note that the third and fourth complementary functions are unbounded in X. A naive reaction to this fact would be to set D_3 and D_4 to zero. However, we shall find in Section 4.6 that the leading-order 'forcing due to truncation' results in a non-zero multiple, with coefficient dependent on ϕ, of the third complementary function being switched on as X crosses the imaginary axis from right to left. Furthermore, the particular integral P is itself unbounded as $X \to -\infty$. Therefore, if the third complementary function did not contribute then we would be left with no means by which to cancel out this growth apart from setting $\delta r = 0$, rendering the present attempt to describe the snaking region fruitless. In fact, we shall see that the correct way to ensure a uniform expansion as $X \to -\infty$ is to apply a solvability condition, which sets the coefficient of unbounded terms to zero by fixing the phase of the underlying pattern in terms of δr. This is the phase-locking mechanism responsible for the occurrence of snaking.

4.2.2 nth term equations

We can now see that if we are to fully determine the exponentially small remainders in the expansions of U and r, the 'forcing due to truncation' in (4.2.4), must be derived, as must the point of truncation N. In order to do this, we must first calculate the large-n behaviour of the asymptotic expansion.

Substituting the expansions of U and r into the steady version of (4.1.1) and equating terms at $\mathrm{O}\left(\epsilon^{2n}\right)$ provides a differential-recurrence relation for U_n, $0 \leq n \leq N-1$:

$$\begin{aligned}\left(1+\frac{\partial^2}{\partial\tilde{x}^2}\right)^2 U_n = &-4\frac{\partial^2}{\partial\tilde{x}\partial X}\left(1+\frac{\partial^2}{\partial\tilde{x}^2}\right)U_{n-1} - \frac{\partial^2}{\partial X^2}\left(2+6\frac{\partial^2}{\partial\tilde{x}^2}\right)U_{n-2}\\ &-4\frac{\partial^4}{\partial\tilde{x}\partial X^3}U_{n-3} - \frac{\partial^4}{\partial X^4}U_{n-4} + r_{M,1}U_{n-2}\\ &+\sum_{j=0}^{n-3} r_{2j+6}U_{n-j-3} + s_2\sum_{j_1=0}^{J_1}\sum_{j_2=0}^{J_2} U_{j_1}U_{j_2}U_{n-2-j_1-j_2}\\ &-\sum_{j_1=0}^{J_1}\sum_{j_2=0}^{J_2}\sum_{j_3=0}^{J_3}\sum_{j_4=0}^{J_4} U_{j_1}U_{j_2}U_{j_3}U_{j_4}U_{n-2-j_1-j_2-j_3-j_4},\end{aligned} \tag{4.2.11}$$

where

$$\begin{aligned} J_1 &= n-2, & J_2 &= n-2-j_1,\\ J_3 &= n-2-j_1-j_2, & J_4 &= n-2-j_1-j_2-j_3, \end{aligned} \tag{4.2.12}$$

and with the understanding that $U_n \equiv 0$ for $n < 0$. Now, the leading-order solution (4.1.3) comprises modulated harmonics of wavenumber ± 1. The higher-order nonlinear interactions between harmonics due to the cubic and quintic powers of U in (4.1.1) then produce harmonics of higher wavenumber; as both nonlinear terms are $\mathrm{O}\left(\epsilon^4\right)$, new harmonics appear at even orders of ϵ^2 but not odd. We therefore seek a solution in the form

$$U_n = \sum_{k=-K(n)}^{K(n)} A_{n,k}(X)e^{ik\tilde{x}}, \tag{4.2.13}$$

where

$$K(n) = \begin{cases} 2n+1, & n \text{ even},\\ 2n-1, & n \text{ odd}. \end{cases} \tag{4.2.14}$$

Note that only odd powers of $e^{i\tilde{x}}$ can occur in the solution, so $A_{n,k} = 0$ for even k.

Substituting (4.2.13) into (4.2.11) and equating powers of $e^{ik\tilde{x}}$ then gives

$$\begin{aligned}\left(1-k^2\right)^2 A_{n,k} = & -4ik\left(1-k^2\right)\frac{\mathrm{d}}{\mathrm{d}X}A_{n-1,k} - \left(2-6k^2\right)\frac{\mathrm{d}^2}{\mathrm{d}X^2}A_{n-2,k} - 4ik\frac{\mathrm{d}^3}{\mathrm{d}X^3}A_{n-3,k} \\ & - \frac{\mathrm{d}^4}{\mathrm{d}X^4}A_{n-4,k} + r_{M,1}A_{n-2,k} + \sum_{j=0}^{n-3} r_{2j+6}A_{n-j-3,k} \\ & + s_2 \sum_{j_1=0}^{J_1}\sum_{j_2=0}^{J_2}\sum_{p_1=-K(j_1)}^{K(j_1)}\sum_{p_2=-K(j_2)}^{K(j_2)} A_{j_1,p_1}A_{j_2,p_2}A_{n-2-j_1-j_2,k-p_1-p_2} \\ & - \sum_{j_1=0}^{J_1}\sum_{j_2=0}^{J_2}\sum_{j_3=0}^{J_3}\sum_{j_4=0}^{J_4}\sum_{p_1=-K(j_1)}^{K(j_1)}\sum_{p_2=-K(j_2)}^{K(j_2)}\sum_{p_3=-K(j_3)}^{K(j_3)} \\ & \sum_{p_4=-K(j_4)}^{K(j_4)} A_{j_1,p_1}A_{j_2,p_2}A_{j_3,p_3}A_{j_4,p_4}A_{n-2-j_1-j_2-j_3-j_4,k-p_1-p_2-p_3-p_4}, \end{aligned} \tag{4.2.15}$$

where $A_{n,k}$ is taken to be zero for $|k| > 2n+1$. The derivation of the $A_{n,k}$ in the large-n limit is presented in the following two sections. Unlike the quadratic-cubic case studied by Chapman and Kozyreff in [22], the leading-order solution (4.1.7) to the amplitude equation is real (up to the arbitrary rotation encapsulated by the phase-shift ϕ), a consequence of the lack of a term to break the $u \to -u$ symmetry in (4.0.1). Hence the following analysis is, in this respect, more straightforward than their work. However, the higher-order nonlinearities in the SHE make some aspects of the calculation more complicated; in particular, there are eight nested summations in the equation for the large-n amplitudes (4.2.15), rather than four in [22].

4.3 Large-n behaviour near the complex singularities

We are now in possession of enough information to seek a solution to (4.2.15) in the large-n limit. Firstly, we observe that the leading-order envelopes $A_{0,\pm1} = A_f$, given in (4.1.7), have infinitely many singularities on the imaginary axis, at $X = X_m := (2m+1)i\pi/\mu$, for $m \in \mathbb{Z}$. Moreover, in light of (4.2.11), we can see that in order to find U_n then U_{n-l} must be differentiated l times with respect to X, for $l = 1,2,3,4$. Therefore, as $U_0 = \mathrm{O}\left((X-X_m)^{-1/2}\right)$ as $X \to X_m$, we expect that $U_n = \mathrm{O}\left((X-X_m)^{-n-1/2}\right)$ as $X \to X_m$. These two facts taken together indicate that the asymptotic expansion is

divergent and each term in the expansion must consist of a factorial over a power, a feature generic to such singular perturbation problems [1, 51]. The expansion must therefore be truncated in order to retain uniformity. If we truncate after the least term, the remainder is exponentially small; thus it is the presence of singularities in the leading-order solution that is responsible for the exponentially small tail. This in itself is well known (see, for example, [5]); it is only with the advent of techniques developed specifically to carry out calculations beyond all algebraic orders and explicitly derive the exponentially small remainder [1, 7, 51] that the connection has become clear [56].

Although we are ultimately concerned with the behaviour of the system on the real line, we shall start by solving (4.2.15) close to its complex singularities, as doing so will elucidate the more general behaviour. In light of the above discussion, and restricting our attention for the moment to singularities in the upper half-plane by assuming $m \geq 0$, we define the constants $B_{n,k}$ by

$$A_{n,k} \sim \frac{B_{n,k}}{(X - X_m)^{n+1/2}} \tag{4.3.1}$$

as $X \to X_m$. In particular, because $A_{0,\pm 1} = A_f$, we have

$$B_{0,\pm 1} = -i \left(\frac{3}{10} \right)^{1/4}. \tag{4.3.2}$$

Note the minus sign in (4.3.2) arises due to the choice of the positive square root in (4.1.7) and ensuring that the necessary branch cuts do not cross the real line. By symmetry, the solution at $X = -X_m$ is then simply the complex conjugate of that at $X = +X_m$. Taking the leading-order approximation in powers of $(X - X_m)$ of (4.2.15) therefore provides a recurrence relation in the $B_{n,k}$. Furthermore, the factorial-over-power nature of the $A_{n,k}$ motivates the ansatz

$$B_{n,k} \sim \kappa^n \Gamma\left(n + \alpha_k\right) \left(a_k + \frac{1}{n} b_k + \frac{1}{n^2} c_k + \cdots \right) \tag{4.3.3}$$

as $n \to \infty$, familiar to such beyond-all-orders methods [1, 51]. The large-n limit has been exploited here in order to write down all n-dependence explicitly, thus ensuring that κ, α_k, a_k, b_k and c_k are independent of n; these unknowns remain to be found.

Upon substitution of the ansatz (4.3.1), (4.2.15) becomes

$$\begin{aligned}\left(1-k^2\right)^2 B_{n,k} = {} & 4ik\left(1-k^2\right)\left(n-\frac{1}{2}\right)B_{n-1,k} - \left(2-6k^2\right)\left(n-\frac{1}{2}\right)\left(n-\frac{3}{2}\right)B_{n-2,k} \\ & + 4ik\left(n-\frac{1}{2}\right)\left(n-\frac{3}{2}\right)\left(n-\frac{5}{2}\right)B_{n-3,k} \\ & - \left(n-\frac{1}{2}\right)\left(n-\frac{3}{2}\right)\left(n-\frac{5}{2}\right)\left(n-\frac{7}{2}\right)B_{n-4,k} \\ & - \sum_{j_1=0}^{n-2}\sum_{j_2=0}^{n-2-j_1}\sum_{j_3=0}^{n-2-j_1-j_2}\sum_{j_4=0}^{n-2-j_1-j_2-j_3}\sum_{p_1=-K(j_1)}^{K(j_1)}\sum_{p_2=-K(j_2)}^{K(j_2)}\sum_{p_3=-K(j_3)}^{K(j_3)} \\ & \sum_{p_4=-K(j_4)}^{K(j_4)} B_{j_1,p_1}B_{j_2,p_2}B_{j_3,p_3}B_{j_4,p_4}B_{n-2-j_1-j_2-j_3-j_4,k-p_1-p_2-p_3-p_4}, \end{aligned} \tag{4.3.4}$$

as $X \to X_m$. Note that the dominant balance is between the left-hand side of (4.2.15), the four terms involving derivatives and the quintic term; neither the cubic term nor that containing the expansion of r contribute at leading order in $(X - X_m)$.

To solve (4.3.4), we order the wavenumbers k according to the size of the offsets α_k by defining k_i for $i = 1, 2, 3, \ldots$ so that $\alpha_{k_1} > \alpha_{k_2} > \alpha_{k_3} > \cdots$. The leading-order contribution to (4.3.4) for $k = k_1$ therefore comprises only the linear terms, as these are $\mathrm{O}\left(\Gamma\left(n + \alpha_{k_1}\right)\right)$, whereas the quintic terms are at most $\mathrm{O}\left(\Gamma\left(n - 2 + \alpha_{k_1}\right)\right)$. Dividing through by $\kappa^{n-4}\Gamma\left(n + \alpha_{k_1}\right)$, we obtain the eigenvalue equation

$$\left[(1-k_1^2)^2\kappa^4 - 4ik_1(1-k_1^2)\kappa^3 + (2-6k_1^2)\kappa^2 - 4ik_1\kappa + 1\right] a_{k_1} = 0. \tag{4.3.5}$$

Requiring non-zero a_{k_1}, this provides a quadratic polynomial in κ if $|k_1| = 1$, and a quartic polynomial otherwise. If $k_1 = 1$, (4.3.5) has the repeated root $\kappa = -i/2$, if $k_1 = -1$ it has the repeated root $\kappa = i/2$, and if $|k_1| > 1$ it has the repeated roots $\kappa = -i/(k_1 + 1), -i/(k_1 - 1)$. As each wavenumber k is odd, we can without loss of generality set $\kappa = -i/2q$ for $|q| \in \{1, 2, \ldots, (K(n) - 1)/2\}$, where $K(n)$ is the maximum positive wavenumber as defined in (4.2.14). Then, for a particular eigenvalue $\kappa = -i/2q$, the dominant wavenumbers are given by $k_1 = 2q \pm 1$. Therefore we set $\alpha_{2q\pm1} = \alpha$, for some constant α to be determined.

Proceeding to $k = k_2 \neq 2q \pm 1$, we see that the leading-order linear terms (4.3.5) do not

sum to zero $\kappa = -i/2q$. In order for $a_{k_2} \neq 0$ then (4.3.5) cannot be the leading-order contribution; there must be a leading-order balance between linear and quintic terms. The largest possible quintic terms arising from the nested summations in (4.3.4) are $\mathrm{O}\left(\Gamma\left(n-2+\alpha\right)\right)$. These occur either when one of the index pairs $(j_i, p_i) = (n-2, 2q \pm 1)$, or when all four of the indices j_i are zero (giving $n-2-j_1-j_2-j_3-j_4 = n-2$) and the indices p_i satisfy $k - p_1 - p_2 - p_3 - p_4 = 2q \pm 1$, for $i = 1, 2, 3, 4$. Satisfying first the conditions on the j_i and recalling that $B_{0,1} = B_{0,-1}$ (see (4.3.2)), the largest terms are thus

$$-5B_{0,1}^4\left(B_{n-2,k_2-4} + 4B_{n-2,k_2-2} + 6B_{n-2,k_2} + 4B_{n-2,k_2+2} + B_{n-2,k_2+4}\right). \tag{4.3.6}$$

Hence, as $k_2 \neq k_1$, a balance between linear and quintic terms is achieved when at least one of $\alpha_{k_2\pm2}$ or $\alpha_{k_2\pm4}$ are equal to $\alpha_{k_1} = \alpha$. This is the case when $k_2 + \sigma = 2q \pm 1$, where $\sigma = \pm2, \pm4$, i.e. for $k_2 = 2q \pm 3, 2q \pm 5$. We shall not calculate the $a_{k_2} \neq 0$ explicitly as we are concerned only with leading-order behaviour; the important detail is the offsets $\alpha_{2q\pm3} = \alpha_{2q\pm5} = \alpha - 2$. By continuing in this manner, one may show that $\alpha_{2q\pm7} = \alpha_{2q\pm9} = \alpha - 4$, etc.

Now we have a compete description of the offsets α_k we know how the $B_{n,k}$ scale according to their Γ-functions. Hence we are able to determine α. Concentrating on the dominant harmonics for each eigenvalue, we set $k = k_1 = 2q \pm 1$ and continue to higher orders in $1/n$ in (4.3.4). We find that $\mathrm{O}\left(1/n\right)$ terms vanish, but at $\mathrm{O}\left(1/n^2\right)$ we have

$$\begin{aligned} 0 &= \left(-4\alpha^2 + 8\alpha + 6\right)a_{2q+1} + 6a_{2q-1}, \\ 0 &= \left(-4\alpha^2 + 8\alpha + 6\right)a_{2q-1} + 6a_{2q+1}. \end{aligned} \tag{4.3.7}$$

Non-trivial solutions exist provided that the solvability condition

$$\left(-4\alpha^2 + 8\alpha + 6\right)^2 = 36 \tag{4.3.8}$$

is met. Thus we must have $\alpha = 3, 2, 0$ or -1. We shall only consider $\alpha = 3$, as the other values, being smaller, are subdominant; this gives $a_{2q+1} = a_{2q-1} = \lambda_q$, say.

We have finally arrived at an expression for the leading-order behaviour of U_n as $X \to X_m$ and $n \to \infty$. For a particular $|q| \in \{1, 2, \ldots, (K(n)-1)/2\}$, this is

$$U_n \sim \frac{(-i)^n \Gamma(n+3)\, \lambda_q}{(2q)^n (X - X_m)^{n+1/2}} \left[e^{(2q+1)i\tilde{x}} + e^{(2q-1)i\tilde{x}} \right], \tag{4.3.9}$$

where the λ_q are as yet unknown (and in general, complex) constants. The full solution near X_m, incorporating the leading order coefficient of each harmonic $k \in \{-K(n), \ldots, K(n)\}$, is thus given by summing (4.3.9) over all q. By symmetry, the solution near to the conjugate singularity at $-X_m$ is simply the sum over all q of the complex conjugate of (4.3.9). Note that the dominant contributions come from the singularities closest to the real line, namely those at $X = X_0 = i\pi/\mu$ and $X = X_{-1} = -i\pi/\mu$; the dominant eigenvalue is given in both cases by $|q| = 1$.

4.4 Calculating $\lambda_{\pm 1}$

An inconvenient consequence of the linear nature of the large-n calculation is that the constants λ_q remain undetermined. In particular, the $\lambda_{\pm 1}$ are unknown. As $\lambda_{\pm 1}$ correspond to the minimum value of $|q|$ in (4.3.9), and therefore determine the dominant contribution to U_n, they are crucial for a quantitative expression for the width of the snaking region (see Section 4.7). Fortunately, we do in fact possess a means by which the λ_q can be determined; the recurrence relation (4.3.4). In light of the large-n solution (4.3.9), the ansatz (4.3.3) can be rearranged to give

$$\begin{aligned} \lambda_{\pm 1} &= \lim_{n\to\infty} \frac{(\pm 2i)^n B_{n,\pm 1}}{\Gamma(n+3)}, \\ \lambda_{(k\mp 1)/2} &= \lim_{n\to\infty} \frac{((k\mp 1)i)^n B_{n,k}}{\Gamma(n+3)}, \quad \pm k \in \{3, 5, \ldots, K(n)\}. \end{aligned} \tag{4.4.1}$$

Consequently, if (4.3.4) can be iterated to a large enough value of n, the ansatz (4.3.3) holds and the λ_q are given by (4.4.1).

In order to begin iterating (4.3.4) to large values of n, we first require $B_{0,\pm 1}$ and $B_{1,\pm 1}$. All $B_{n,k}$ with $|k| \neq 1$ are zero for $n = 0, 1$, and so these four constants provide the

starting point from which all $B_{n,k}$ for $n \geq 2$ can be found. As $A_{0,\pm 1} = A_f(X)$, we know that $B_{0,\pm 1} = -i\,(3/10)^{1/4}$ (see (4.3.2)). Furthermore, expressions for the $B_{1,\pm 1}$ are easily found by continuing the multiple-scales calculation outlined in Section 4.1 to $\mathrm{O}\left(\epsilon^6\right)$, producing a solvability condition which can be solved to give $A_{1,\pm 1}$. We omit this calculation for the sake of brevity and merely present the result, consisting of two complementary functions and a particular integral, namely,

$$A_{1,\pm 1}(X) = aA_f'(X) \pm ibA_f(X) \pm \frac{i}{2}A_f(X)\int^X \frac{2A_f(s)A_f''(s) - A_f'(s)^2}{A_f(s)^2}\mathrm{d}s, \qquad (4.4.2)$$

where a and b are arbitrary real constants. In view of the invariance of the SHE (4.0.1) under translation, both constants may be set to zero with no loss of generality. Hence

$$B_{1,\pm 1} = \mp\frac{5}{8}\left(\frac{3}{10}\right)^{1/4}, \qquad (4.4.3)$$

and we possess the requisite information in order to iterate (4.3.4).

We note here that, while (4.3.4) gives $B_{n,k}$ directly for $|k| \neq 1$, the situation is slightly more complicated for $k = \pm 1$. Because the coefficients of $B_{n,\pm 1}$ and $B_{n-1,\pm 1}$ vanish, the quintic nested summations come into play, resulting in a pair of coupled equations in $B_{n-2,\pm 1}$. These must be solved in order to obtain explicit expressions for the $B_{n-2,\pm 1}$ in terms of the $B_{m,k}$ for $0 \leq m \leq n-3$.

In practice, solving the recurrence relation is computationally intensive for large values of n, due to the presence of the nested summations and the increasing numbers of harmonics at each order. However, by iterating the recurrence relation up to $n = 30$ and using polynomial interpolation in inverse powers of n on $B_{n,1}$ and $B_{n,3}$ for $n = 20, \ldots, 30$, two estimates of the large-n limit (4.4.1) for $q = 1$ have been calculated using floating point arithmetic (λ_1 being the most important unknown constant, corresponding as it does to the dominant eigenvalues). Polynomial interpolation on the $B_{n,1}$ yields the estimate $\lambda_1 \approx -0.10190i$, while interpolation on the $B_{n,3}$ yields $\lambda_1 \approx -0.10084i$. The data and polynomial approximation are shown in figure 4.1, and compared with a further five data points beyond $n = 30$, with good visual agreement. Taking the average of

these estimates gives

$$\lambda_1 \approx -0.101i. \tag{4.4.4}$$

This value of λ_1 will prove essential in allowing the accurate assessment of the present work against numerical calculations.

λ_{-1} can be easily found by noting two convenient properties of (4.3.4). Firstly, (4.3.4) is invariant under the transformation $B_{n,k} \to -B^*_{n,-k}$. As we also have $B_{0,1} = -B^*_{0,-1}$ and $B_{1,1} = -B^*_{1,-1}$, then $B_{n,k} = -B^*_{n,-k}$ for all n and k. We can infer from this that $\lambda_q = -\lambda^*_{-q}$ in (4.3.9). Secondly, we can see from inspection of $B_{0,\pm1}$, $B_{1,\pm1}$ and (4.3.4) that the $B_{n,k}$ are imaginary for even n and real for odd n. Thus λ_q is imaginary, as we have already seen by iteration of (4.3.4), and we have $\lambda_q = \lambda_{-q}$ for all q; in particular $\lambda_1 = \lambda_{-1}$. These relationships are also useful when iterating (4.3.4), as they provide a simple method of checking the validity of one's results.

Note that the amplitude of the large-wavenumber harmonics rapidly becomes negligible as (4.3.4) is iterated. This can be easily seen by considering (4.3.9) for large q. The iteration process could then, in principle, be carried forward to much greater values of n than has been done here, simply by truncating the nested sums to ignore the large-wavenumber harmonics. However, as can be seen from figure 4.1, convergence is very slow, so the resultant marginal gains in accuracy are unlikely to be worth the extra computational time required.

4.5 Large-n behaviour on the real line

We shall now derive a more general solution to (4.2.15) in the large-n limit, in particular one which is valid on the real line. The factorial-over-power nature of the solution, as discussed at the beginning of the last section, still holds. We extend the solution away

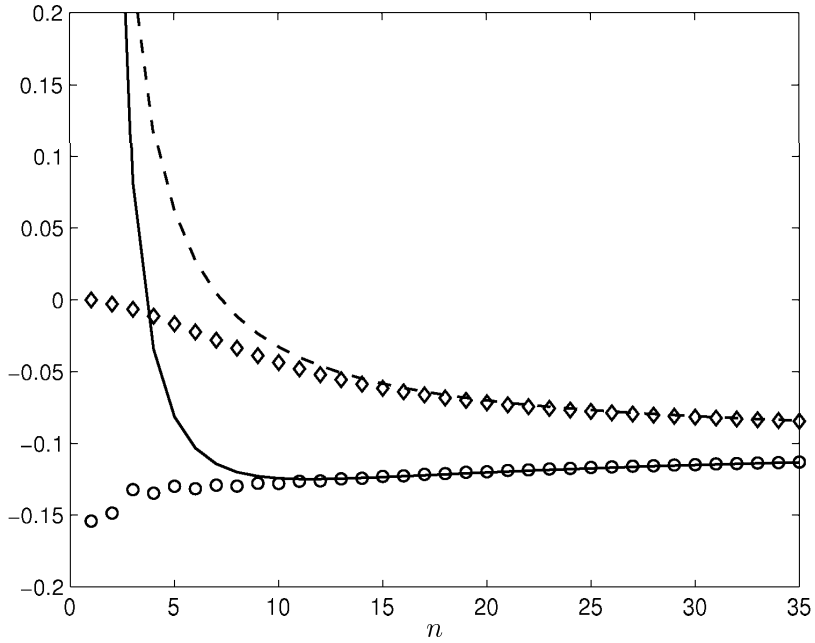

Figure 4.1: *Results of evaluating the $B_{n,k}$ by iteration of (4.3.4). The data points represent $\Im[(2i)^n B_{n,k}/\Gamma(n+3)]$ for $k = 1$ (circles) and $k = 3$ (diamonds). The lines plot a second-order polynomial in inverse powers of n, given by interpolation using these data for $n = 20, \ldots, 30$. The solid line represents this for $k = 1$, and dashed line for $k = 3$. The data for $n = 30, \ldots, 35$ are also plotted, indicating the good agreement between the predictions from interpolation and the direct calculation.*

from the singularities at $X = X_m$ by means of the ansatz

$$A_{n,k}(X) \sim \frac{\Gamma(n+\beta_k)}{F(X)^{n+\beta_k}} \left(f_k(X) + \frac{1}{n} g_k(X) + \frac{1}{n^2} h_k(X) + \cdots \right), \tag{4.5.1}$$

as $n \to \infty$. Here $F(X)$, β_k, $f_k(X)$, $g_k(X)$ and $h_k(X)$ are independent of n and are to be determined. Note the β_k in the exponent of $F(X)$; this provides exact cancellation with the Γ-function when differentiating with respect to X in (4.2.15).

As in Section 4.3, $F(X)$ is determined by the leading-order approximation of (4.2.15), with the assumption that β_k is maximal, i.e. by considering the dominant modes in U_n. The largest terms are $\mathrm{O}(\Gamma(n+\beta_k))$, and so consist of the left-hand side of (4.2.15) and the terms from the right-hand side in which the first derivative of $F(X)$ appears,

yielding

$$0 = \left[\left(1-k^2\right)^2 - 4ik\left(1-k^2\right)F_X + \left(2-6k^2\right)F_X^2 - 4ikF_X^3 + F_X^4\right] f_k. \tag{4.5.2}$$

This is precisely the eigenvalue equation (4.3.5) which determined κ in the Section 4.3, with $F_X = 1/\kappa$. Thus $F_X = 2iq$, where $|q| \in \{1, 2, \ldots, (K(n)-1)/2\}$, with the dominant modes given by $k = 2q+1, 2q-1$ and $\beta_{2q\pm1} = \beta$, $\beta_{2q\pm5} = \beta_{2q\pm3} = \beta - 2$, etc.

Now, in light of (4.2.15), $A_{n,k}$ must have the same singularities as $A_{0,\pm1} = A_f$, which can be ensured by the choice of the constant of integration in F. Therefore we set

$$F(X) = 2iq\left(X - X_m\right), \tag{4.5.3}$$

for $m \in \mathbb{N} \cup \{0\}$, as we can regain the contribution due to singularities in the lower half-plane by symmetry. $A_{n,k}$ is then given by the sum of the contributions from each singularity X_m, plus their complex conjugates.

Dividing (4.2.15) through by $\Gamma(n+\beta)$ and continuing to $\mathrm{O}\left(1/n\right)$, we find that there is exact cancellation, as was seen in the Section 4.3, and so we must proceed to $\mathrm{O}\left(1/n^2\right)$ to make further progress. Here the largest terms in the two sets of nested summations contribute, along with the term with coefficient $r_{M,1}$, resulting in the coupled ODEs

$$0 = 4\frac{\mathrm{d}^2 f_{2q+1}}{\mathrm{d}X^2} + r_{M,1}f_{2q+1} + 6s_2A_f^2f_{2q+1} - 30A_f^4f_{2q+1} + 3s_2A_f^2f_{2q-1} - 20A_f^4f_{2q-1}, \tag{4.5.4}$$

$$0 = 4\frac{\mathrm{d}^2 f_{2q-1}}{\mathrm{d}X^2} + r_{M,1}f_{2q-1} + 6s_2A_f^2f_{2q-1} - 30A_f^4f_{2q-1} + 3s_2A_f^2f_{2q+1} - 20A_f^4f_{2q+1}. \tag{4.5.5}$$

Because $A_f(X)$ satisfies (4.1.4), it is immediately obvious that one set of solutions are

$$f_{2q+1} = -f_{2q-1} = A_f(X), \tag{4.5.6}$$

$$f_{2q+1} = f_{2q-1} = A_f'(X). \tag{4.5.7}$$

The second set of solutions is readily found using the method of variation of parameters, and is given by

$$f_{2q+1} = -f_{2q-1} = A_f(X)\int_{X_m}^{X} \frac{1}{A_f(s)^2}\mathrm{d}s =: G_m(X), \tag{4.5.8}$$

$$f_{2q+1} = f_{2q-1} = A_f'(X)\int_{X_m}^{X} \frac{1}{A_f'(s)^2}\mathrm{d}s =: H_m(X), \tag{4.5.9}$$

where the lower limit of integration is chosen in order to be able to match between the outer solution derived here and the inner solution (4.3.9) derived in the Section 4.3.

Now, as $X \to X_m$, remembering that each singularity is in the upper half-plane, we have

$$A_f \sim -i\left(\frac{3}{10}\right)^{1/4}\frac{1}{(X-X_m)^{1/2}}, \tag{4.5.10}$$

$$A_f' \sim \frac{i}{2}\left(\frac{3}{10}\right)^{1/4}\frac{1}{(X-X_m)^{3/2}}, \tag{4.5.11}$$

$$G_m \sim \frac{i}{2}\left(\frac{10}{3}\right)^{1/4}(X-X_m)^{3/2}, \tag{4.5.12}$$

$$H_m \sim -\frac{i}{2}\left(\frac{10}{3}\right)^{1/4}(X-X_m)^{5/2}. \tag{4.5.13}$$

Matching the outer solution given above with the inner solution (4.3.9) requires equal powers of $(X - X_m)$, thus fixing β. Respectively, the solutions above give $\beta = 0, -1, 2$ or 3, corresponding to the values of α derived in Section 4.3. As the value of β which results in the largest argument of the Γ-function in (4.5.1) dominates, we set $\beta = 3$ and discount the other solutions. This gives the contribution to U_n for $n \to \infty$ from the singularity X_m, $m \geq 0$, for a particular $|q| \in \{1, 2, \ldots, (K(n)-1)/2\}$, as

$$U_n \sim \frac{(-i)^n\Gamma(n+3)}{(2q)^n(X-X_m)^{n+3}}\Lambda_q H_m(X)\left[e^{(2q+1)i\tilde{x}} + e^{(2q-1)i\tilde{x}}\right], \tag{4.5.14}$$

where

$$\Lambda_q = 2i\left(\frac{3}{10}\right)^{1/4}\lambda_q. \tag{4.5.15}$$

As λ_q is imaginary, Λ_q is real. From our estimate for $\lambda_{\pm 1}$ given in (4.4.4), we have $\Lambda_{\pm 1} \approx -0.15$.

By symmetry, the contribution from the conjugate singularity at $X = -X_m$ is simply the complex conjugate of (4.5.14). The full solution, consisting of the sum of the contributions from each singularity, for each q, is therefore real for real X, as would be expected. Now, because n is large, the dominant contribution to U_n on the real line

comes from those singularities closest to the real line, taking the minimum value of q. Thus U_n is asymptotic on the real line to (4.5.14) with $m = 0$ and $|q| = 1$, plus its complex conjugate, and the dominant harmonics are $e^{\pm i\tilde{x}}$ and $e^{\pm 3i\tilde{x}}$. Note that this is in contrast to the quadratic-cubic SHE, in which the dominant modes are the constant mode $e^{0i\tilde{x}}$ and $e^{\pm 2i\tilde{x}}$ [22], and is due to the fact that only odd powers of u appear in the original equation (4.0.1).

4.6 Optimal truncation and the remainder

Now that the large n terms in the expansion of U are known, we seek to truncate the expansion optimally, that is, to truncate in such a manner as to ensure the remainder is not algebraically small but exponentially small. To this end, we must consider each contribution (4.5.14) to U_n separately for each singularity X_m and each eigenvalue q. Truncating after N terms, N is given, in light of (4.3.9) and (4.5.14), by minimising

$$\left| \frac{\epsilon^{2n}\Gamma(n+3)}{(2q)^n (X - X_m)^{n+3}} \right| \tag{4.6.1}$$

with respect to n and evaluating at $n = N - 1$. Approximating the Γ-function using Stirling's formula, the minimum of (4.6.1) is at

$$\frac{\mathrm{d}}{\mathrm{d}n} \left(\frac{\epsilon^{2n}\sqrt{2\pi}(n+3)^{n+5/2}e^{-n-3}}{(2|q|)^n \left|X - X_m\right|^{n+3}} \right) = 0. \tag{4.6.2}$$

Collecting exponents gives

$$\frac{\mathrm{d}}{\mathrm{d}n} \exp\left[n \ln\left(\frac{\epsilon^2 (n+3)}{2|q(X - X_m)|} \right) - n + \frac{5}{2}\ln(n+3) \right] = 0; \tag{4.6.3}$$

setting $n = N - 1$, we therefore require

$$\ln\left(\frac{\epsilon^2 (N+2)}{2|q(X - X_m)|} \right) = 0, \tag{4.6.4}$$

which gives

$$N \sim \frac{2|q(X - X_m)|}{\epsilon^2} + \nu, \tag{4.6.5}$$

for a particular q and m, where $\nu \in [-2.5, -1.5)$ is added to ensure that $N-1$ is the integer closest to the minimum of (4.6.1). Note that N depends upon ϵ, X, X_m and q. Recalling that U and r are given by the truncated expansions (4.1.2) and (4.1.8), respectively, we are now in a position to derive the exponentially small remainder R_N, which will in turn give us the exponentially small deviation from the Maxwell point δr.

Substitution of (4.1.2) into (4.1.1) gives the equation for $R_N(\tilde{x}, X)$,

$$\begin{aligned}\epsilon^4 r_{M,1} R_N - \left(1 + \frac{\partial^2}{\partial \tilde{x}^2} + 2\epsilon^2 \frac{\partial^2}{\partial \tilde{x} \partial X} + \epsilon^4 \frac{\partial^2}{\partial X^2}\right)^2 R_N + \epsilon^4 \left(3 s_2 U_0^2 - 5 U_0^4\right) R_N + \cdots \\ \sim -\epsilon^{2N} \left(1 + \frac{\partial^2}{\partial \tilde{x}^2}\right)^2 U_N - \epsilon^{2N+2} \left[\left(1 + \frac{\partial^2}{\partial \tilde{x}^2}\right)^2 U_{N+1} \right. \\ \left. + 4 \frac{\partial^2}{\partial \tilde{x} \partial X} \left(1 + \frac{\partial^2}{\partial \tilde{x}^2}\right) U_N \right] + \epsilon^{2N+4} \left[4 \frac{\partial^4}{\partial \tilde{x} \partial X^3} U_{N-1} + \frac{\partial^4}{\partial X^4} U_{N-2}\right] \\ + \epsilon^{2N+6} \frac{\partial^4}{\partial X^4} U_{N-1} - \epsilon^4 \delta r U_0 + \cdots . \end{aligned} \tag{4.6.6}$$

Here, only the leading-order forcing has been retained. The process of determining which terms contribute at leading order, while somewhat laborious, is made much easier by considering the factor of $(X - X_m)^{-N-3}$ in the solution (4.5.14) for U_n, which gives $\partial_X = \mathrm{O}(N) = \mathrm{O}\left(1/\epsilon^2\right)$. Once the dominant contributions have been found, the forcing can then be further simplified by use of (4.2.11), resulting in (4.6.6).

The complementary functions of (4.6.6) and particular integral due to the deviation from the Maxwell point δr have already been derived in Section 4.2.1. However, we are now able to elucidate the effect on R_N of the previously unconsidered forcing. This will turn out the be maximal near Stokes lines, and require a rescaling of the slow variable X in their vicinity. This in turn will enable us to explicitly observe the switching on of the unbounded complementary function of (4.6.6) via error function smoothing.

4.6.1 The remainder near the Stokes lines

Because (4.6.6) is linear, we can consider the contribution to the forcing for each q and each X_m separately. For a particular q and X_m, then, the right-hand side (RHS) of (4.6.6) is

$$\text{RHS} \sim \frac{\epsilon^{2N}(-i)^N\Gamma(N+3)}{(2q)^N(X-X_m)^{N+3}}\Lambda_q H_m(X)\left[c_{2q+1}(X;N,\epsilon)e^{(2q+1)i\tilde{x}}+c_{2q-1}(X;N,\epsilon)e^{(2q-1)i\tilde{x}}\right], \tag{4.6.7}$$

where

$$\begin{aligned} c_k(X;N,\epsilon) \sim & -\left(1-k^2\right)^2+\left[\frac{i}{2q}\left(1-k^2\right)^2+4ik\left(1-k^2\right)\right]\frac{\epsilon^2N}{X-X_m} \\ & +\left(8qk-4q^2\right)\frac{\epsilon^4N^2}{(X-X_m)^2}+2qi\frac{\epsilon^6N^3}{(X-X_m)^3}, \end{aligned} \tag{4.6.8}$$

for $k = 2q \pm 1$. Note that, because $N = \mathrm{O}\left(1/\epsilon^2\right)$, $\mathrm{d}(X-X_m)^{-N}/\mathrm{d}X = \mathrm{O}(N) = \mathrm{O}\left(1/\epsilon^2\right)$, whereas $\mathrm{d}H_m/\mathrm{d}X = \mathrm{O}(1)$. Therefore the c_k are $\mathrm{O}(1)$; moreover, derivatives of $H_m(X)$ do not contribute at leading order.

It is convenient to write

$$2q(X-X_m) = \rho e^{i\theta}, \tag{4.6.9}$$

which gives

$$N \sim \rho/\epsilon^2+\nu. \tag{4.6.10}$$

Note that ρ and θ depend implicitly on X_m and q. Using Stirling's approximation to rewrite the Γ-function, the prefactor of (4.6.7) can be written as

$$\begin{aligned} \frac{\epsilon^{2N}(-i)^N\Gamma(N+3)}{(2q)^N(X-X_m)^{N+3}} &\sim \frac{\epsilon^{2N}(-i)^N\sqrt{2\pi}(N+3)^{N+5/2}e^{-(N+3)}}{(2q)^N(X-X_m)^{N+3}} \\ &\sim \frac{\sqrt{2\pi}\epsilon^{-5}(-i)^N}{(2q)^{-3}\sqrt{\rho}}\left(\frac{\epsilon^2(\rho/\epsilon^2+\nu+3)}{\rho}\right)^{\rho/\epsilon^2+\nu+5/2}e^{-(\rho/\epsilon^2+\nu+3)}e^{-iN\theta} \\ &\sim \frac{8\sqrt{2\pi}q^3}{\epsilon^5\sqrt{\rho}}e^{\left(\rho/\epsilon^2+\nu+5/2\right)\ln\left(1+\epsilon^2(\nu+3)/\rho\right)}e^{-\left(\rho/\epsilon^2+\nu+3\right)}e^{-iN(\pi/2+\theta)} \\ &\sim \frac{8\sqrt{2\pi}q^3}{\epsilon^5\sqrt{\rho}}e^{-iN(\pi/2+\theta)}e^{-\rho/\epsilon^2}. \end{aligned} \tag{4.6.11}$$

Thus the right-hand side of (4.6.6) is exponentially small in ϵ.

Now,

$$e^{-\rho/\epsilon^2} = e^{-2|q(X-X_m)|/\epsilon^2} = e^{-2|q(x-X_m/\epsilon^2)|}, \tag{4.6.12}$$

so we can see that the exponential smallness is a consequence of the singularities X_m, and a non-oscillatory x-dependence has been recovered. Recalling that X_m is in the upper half-plane, we have

$$e^{2qi\tilde{x}} = e^{2qi(x+\phi)} = e^{2qi(X-X_m+X_m)/\epsilon^2} e^{2qi\phi} = e^{i\rho e^{i\theta}/\epsilon^2} e^{-2q|X_m|/\epsilon^2} e^{2qi\phi}. \tag{4.6.13}$$

Therefore, considering the real part of the exponent in (4.6.7), we see that the forcing is maximal when

$$-\frac{1}{\epsilon^2}\left(\rho + \rho\sin\theta + 2q|X_m|\right) = 0. \tag{4.6.14}$$

For fixed ρ, this occurs at $\theta = -\pi/2$, the Stokes line. Certain contributions to the remainder are 'switched on' as Stokes lines are crossed, in a sense to be detailed presently. Note there are two Stokes lines emanating from each X_m, one for $q > 0$ and one for $q < 0$. As the present calculation is ultimately concerned with the behaviour on the real line, only those Stokes lines which intersect it need be considered. Focusing as usual on singularities in the upper half-plane, we see that the Stokes lines of importance are those for $q > 0$. The contributions from the lower singularities (in which case the Stokes lines of importance are those with $q < 0$) can then be retrieved by taking the complex conjugate.

In order to capture the dynamics in the neighbourhood of the pertinent Stokes lines, we rescale θ as $\theta = -\pi/2 + \eta(\epsilon)\hat{\theta}$, where the exact scaling $\eta(\epsilon)$ is to be determined. Including a factor of $e^{2qi\tilde{x}}$, rewritten in terms of X as in (4.6.13), we write the prefactor of (4.6.7) as

$$\begin{aligned}
&\frac{\epsilon^{2N}(-i)^N\Gamma(N+3)}{(2q)^N(X-X_m)^{N+3}} e^{2qi\tilde{x}} \\
&\qquad\sim \frac{8\sqrt{2\pi}q^3}{\epsilon^5\sqrt{\rho}} e^{-i\eta\hat{\theta}\left(\rho/\epsilon^2+\nu+3\right)} e^{-\rho/\epsilon^2} e^{\rho(1+i\eta\hat{\theta}-\eta^2\hat{\theta}^2/2)/\epsilon^2} e^{-2q|X_m|/\epsilon^2} e^{2qi\phi} \\
&\qquad\sim \frac{8\sqrt{2\pi}e^{3i\pi/2}q^3}{\epsilon^5\sqrt{\rho}} e^{-i\eta\hat{\theta}(\nu+3)} e^{-q\rho\eta^2\hat{\theta}^2/2\epsilon^2} e^{-2q|X_m|/\epsilon^2} e^{2qi\phi}.
\end{aligned} \tag{4.6.15}$$

This suggests the scaling $\eta(\epsilon) = \epsilon$, yielding

$$\frac{\epsilon^{2N}(-i)^N\Gamma(N+3)}{(2q)^N(X-X_m)^{N+3}}e^{2qi\tilde{x}} \sim \frac{8\sqrt{2\pi}e^{3i\pi/2}q^3}{\epsilon^5\sqrt{\rho}}e^{-\rho\hat{\theta}^2/2}e^{-2q|X_m|/\epsilon^2}e^{2qi\phi}, \tag{4.6.16}$$

at leading order. Thus we see that the forcing is maximal at $\hat{\theta} = 0$, i.e. on the Stokes line, but rapidly decays as $|\hat{\theta}|$ increases. Thus the maximal change in R_N occurs in the region $\hat{\theta} = \mathrm{O}(1)$. This we shall henceforth refer to as the Stokes layer.

With this scaling of θ, the coefficient functions $c_{2q\pm1}$ become

$$c_{2q\pm1} \sim -16q^2\epsilon i\hat{\theta}, \tag{4.6.17}$$

$H_m(X)$ is evaluated on the Stokes line to be

$$H_m(X) = H_m\left(X_m - \frac{i\rho e^{\epsilon i\hat{\theta}}}{2q}\right) = H_m\left(X_m - \frac{i\rho}{2q}\right) + \frac{\epsilon\rho}{2q}\hat{\theta}H_m'\left(X_m - \frac{i\rho}{2q}\right) + \mathrm{O}\left(\epsilon^2\right) \tag{4.6.18}$$

and ∂_X is

$$\frac{\partial}{\partial X} = -\frac{2qie^{-i\theta}}{\rho}\frac{\partial}{\partial\theta} = \frac{2qe^{-\epsilon i\hat{\theta}}}{\epsilon\rho}\frac{\partial}{\partial\hat{\theta}}. \tag{4.6.19}$$

The aim of the present step in the calculation is to observe the switching on of previously subdominant terms. As this occurs as Stokes lines are crossed, variations in the radial direction are of no concern. It is therefore sufficient to treat ρ as constant and concentrate solely on variations in the azimuthal direction.

Thus, (4.6.6) becomes

$$\left(1 + \frac{\partial^2}{\partial\tilde{x}^2} + \epsilon\frac{4qe^{-\epsilon i\hat{\theta}}}{\rho}\frac{\partial^2}{\partial\tilde{x}\partial\hat{\theta}} + \epsilon^2\frac{4q^2e^{-2\epsilon i\hat{\theta}}}{\rho^2}\frac{\partial^2}{\partial\hat{\theta}^2} - i\epsilon^3\frac{4q^2e^{-2\epsilon i\hat{\theta}}}{\rho^2}\frac{\partial}{\partial\hat{\theta}}\right)^2 R_N - \epsilon^4\left(r_{M,1} + 3s_2U_0^2 - 5U_0^4\right)R_N \sim \frac{128\sqrt{2\pi}q^5}{\epsilon^4\sqrt{\rho}}\hat{\theta}e^{-\rho\hat{\theta}^2/2}e^{-2q|X_m|/\epsilon^2}e^{2qi\phi}\Lambda_q H_m\left(X_m - \frac{i\rho}{2q}\right)\left(e^{i\tilde{x}} + e^{-i\tilde{x}}\right). \tag{4.6.20}$$

Note the additional factor of $e^{2qi\phi}$, which appears due to the rescaling of $e^{2qi\tilde{x}}$ in terms of X, as detailed in (4.6.15). In this way the phase shift has an explicit presence in the calculation.

Although variations in $\hat{\theta}$ occur on a faster lengthscale than the original slow-scale X, they are still slower than the rapid oscillations in $\tilde{x}$, and so the problem remains one of multiple scales. This suggests the multiple-scales ansatz,

$$R_N \sim \frac{\sqrt{2\pi}}{\epsilon^6} e^{-2q|X_m|/\epsilon^2} e^{2qi\phi} \Lambda_q \left(R_{N,0} + \epsilon R_{N,1} + \epsilon^2 R_{N,2} + \cdots \right), \tag{4.6.21}$$

where each of the $R_{N,j}$ are functions of $\tilde{x}$ and $\hat{\theta}$. Note that R_N has been scaled to be a factor of ϵ^{-2} larger than the resonant forcing in (4.6.6). This ensures that all resonant terms in (4.6.6) sum to zero at each order, in accordance with the usual multiple-scales method.

After cancelling the common factor of $\epsilon^{-6} e^{-2q|X_m|/\epsilon^2}$ in (4.6.20), we find that the problem becomes simply one of multiple scales in algebraic orders. Taylor expanding the exponential terms in the differential operator and equating terms at $\mathrm{O}(1)$ gives

$$\left(1 + \frac{\partial^2}{\partial \tilde{x}^2}\right)^2 R_{N,0} = 0, \tag{4.6.22}$$

giving the leading-order solution

$$R_{N,0} = S_{0,1}(\hat{\theta}) e^{i\tilde{x}} + S_{0,-1}(\hat{\theta}) e^{-i\tilde{x}}. \tag{4.6.23}$$

Note that $R_{N,0}$ is not necessarily real on the real line; this fundamental property of the dependent variable U is recovered by adding the contribution from the conjugate singularity $-X_m$. At $\mathrm{O}(\epsilon)$ we have

$$\left(1 + \frac{\partial^2}{\partial \tilde{x}^2}\right)^2 R_{N,1} = 0, \tag{4.6.24}$$

with solution

$$R_{N,1} = S_{1,1}(\hat{\theta}) e^{i\tilde{x}} + S_{1,-1}(\hat{\theta}) e^{-i\tilde{x}}. \tag{4.6.25}$$

Finally, at $\mathrm{O}\left(\epsilon^2\right)$ we obtain

$$\left(1 + \frac{\partial^2}{\partial \tilde{x}^2}\right)^2 R_{N,2} - \frac{16q^2}{\rho^2} \frac{\partial^4 R_{N,0}}{\partial \tilde{x}^2 \partial \hat{\theta}^2} = \frac{128q^5}{\sqrt{\rho}} \hat{\theta} e^{-\rho\hat{\theta}^2/2} H_m\left(X_m - \frac{i\rho}{2q}\right) \left(e^{i\tilde{x}} + e^{-i\tilde{x}}\right). \tag{4.6.26}$$

Ensuring secular terms sum to zero provides the solvability condition

$$\frac{\mathrm{d}^2 S_{0,\pm 1}}{\mathrm{d}\hat{\theta}^2} = -8q^3\rho^{3/2} H_m\left(X_m - \frac{i\rho}{2q}\right)\hat{\theta}e^{-\rho\hat{\theta}^2/2}. \tag{4.6.27}$$

Hence we must have

$$S_{0,\pm 1}(\hat{\theta}) = (2q)^3\sqrt{\frac{\pi}{2}} H_m\left(X_m - \frac{i\rho}{2q}\right)\left[C_{\pm 1} + \operatorname{erf}\left(\hat{\theta}\sqrt{\rho/2}\right)\right]. \tag{4.6.28}$$

Here the $C_{\pm 1}$ are constants of integration, the other pair of which have been set to zero in order to ensure that the expansion remains uniform towards the edges of the Stokes layer, and $\operatorname{erf}(z)$ is the error function,

$$\operatorname{erf}(z) = \frac{2}{\sqrt{\pi}}\int_0^z e^{-v^2}\mathrm{d}v. \tag{4.6.29}$$

The contribution from the singularity X_m, $m \geq 0$, for a particular q is therefore

$$\begin{aligned} R_N \sim \frac{(2q)^3\pi}{\epsilon^6} e^{-2q|X_m|/\epsilon^2} e^{2qi\phi}\Lambda_q H_m\left(X_m - \frac{i\rho}{2q}\right)\Big[\left(C_1 + \operatorname{erf}\left(\hat{\theta}\sqrt{\rho/2}\right)\right)e^{i\tilde{x}} \\ + \left(C_{-1} + \operatorname{erf}\left(\hat{\theta}\sqrt{\rho/2}\right)\right)e^{-i\tilde{x}}\Big]. \end{aligned} \tag{4.6.30}$$

By symmetry, the contribution from the singularity in the lower half-plane $-X_m$ is simply the complex conjugate of (4.6.30), given by (recalling that Λ_q is real)

$$\begin{aligned} R_N \sim \frac{(2q)^3\pi}{\epsilon^6} e^{-2q|X_m|/\epsilon^2} e^{-2qi\phi}\Lambda_q H_m^*\left(-X_m + \frac{i\rho^*}{2q}\right)\Big[\left(C_1^* + \operatorname{erf}\left(\hat{\theta}^*\sqrt{\rho^*/2}\right)\right)e^{-i\tilde{x}} \\ + \left(C_{-1}^* + \operatorname{erf}\left(\hat{\theta}^*\sqrt{\rho^*/2}\right)\right)e^{i\tilde{x}}\Big]. \end{aligned} \tag{4.6.31}$$

where $\rho^* e^{i\pi/2 - i\epsilon\hat{\theta}^*} = 2q(X + X_m) = 2q(X - X_m^*)$. By matching (4.6.30) and (4.6.31) with the solution outside the Stokes layer, we can now show that it is a combination of $H_m(X)$ and its complex conjugate $H_m^*(X)$ that is switched on by crossing the Stokes line (from right to left).

4.6.2 Matching the inner and outer solutions

By considering the forcing terms in (4.6.20), we can now see that as $\hat{\theta} \to \pm\infty$, the right-hand side rapidly tends to zero. In other words, the forcing due to the singularities

is significant only in a region of width $\mathrm{O}(\epsilon)$ centred on the imaginary axis; the Stokes layer. Elsewhere along the real line, it can be taken to be zero, and the solution is given to leading order by (4.2.9), rewritten here as

$$R_N \sim \Big[D_1 A_f' + iD_2 A_f + D_3 H_m(X) + D_3^* H_m^*(X) + iD_4 G_m(X) + iD_4^* G_m^*(X) + \delta r P(X)\Big] e^{i\tilde{x}} + \text{c.c.}, \tag{4.6.32}$$

where $P(X)$ is given in (4.2.10). This must be matched to the inner expansion within the Stokes layer (4.6.30) and (4.6.31); we have redefined the arbitrary constants D_j in order to facilitate this. Comparing (4.6.32) with (4.6.30) and (4.6.31), we immediately see that we must have $C_1 = C_{-1} = C$, say, in order for the coefficient of H_m^* to be the complex conjugate of the coefficient of H_m both within and without the Stokes layer; we assume this henceforth.

Focusing on the fundamental harmonic $e^{i\tilde{x}}$, the inner expansion at the edges of the Stokes layer is, for a particular q and X_m,

$$R_N \to \frac{(2q)^3\pi}{\epsilon^6} e^{-2q|X_m|/\epsilon^2} \Lambda_q \left[e^{2qi\phi} H_m\left(X_m - \frac{i\rho}{2q}\right)(C \pm 1) + e^{-2qi\phi} H_m^*\left(-X_m + \frac{i\rho^*}{2q}\right)(C^* \pm 1)\right] e^{i\tilde{x}} + \text{c.c.} \tag{4.6.33}$$

as $\hat{\theta} \to \pm\infty$ and $\hat{\theta}^* \to \pm\infty$. Matching to the right of the Stokes layer requires that $R_N \to 0$ as $\hat{\theta} \to \infty$ and $\hat{\theta}^* \to \infty$, giving $C = -1$. Matching to the left is made simplest by first substituting $X = X_m - i\rho e^{i\epsilon\hat{\theta}}/2q$ in $H_m(X)$ and $X = -X_m + i\rho^* e^{-i\epsilon\hat{\theta}^*}/2q$ in $H_m^*(X)$ in (4.6.32). Focusing upon the pertinent part of (4.6.32), i.e. that which is switched on, and taking the limit $\hat{\theta} \to 0$, $\hat{\theta}^* \to 0$, this gives

$$R_N \sim \left[D_3 H_m\left(X_m - \frac{i\rho}{2q}\right) + D_3^* H_m^*\left(-X_m + \frac{i\rho^*}{2q}\right)\right] e^{i\tilde{x}} + \text{c.c.} \tag{4.6.34}$$

At the left-hand edge of the Stokes layer, the inner solution is given by

$$R_N \sim -\frac{2(2q)^3\pi}{\epsilon^6} e^{-2q|X_m|/\epsilon^2} \Lambda_q \left[e^{2qi\phi} H_m\left(X_m - \frac{i\rho}{2q}\right) + e^{-2qi\phi} H_m^*\left(-X_m + \frac{i\rho^*}{2q}\right)\right] e^{i\tilde{x}} + \text{c.c.} \tag{4.6.35}$$

Matching the two solutions therefore gives

$$D_3 = \begin{cases} -\dfrac{2(2q)^3\pi}{\epsilon^6} e^{-2q|X_m|/\epsilon^2} e^{2qi\phi} \Lambda_q, & X \leq 0, \\ 0 & X > 0. \end{cases} \tag{4.6.36}$$

Continuity is recovered by the adding the inner solution (4.6.30) and (4.6.31) to the outer solution (4.6.32), and subtracting matched parts. This results in the coefficient of $H_m(X)$ varying from zero to non-zero as the Stokes lines are crossed from right to left, giving the switching on of exponentially small terms via error function smoothing familiar to such beyond-all-orders analysis [7].

4.7 Existence of stationary fronts

We are now able to derive an existence condition for stationary fronts. We shall henceforth focus on the dominant contribution to the remainder, which is given by the singularities closest to the real line, X_0 and $X_{-1} = -X_0$, with $|q| = 1$, on the real line. Thus the dominant contribution to the remainder R_N to be switched on as the Stokes lines are crossed is

$$-\frac{16\pi}{\epsilon^6} e^{-2|X_0|/\epsilon^2} \Lambda_1 \left(e^{2i\phi} H_0(X) + e^{-2i\phi} H_0^*(X) \right) e^{i\tilde{x}} + \text{c.c.}, \tag{4.7.1}$$

existing to the left of the Stokes layer. Although the remainder (4.6.32) is exponentially small, $H_m(X)$ (see (4.5.9)) is exponentially growing as $X \to \pm\infty$. As the coefficient of H_m is zero to the right of the Stokes layer, unbounded terms are only present as $X \to -\infty$; note that the particular integral included in (4.6.32) is also exponentially growing as $X \to -\infty$, but bounded as $X \to \infty$. To ensure that the expansion remains uniform, the coefficient of the unbounded contributions must be set to zero. Because

$$H_m(X) \sim \left(\frac{10}{3}\right)^{1/4} \mu^{-5/2} e^{-\mu X}, \tag{4.7.2}$$

and the particular integral (4.2.10) is

$$P(X) \sim -\frac{\delta r}{8} \left(\frac{3}{10}\right)^{1/4} \mu^{-3/2} e^{-\mu X}, \tag{4.7.3}$$

as $X \to -\infty$, we have the exponentially growing contribution to R_N ,

$$-\left[\left(\frac{10}{3}\right)^{1/4}\frac{32\pi}{\epsilon^6\mu^{5/2}}e^{-2|X_0|/\epsilon^2}\Lambda_1\cos(2\phi)+\frac{\delta r}{8\mu^{3/2}}\left(\frac{3}{10}\right)^{1/4}\right]e^{-\mu X}e^{i\tilde{x}}+\text{c.c.}, \tag{4.7.4}$$

for large, negative X.

For the expansion to remain uniform, the exponentially small but exponentially growing term must vanish. Hence ϕ must satisfy

$$256\pi e^{-2|X_0|/\epsilon^2}\Lambda_1\cos(2\phi)+\left(\frac{3}{10}\right)^{1/2}\epsilon^6\mu\delta r=0. \tag{4.7.5}$$

This gives four values of ϕ in $[0,2\pi)$, two of which merely correspond to the reflection $u \to -u$, provided that the condition

$$|\delta r| \le \delta r_c := \left(\frac{10}{3}\right)^{1/2}\frac{256\pi}{\epsilon^6\mu}|\Lambda_1|e^{-2|X_0|/\epsilon^2} \tag{4.7.6}$$

is met. This, then, is the exponentially small parameter range within which the phase of the underlying spatial oscillations is fixed and stationary fronts exist. Moreover, (4.7.6) provides an analytical formula for the width of the snaking region close to bifurcation. We can rewrite this in terms of the unscaled parameters r and s to give

$$|r-r_M| \le \Delta r_c := \frac{10240\pi}{9s}|\Lambda_1|e^{-8\sqrt{30}\pi/9s}, \tag{4.7.7}$$

where $\Lambda_1 \approx 0.15$ (see Section 4.4) and r_M denotes the unscaled Maxwell point, given by rewriting (4.1.10) in terms of s:

$$r_M = -\frac{27}{160}s^2-\frac{1377}{81920000}s^4-\frac{106677}{10485760000000}s^6+\mathrm{O}\left(s^8\right). \tag{4.7.8}$$

Our formula should be compared to that derived by Susanto and Matthews using variational methods in [83], equation (16) in that paper, reproduced here in terms of the variables presently in use. They have

$$|r-r_M| \le \frac{14\sqrt{30}\pi}{3s}e^{-8\sqrt{30}\pi/9s}, \tag{4.7.9}$$

which is of the same form as (4.7.7), albeit approximately six times smaller. Nonetheless, the similarity between the two formulae is encouraging. We note that, because the

derivation of (4.7.9) is based only on leading order terms, the snaking width formula given here is the more accurate of the two.

4.8 Comparison with numerical computations

We shall now compare our analytical results with numerical computations. The latter have been achieved by solving the steady version of (4.0.1) in $x \in [-D/2, D/2]$ with periodic boundary conditions. This is a good approximation of the real line for large D, provided the patterned region of the localised solution under consideration is sufficiently far from the boundaries that they have negligible effect on the solution, i.e. $D \gg 2L/s^2$ (as $s = \mathrm{O}\left(\epsilon^2\right)$).

The numerical results presented here were obtained using a spectral collocation method to discretise the problem, and pseudo-arclength continuation to compute the bifurcation diagram. We note that second-order finite difference methods were found to be unable to determine the Maxwell point to sufficient accuracy for small s. Even with spectral methods, numerical continuation within the (exponentially small) snaking region can be particularly challenging due to the high density of solutions therein [15]. Such numerical difficulties can be somewhat mitigated by seeking a solution in the form of a cosine series rather than a full Fourier series, thus restricting our attention to solutions with even symmetry. Not only does the continuation process require only half as many gridpoints, but it is less prone to jumping from one branch to another, as the majority of the solution branches within the snaking region do not possess even symmetry. The second snaking branch, comprising odd localised patterns, can then be found using a sine series. Of course, no such short cut is available when calculating the rung solutions, as these are asymmetric, and one is forced to use a full Fourier series for such solution branches.

Our formula for the snaking width (4.7.7) is compared to numerical results in figure 4.2,

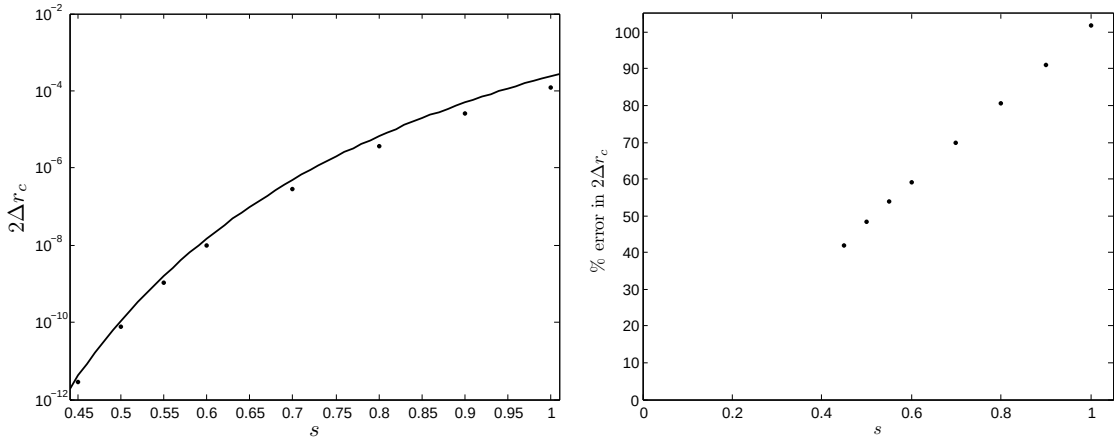

Figure 4.2: *Left: log plot of the analytically (solid line) and numerically (data points) determined snaking widths. Right: percentage error in the analytical formula for the snaking width (4.7.7). $s = 0.45$ is roughly the lowest value of s for which accurate results can be obtained in MATLAB without contamination due to machine error.*

for various values of s. The norm used is $||u||^2 = \sum_{j=0}^{N} u_j^2 D/N$, the discrete analogue of the L^2 norm, where $u(x)$ has been discretised into a sequence $u_j = u(-D/2 + jD/N)$, $j \in \{0, .., N\}$. Note that $u_0 = u_N$, as we have chosen to seek a solution in a D-periodic domain. Typically, we chose $D = 200\pi$ and $N = 1800$, giving eighteen grid points per wavelength. There is good agreement between the two, although the analytical formula for $2\Delta r_c$ overestimates the width of the snaking region. Nevertheless, we see in figure 4.2 that the error decreases linearly with s. Indeed, one of the strengths of the exponential asymptotics approach in general is its ability to shed light on behaviour taking place on scales too small to be numerically accessible. Furthermore, the percentage error in approximating the snaking width by $2\Delta r_c$ is proportional to $s = \mathrm{O}\left(\epsilon^2\right)$, as we would expect the first correction term to the remainder R_N to be (see Section 4.6).

We remark that Chapman and Kozyreff did not use a recurrence relation in the manner outlined in Section 4.4 in order to determine an estimate for their equivalent of $\lambda_{\pm 1}$ (which in the case of the quadratic-cubic SHE is complex as opposed to purely imaginary, thus giving two real constants to find) [22]. Instead, it was determined by a numerical fit of their analytical formula for the snaking width to a numerical com-

putation for a particular value of ϵ. Consequently, agreement between numerical and analytical results actually worsens as ϵ decreases below their selected value (see figure 5 of [22]). Due to our constructive derivation of $\lambda_{\pm 1}$ (and hence $\Lambda_{\pm 1}$), we observe increasing agreement between analytically and numerically derived snaking widths as ϵ decreases, as one would expect from an asymptotic analysis (see figure 4.2). Thus the present work provides a more satisfying application of their method.

CHAPTER 5

Matching distant fronts: localised patterns and multi-pulses

Now that we have derived the full asymptotic expansion of a stationary front solution to the Swift-Hohenberg equation (SHE) (3.0.1), including the exponentially small but exponentially growing terms in the remainder (4.7.4), we can construct fully localised spatial oscillations by superimposing two distant fronts back-to-back. This is done by matching the far-field expansion of an up-front with the far-field expansion of a down-front; the resultant matching conditions describe the snakes-and-ladders bifurcation diagram. This process can be extended to describe 'multi-pulse' solutions consisting of two or more patches of spatial oscillations [4, 15, 53] by matching the exponentially decaying tails of two localised patterns. In addition, a similar process allows investigation of the effects of boundary conditions on the snaking bifurcation diagram [55]. Following the calculation in Section 4.6.1, we note that each front used in the construction of a solution has an associated set of Stokes lines. Therefore each front switches on new exponentially growing terms as the Stokes lines are crossed; these are eliminated by carefully matching successive fronts.

5.1 Far-field expansions of fronts

To undergo the matching process, we need to know the behaviour of both a down-front and an up-front in the far-fields $X \to \pm\infty$. We shall focus first on a down-front, as given by the asymptotic expansion $U = U_0 + \cdots + R_N$ derived in Chapter 4; an up-front may be recovered simply by exploiting the spatial reversibility of the SHE (3.0.1) and performing the reflection $(x, X) \to (-x, -X)$ in the down-front. In the far-fields, the down-front is dominated by the sum of the leading-order front and the unbounded terms appearing in the remainder (4.7.4). In the relevant limits, the leading-order front A_f (4.1.7) is

$$A_f \sim \begin{cases} \left(\frac{3}{10}\right)^{1/4} \sqrt{\mu} \left(1 - \frac{1}{2} e^{\mu X}\right), & X \to -\infty, \\ \left(\frac{3}{10}\right)^{1/4} \sqrt{\mu} e^{-\mu X/2}, & X \to \infty; \end{cases} \tag{5.1.1}$$

the unbounded contribution (4.5.9) to the remainder which is switched as Stokes lines are crossed (see (4.6.30)-(4.6.33)) is

$$H_m \sim \begin{cases} \left(\frac{10}{3}\right)^{1/4} \mu^{-5/2} e^{-\mu X}, & X \to -\infty, \\ -2 \left(\frac{10}{3}\right)^{1/4} \mu^{-5/2} e^{\mu X/2}, & X \to \infty; \end{cases} \tag{5.1.2}$$

the particular integral (4.2.10) due to the deviation δr from the Maxwell point which appears in the remainder equation (4.2.4) is

$$P \sim \begin{cases} -\frac{1}{8} \left(\frac{3}{10}\right)^{1/4} \mu^{-3/2} e^{-\mu X}, & X \to -\infty, \\ \frac{1}{4} \left(\frac{3}{10}\right)^{1/4} \mu^{-1/2} X e^{-\mu X/2}, & X \to \infty. \end{cases} \tag{5.1.3}$$

Note that the particular integral P remains bounded as $X \to \infty$. Thus it is exponentially subdominant to the leading-order terms in the expansion in this limit and can be neglected. However, P is exponentially growing in the opposite far-field $X \to -\infty$, and so will need to be taken into account in the leading-order expansion in that limit.

Before we write down the full far-field expansion, we note that in order to construct localised patterns and multi-pulses we must match fronts which are separated by some distance in X. Hence we require the far-field expansions of translated fronts. We scale

the front separation to be $\mathrm{O}\left(1/\epsilon^2\right)$, motivated by the observation that the exponentially growing term in the remainder causes the asymptotic expansion to become non-uniform when $X = \mathrm{O}\left(1/\epsilon^2\right)$. Taking into account the error-function smoothing of the coefficient of H_m, as detailed in (4.6.30) and (4.6.31), the full leading-order far-field expansion of a down-front translated to the right by a distance l/ϵ^2, where l is an $\mathrm{O}(1)$ constant, is

$$U \sim \left\{ E_1 \left[1 - \frac{1}{2} e^{\mu\left(X - l/\epsilon^2\right)} \right] + \left[\frac{E_2}{\epsilon^6} e^{-2|X_0|/\epsilon^2} \left(K\cos(2\phi + \gamma) - 2\cos(2\phi) \right) \right.\right.$$
$$\left.\left. - E_3 \delta r \right] e^{-\mu\left(X - l/\epsilon^2\right)} \right\} e^{i(x + \phi - l/\epsilon^4)} + \text{c.c.} \tag{5.1.4}$$

for $X \ll l/\epsilon^2$, and

$$U \sim \left\{ E_1 e^{-\mu\left(X - l/\epsilon^2\right)/2} - \frac{2E_2}{\epsilon^6} e^{-2|X_0|/\epsilon^2} K\cos(2\phi + \gamma) e^{\mu\left(X - l/\epsilon^2\right)/2} \right\} e^{i(x + \phi - l/\epsilon^4)} + \text{c.c.} \tag{5.1.5}$$

for $X \gg l/\epsilon^2$, where we define

$$\begin{aligned} E_1 &= \left(\frac{3}{10}\right)^{1/4} \sqrt{\mu}, \\ E_2 &= \left(\frac{10}{3}\right)^{1/4} \frac{16\pi\Lambda_1}{\mu^{5/2}}, \\ E_3 &= \frac{1}{8\mu^{3/2}} \left(\frac{3}{10}\right)^{1/4}. \end{aligned} \tag{5.1.6}$$

Note the constant $Ke^{i\gamma}$; this arises from matching the inner solution (4.6.30) and (4.6.31) within the Stokes layer to the outer solution (4.6.32), and setting $C = -1 + Ke^{i\gamma}$. In Section 4.6.2, we set K to zero, as in that case we required H_m to have coefficient zero to the left of the Stokes layer. In the present chapter, however, we need to match exponentially decaying tails of fronts in order to construct multi-pulses and investigate boundary conditions. Therefore we shall require H_m to have non-zero coefficient to the left of the relevant Stokes layer in order that the tails contain both exponentially growing and decaying terms, and so shall not fix $Ke^{i\gamma}$ for the moment but instead evaluate it as needed in the calculations to come.

From (5.1.4) and (5.1.5) we can write down the far-field behaviour of an up-front by performing the reflection $(x - l/\epsilon^4, X - l/\epsilon^2) \to (-x + l/\epsilon^4, -X + l/\epsilon^2)$; in order to retain the focus on the fundamental harmonic e^{ix}, we then take the complex conjugate. Thus we obtain

$$U \sim \left\{ E_1 \left[1 - \frac{1}{2} e^{-\mu\left(X - l/\epsilon^2\right)} \right] + \left[\frac{E_2}{\epsilon^6} e^{-2|X_0|/\epsilon^2} \left(\hat{K} \cos(2\hat{\phi} + \hat{\gamma}) - 2\cos(2\hat{\phi}) \right) \right.\right.$$
$$\left.\left. - E_3 \delta r \right] e^{\mu\left(X - l/\epsilon^2\right)} \right\} e^{i(x - \hat{\phi} - l/\epsilon^4)} + \text{c.c.} \tag{5.1.7}$$

for $X \gg l/\epsilon^2$, and

$$U \sim \left\{ E_1 e^{\mu\left(X - l/\epsilon^2\right)/2} - \frac{2E_2}{\epsilon^6} e^{-2|X_0|/\epsilon^2} \hat{K} \cos(2\hat{\phi} + \hat{\gamma}) e^{-\mu\left(X - l/\epsilon^2\right)/2} \right\} e^{i(x - \hat{\phi} - l/\epsilon^4)} + \text{c.c.} \tag{5.1.8}$$

for $X \ll l/\epsilon^2$. The phase-shift and constant of integration are denoted by hatted symbols in the up-front in order to allow us to take into account all possible solutions when matching fronts. As the focus is on the fundamental harmonic e^{ix} and we have performed the reflection $(x - l/\epsilon^2) \to -x + l/\epsilon^2$ in (5.1.4) and (5.1.5), the phase-shift appears as $-\hat{\phi}$ rather than $+\hat{\phi}$. Note that the up-front and down-front have the same origin, namely $X = l/\epsilon^2$.

As an aside, we note that, whereas Chapman and Kozyreff were forced to include a super-slow scale $\xi = \epsilon^4 x$ in order to carry out this step [22], there is no need to do so here. In the quadratic-cubic case considered in [22], the $\mathrm{O}\left(\epsilon^2\right)$ contribution to the expansion contains a term of the form Xe^X as $X \to -\infty$. This decaying exponential has a coefficient of $\mathrm{O}(1)$ when $X = \mathrm{O}\left(1/\epsilon^2\right)$, and so must be included in the matching process. The super-slow scale ξ, which manifests as a slow phase adjustment $\phi = \Phi\xi + \psi$ for some constants Φ and ψ, is necessary in order to derive the $\mathrm{O}\left(\epsilon^2\right)$ term in the expansion, as it forces an unbounded particular integral to vanish. On the other hand, in the present case of the cubic-quintic SHE, the equivalent super-slow scale turns out to be $\xi = \epsilon^8 x$. As we match fronts when $X - l/\epsilon^2 = \mathrm{O}\left(1/\epsilon^2\right)$, i.e. when the exponentially growing terms in the remainder (4.7.4) cancel out their exponentially

small coefficients, the super-slow scale does not affect the matching process and is of no consequence to the present calculation.

5.2 Constructing localised patterns

We can now match together a down-front and an up-front to form a localised pattern. We first note that, as we require $U \to 0$ as $X \to \pm\infty$, H_m must have coefficient zero outside the localised patch. Hence we must have $K = 0$ in order to eliminate growing terms in the tails of of the fronts, as in Section 4.6.2. We shall choose the origin of the down-front to be at $X = L/\epsilon^2$, and the up-front to be at $X = -L/\epsilon^2$, thus producing a localised patch of width $2L/\epsilon^2$, centred on $X = 0$. Thus we match the constant amplitude, exponentially growing and exponentially decaying terms in the down-front for $X \ll L/\epsilon^2$, given by (5.1.4) with $l = L$, with the equivalent terms in the up-front for $X \gg -L/\epsilon^2$, given by (5.1.7) with $l = -L$.

Equating constant amplitude terms gives

$$e^{i\phi - iL/\epsilon^4} = e^{-i\hat{\phi} + iL/\epsilon^4}; \tag{5.2.1}$$

hence

$$\hat{\phi} = \left(\frac{2L}{\epsilon^4} - \phi\right) \mod 2\pi. \tag{5.2.2}$$

Equating coefficients of $e^{-\mu X}$ gives

$$\frac{E_1}{2} e^{-2\mu L/\epsilon^2} = \frac{2E_2}{\epsilon^6} e^{-2|X_0|/\epsilon^2} \cos(2\phi) + E_3 \delta r, \tag{5.2.3}$$

while equating coefficients of $e^{\mu X}$ requires

$$\frac{E_1}{2} e^{-2\mu L/\epsilon^2} = \frac{2E_2}{\epsilon^6} e^{-2|X_0|/\epsilon^2} \cos(2\hat{\phi}) + E_3 \delta r. \tag{5.2.4}$$

In consequence, either

$$\hat{\phi} = \phi \mod \pi, \tag{5.2.5}$$

or

$$\hat{\phi} = -\phi \mod \pi. \tag{5.2.6}$$

Thus there are four possible relations between the two phases, modulo 2π, each of which must be considered in order to draw the bifurcation diagram.

Case 1. $\hat{\phi} \equiv \phi \mod 2\pi$

In this instance $\phi \equiv L/\epsilon^4 \mod \pi$, and the front separation $2L/\epsilon^2$ is defined implicitly by

$$\delta r = -\left(\frac{10}{3}\right)^{1/2} \frac{256\pi}{\epsilon^6 \mu} e^{-2|X_0|/\epsilon^2} \Lambda_1 \cos\left(\frac{2L}{\epsilon^4}\right) + 4\mu^2 e^{-2\mu L/\epsilon^2}, \tag{5.2.7}$$

where we now write out the constants E_j in full.

Case 2. $\hat{\phi} \equiv \phi + \pi \mod 2\pi$

Now $\phi \equiv L/\epsilon^4 + \frac{\pi}{2} \mod \pi$ and L is given by

$$\delta r = -\left(\frac{10}{3}\right)^{1/2} \frac{256\pi}{\epsilon^6 \mu} e^{-2|X_0|/\epsilon^2} \Lambda_1 \cos\left(\frac{2L}{\epsilon^4} + \pi\right) + 4\mu^2 e^{-2\mu L/\epsilon^2}. \tag{5.2.8}$$

Case 3. $\hat{\phi} \equiv -\phi \mod 2\pi$

This gives $2L = 2p\pi\epsilon^4$ for $p \in \mathbb{N}$. The phase-shift is obtained by solving

$$\delta r = -\left(\frac{10}{3}\right)^{1/2} \frac{256\pi}{\epsilon^6 \mu} e^{-2|X_0|/\epsilon^2} \Lambda_1 \cos(2\phi) + 4\mu^2 e^{-2\mu L/\epsilon^2}. \tag{5.2.9}$$

Case 4. $\hat{\phi} \equiv -\phi + \pi \mod 2\pi$

Here $2L = (2p+1)\pi\epsilon^4$ for $p \in \mathbb{N}$, with the phase-shift again determined by (5.2.9).

The bifurcation equations are therefore a result of two exponentially small effects, the pinning of the envelope to the underlying pattern at a particular value of δr and the interaction between the up-front and the down-front. Cases 1 and 2, in which the phase-shifts of the two fronts are equal modulo π, describe the two snaking solutions, each with a different symmetry. Case 1 preserves the symmetry $x \to -x$, whilst Case 2 preserves the symmetry $(u, x) \to (-u, -x)$. The snaking structure itself is a consequence

of the cosine terms in (5.2.7) and (5.2.8). An increase of the front separation, $2L/\epsilon^4$, by 2π, causes the snake to go through a complete loop, thus adding two more spatial oscillations to the pattern as it does so. The terms which are exponentially small in L tend to zero extremely rapidly as the front separation increases. When these are negligible, the solution curves enter the snaking region, the width of which is therefore defined by

$$|\delta r| \leq \delta r_c = \left(\frac{10}{3}\right)^{1/2} \frac{256\pi}{\epsilon^6 \mu} |\Lambda_1| e^{-2|X_0|/\epsilon^2}. \tag{5.2.10}$$

This is precisely the condition for the existence of stationary fronts, (4.7.6), derived earlier. Hence the exponential terms in L show how the snaking curves skew to the right for moderate values of L.

Cases 3 and 4 describe the ladders. The patterns here are asymmetric, with a front separation independent of δr. Although the width of the localised region is fixed, the phase of the pattern shifts inside its envelope as ϕ varies with δr along the solution branch, thus providing the ladders linking the two snaking curves. Note that L must be at least $\mathrm{O}(1)$, and therefore p must be at least $\mathrm{O}\left(1/\epsilon^4\right)$ in these cases. The ladders exist in the same region of parameter space as the snakes, with the exponential term in L (5.2.9) again rapidly tending to zero as L increases.

In each of the four cases, the phase ϕ is determined uniquely modulo π. While adding an even multiple of π to the phase leaves the solution unchanged, adding an odd integer multiple of π to the phase corresponds to the symmetry $u \to -u$, a feature of the cubic-quintic Swift-Hohenberg equation (4.0.1). Thus each snake and each ladder in fact represent two patterns, related by the symmetry $u \to -u$.

These results complement well those of Beck *et al.* [4], in which the existence of fronts (heteroclinic orbits in x) in a general, reversible fourth-order system, of which (4.0.1) is a special case, was shown to give rise to snakes-and-ladders bifurcations of localised states (homoclinic orbits in x) through the 'gluing together' of matched fronts. We also remark that the values derived here for the phase-shifts in the snaking solutions (Cases

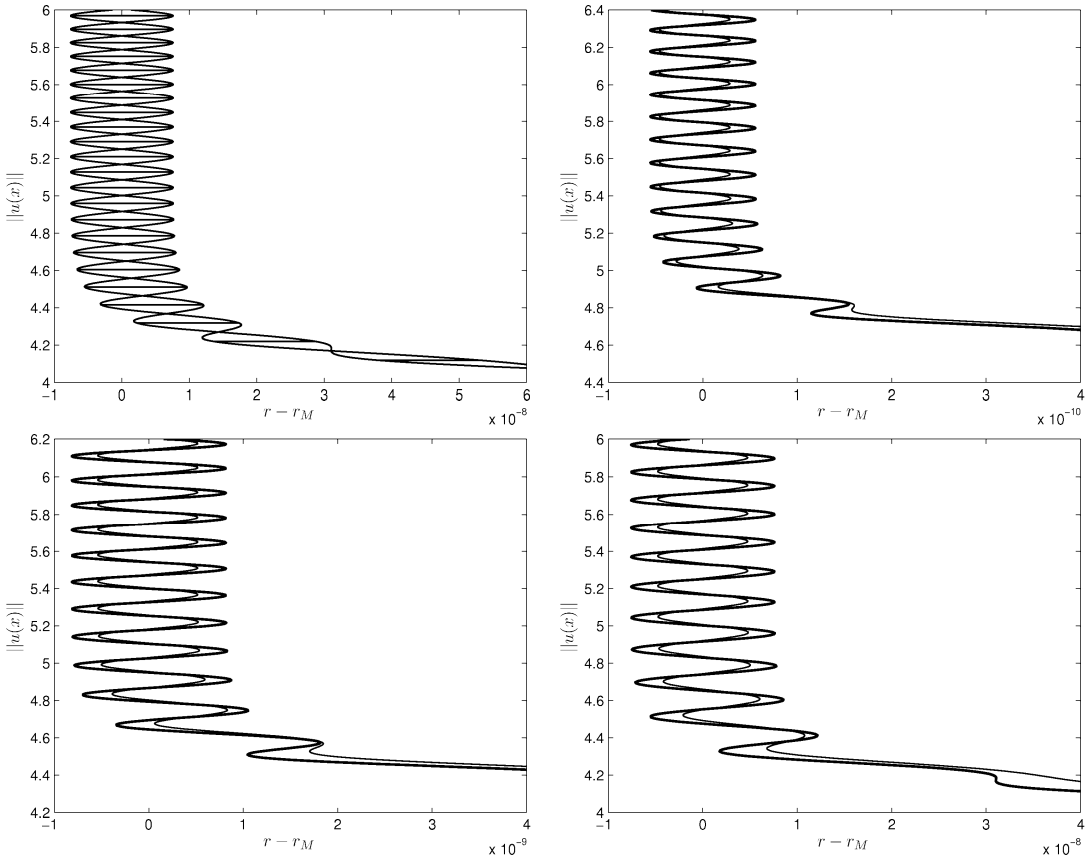

Figure 5.1: *The top left panel contains the analytical snakes-and-ladders bifurcation diagram of the cubic-quintic SHE (3.0.1) for $s = 0.6$. The other three panels present comparisons between the analytical formula (5.2.7) for the even snaking branch (thick line) and numerical calculations (thin line) in a domain of width $D = 200\pi$, with $s = 0.5$ (top right), $s = 0.55$ (bottom left) and $s = 0.6$ (bottom right). The unscaled Maxwell point r_M is given by (4.7.8).*

1 and 2) and the front separations in the ladder solutions (Cases 3 and 4) agree with those found by Susanto and Matthews [83] using a variational approach.

The full analytical snakes-and-ladders bifurcation diagram can be seen in figure 5.1, along with a comparison of the analytically derived even snaking curve with numerically derived examples for various values of $s = \epsilon^2 s_2$, with good agreement. Numerical computations were carried out using spectral collocation methods and pseudo-arclength continuation, in the same manner as in Section 4.8.

5.3 Constructing multi-pulse solutions

We shall now extend the matching process of Section 5.2 to construct multi-pulse solutions. These comprise two or more localised patches of spatial oscillations, or 'pulses', embedded within the trivial state. In an infinite domain, such solutions do not snake; instead, they form isolas within the snaking region [4, 15, 53], as shown in figure 5.2 for solutions with even symmetry. In contrast, in a periodic domain certain multi-pulses with even symmetry do snake. For example, a Γ-periodic solution containing m pulses whose centres are a distance Γ/m apart is equivalent to a (Γ/m)-periodic solution containing one pulse; there are also certain asymmetric solutions which snake in a finite domain [15]. However, we shall only consider infinite domains and so will not observe snaking of multi-pulses. Each pulse inherits its form from the part of the snake it is closest to; for example, in figure 5.2 we see that the individual pulses on the stable 'snaking part' of the isola are almost rotationally symmetric about their centres, those on the 'rung-like part' are asymmetric, and those on the unstable 'snaking part' are almost reflectionally symmetric. Note each two-pulse in that figure has reflection symmetry; the picture is similar for rotationally symmetric and asymmetric solutions.

For the sake of simplicity, we shall focus on two-pulse solutions, which we construct by superimposing two localised patterns of width $\mathrm{O}\left(1/\epsilon^2\right)$, separated by a distance which is also $\mathrm{O}\left(1/\epsilon^2\right)$. The resultant matching conditions are similar to those derived in Section 5.2; however, the exponentially decaying tail of the down-front in the left-hand pulse must be matched with the exponentially decaying tail of the up-front in the right-hand pulse.

We define the front translations so that the pulses are separated by a distance of $2L_s/\epsilon^2$, the left-hand pulse has width $2L_1/\epsilon^2$ and the right-hand pulse has width $2L_2/\epsilon^2$, for some $L_s, L_1, L_2 = \mathrm{O}(1)$. Thus the left-hand pulse is centred at $X = -(L_s + L_1)/\epsilon^2$, while the right-hand pulse is centred at $X = (L_s + L_2)/\epsilon^2$, and the gap between the

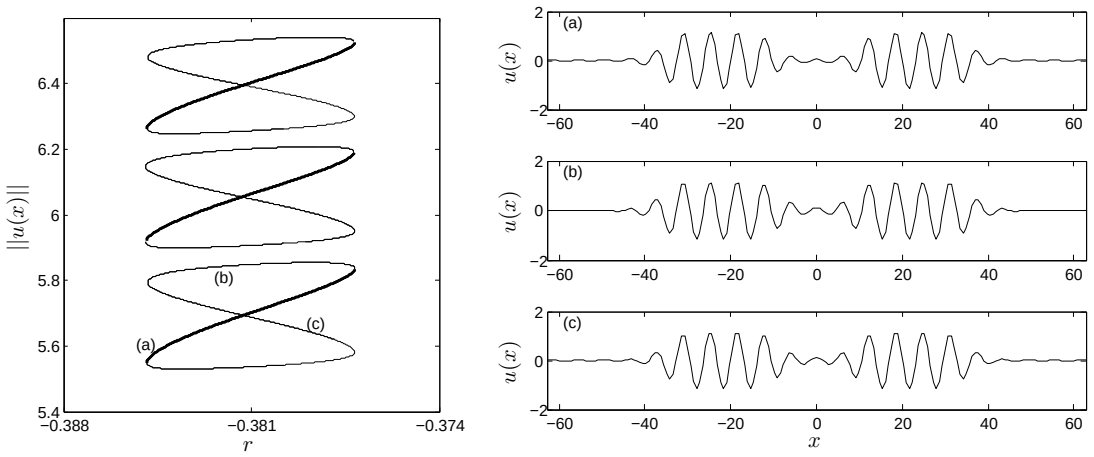

Figure 5.2: *Left: isolas of symmetric two-pulse solution to (3.0.1) with $s = 1.5$ on a periodic domain of length 40π. Stable (unstable) solutions are indicated by a thick (thin) line. Right: example two-pulses. Labels correspond to the positions indicated in the left-hand panel.*

fronts is centred at the origin. We set $\phi = \phi_1$ and $Ke^{i\gamma} = K_1 e^{i\gamma_1}$ in the down-front of the left-hand pulse and $\phi = \phi_2$ and $Ke^{i\gamma} = K_2 e^{i\gamma_2}$ in the down-front of the right-hand pulse, and assign subscripts to the hatted parameters associated with the up-fronts in the obvious manner.

We first ensure $U \to 0$ as $X \to \pm\infty$ by setting $\hat{K}_1 = K_2 = 0$, thus eliminating growing terms as $X \to \pm\infty$ in the same manner as in Section 4.6.2. Secondly, we match the two pulses together by equating exponentially growing and decaying terms in (5.1.5) with $(l, \phi, Ke^{i\gamma}) = (-L_s, \phi_1, K_1 e^{i\gamma_1})$ to the corresponding terms in (5.1.8) with $(l, \hat{\phi}, \hat{K}e^{i\hat{\gamma}}) = (L_s, \hat{\phi}_2, \hat{K}_2 e^{i\hat{\gamma}_2})$. Thus we obtain

$$E_1 e^{-\mu L_s/\epsilon^2} e^{-i(\phi_1 + \hat{\phi}_2 + 2L_s/\epsilon^4)} = -\frac{2E_2}{\epsilon^6} e^{-2|X_0|/\epsilon^2} K_1 \cos(2\phi_1 + \gamma_1), \tag{5.3.1}$$

$$E_1 e^{-\mu L_s/\epsilon^2} e^{i(\phi_1 + \hat{\phi}_2 + 2L_s/\epsilon^4)} = -\frac{2E_2}{\epsilon^6} e^{-2|X_0|/\epsilon^2} \hat{K}_2 \cos(2\hat{\phi}_2 + \hat{\gamma}_2). \tag{5.3.2}$$

As both right-hand sides are real, we must therefore have

$$\hat{\phi}_2 = \left(-\frac{2L_s}{\epsilon^4} - \phi_1 + p\pi \right) \bmod 2\pi, \tag{5.3.3}$$

for $p = 0, 1$.

Now we match the two fronts of the left-hand pulse together, in a similar manner as in Section 5.2. Equating terms of constant amplitude in (5.1.4) with $(l, \phi, Ke^{i\gamma}) = (-L_s, \phi_1, K_1 e^{i\gamma_1})$ and (5.1.7) with $(l, \hat{\phi}, \hat{K}e^{i\hat{\gamma}}) = (-L_s - 2L_1, \hat{\phi}_1, \hat{K}_1 e^{i\hat{\gamma}_1})$ gives

$$\hat{\phi}_1 = \left(\frac{2L_1}{\epsilon^4} - \phi_1 \right) \mod 2\pi. \tag{5.3.4}$$

Then, matching exponential terms and employing (5.3.1) yields

$$-\frac{E_1}{2} e^{-2\mu L_1/\epsilon^2} = -(-1)^p \frac{E_1}{2} e^{-\mu L_s/\epsilon^2} - \frac{2E_2}{\epsilon^6} e^{-2|X_0|/\epsilon^2} \cos(2\phi_1) - E_3 \delta r, \tag{5.3.5}$$

$$-\frac{E_1}{2} e^{-2\mu L_1/\epsilon^2} = -\frac{2E_2}{\epsilon^6} e^{-2|X_0|/\epsilon^2} \cos(2\hat{\phi}_1) - E_3 \delta r. \tag{5.3.6}$$

Similarly, we construct the right-hand pulse by matching (5.1.4) with $(l, \phi, Ke^{i\gamma}) = (L_s + 2L_2, \phi_2, K_2 e^{i\gamma_2})$ to (5.1.7) with $(l, \hat{\phi}, \hat{K}e^{i\hat{\gamma}}) = (L_s, \hat{\phi}_2, \hat{K}_2 e^{i\hat{\gamma}_2})$. Matching constant amplitude terms gives

$$\phi_2 = \left(\frac{2L_2}{\epsilon^4} - \hat{\phi}_2 \right) \mod 2\pi, \tag{5.3.7}$$

while matching exponential terms and substituting (5.3.2) provides

$$-\frac{E_1}{2} e^{-2\mu L_2/\epsilon^2} = -\frac{2E_2}{\epsilon^6} e^{-2|X_0|/\epsilon^2} \cos(2\phi_2) - E_3 \delta r, \tag{5.3.8}$$

$$-\frac{E_1}{2} e^{-2\mu L_2/\epsilon^2} = -(-1)^p \frac{E_1}{2} e^{-\mu L_s/\epsilon^2} - \frac{2E_2}{\epsilon^6} e^{-2|X_0|/\epsilon^2} \cos(2\hat{\phi}_2) - E_3 \delta r. \tag{5.3.9}$$

Substitution of (5.3.3) into (5.3.7) yields

$$\phi_2 = \left(\frac{2L_s}{\epsilon^4} + \frac{2L_2}{\epsilon^4} + \phi_1 + p\pi \right) \mod 2\pi. \tag{5.3.10}$$

Thus (5.3.4), (5.3.10) and (5.3.3) respectively define the phases $\hat{\phi}_1$, ϕ_2 and $\hat{\phi}_2$ in terms of the primary phase ϕ_1, and we are left with the system of four equations (5.3.5), (5.3.6), (5.3.8) and (5.3.9) in the four unknowns ϕ_1, L_s, L_1 and L_2.

Now, subtracting (5.3.5) from (5.3.6) and substituting (5.3.4) gives

$$0 = (-1)^p \frac{E_1}{2} e^{-\mu L_s/\epsilon^2} + \frac{2E_2}{\epsilon^6} e^{-2|X_0|/\epsilon^2} \left[\cos(2\phi_1) - \cos\left(2\phi_1 - \frac{4L_1}{\epsilon^4} \right) \right], \tag{5.3.11}$$

which can be solved for L_1 to give

$$\frac{L_1}{\epsilon^4} = \frac{\phi_1}{2} \pm \frac{1}{4} \arccos\left[(-1)^p \frac{\epsilon^6 E_1}{4E_2} e^{2|X_0|/\epsilon^2} e^{-\mu L_s/\epsilon^2} + \cos(2\phi_1) \right] + \frac{k_1 \pi}{2}, \tag{5.3.12}$$

for some sufficiently large, positive integer k_1. Similarly, subtracting (5.3.9) from (5.3.8) and substituting (5.3.3) and (5.3.10) gives

$$0 = (-1)^p \frac{E_1}{2} e^{-\mu L_s/\epsilon^2} + \frac{2E_2}{\epsilon^6} e^{-2|X_0|/\epsilon^2} \left[\cos\left(2\phi_1 + \frac{4L_s}{\epsilon^4}\right) - \cos\left(2\phi_1 + \frac{4L_s}{\epsilon^4} + \frac{4L_2}{\epsilon^4}\right) \right], \tag{5.3.13}$$

which can be solved for L_2 to give

$$\frac{L_2}{\epsilon^4} = -\frac{\phi_1}{2} - \frac{L_s}{\epsilon^4} \pm \frac{1}{4} \arccos\left[(-1)^p \frac{\epsilon^6 E_1}{4E_2} e^{2|X_0|/\epsilon^2} e^{-\mu L_s/\epsilon^2} + \cos\left(2\phi_1 + \frac{4L_s}{\epsilon^4}\right) \right] + \frac{k_2 \pi}{2}, \tag{5.3.14}$$

for some sufficiently large, positive integer k_2. Note that the first term inside the inverse cosines in (5.3.12) and (5.3.14) is exponentially small provided $(2|X_0| - \mu L_s)$ is $\mathrm{O}(1)$ and negative, i.e. for sufficiently large pulse separation L_s.

(5.3.12) and (5.3.14) thus provide L_1 and L_2 in terms of L_s and ϕ_1. As (5.3.12) and (5.3.14) are both discontinuous functions of ϕ_1, we can begin to see how the snakes-and-ladders bifurcation diagram breaks up into isolas. Unfortunately, the complexity of (5.3.8) and (5.3.9) prevents a complete analytical description of the bifurcation diagram. However, the problem simplifies greatly if we assume that the two-pulse is symmetric, allowing further progress.

5.3.1 Symmetric two-pulses

As the cubic-quintic SHE (3.0.1) is invariant under reflections $(u, x) \to (u, -x)$ and rotations $(u, x) \to (-u, -x)$, symmetric two-pulses come in both even and odd forms. Clearly, a symmetric solution requires that $L_1 = L_2 = L$, say, $\phi_2 = \hat{\phi}_1 + p\pi$ and $\hat{\phi}_2 = \phi_1 + p\pi$, where $p = 0$ corresponds to even solutions and $p = 1$ to odd solutions. Thus (5.3.3) gives

$$\phi_1 = -\frac{L_s}{\epsilon^4} \mod \pi. \tag{5.3.15}$$

Note that (5.3.8)-(5.3.9) are now equivalent to (5.3.5)-(5.3.6). Therefore substitution into (5.3.12) gives

$$\frac{L}{\epsilon^4} = -\frac{L_s}{2\epsilon^4} \pm \frac{1}{4}\arccos\left[(-1)^p\left(\frac{3}{10}\right)^{1/2}\frac{\epsilon^6\mu^3}{64\pi\Lambda_1}e^{2|X_0|/\epsilon^2}e^{-\mu L_s/\epsilon^2} + \cos\left(\frac{2L_s}{\epsilon^4}\right)\right] + \frac{k\pi}{2} \tag{5.3.16}$$

for some sufficiently large integer k, and (5.3.5) then provides the bifurcation equation

$$\delta r = -\left(\frac{10}{3}\right)^{1/2}\frac{256\pi}{\epsilon^6\mu}e^{-2|X_0|/\epsilon^2}\Lambda_1\cos\left(\frac{2L_s}{\epsilon^4}\right) + 4\mu^2\left(e^{-2\mu L/\epsilon^2} - (-1)^p e^{-\mu L_s/\epsilon^2}\right), \tag{5.3.17}$$

where we have written out the constants E_j in full.

We can therefore parameterise the bifurcation diagram by L_s. The pulse width is given by (5.3.16), which is discontinuous for L_s/ϵ^4 within a small band of values near $m\pi$, for some large positive integer m. Furthermore, because the first term inside the arccosine is exponentially small for large enough L_s, the positive branch of L is approximately constant for L_s/ϵ^4 between $m\pi$ and $m\pi + \frac{\pi}{2}$, and decreases approximately linearly with L_s for L_s/ϵ^4 between $m\pi + \frac{\pi}{2}$ and $(m+1)\pi$, and *vice versa* for the negative branch, where m is some large, positive integer. Thus each branch of (5.3.16) encodes one 'snake-like' and one 'rung-like' segment of the isola. The two branches coincide when the argument of the arccosine is equal to one, forming a figure-of-eight. The bifurcation parameter δr is then given by (5.3.17); as (5.3.16) is discontinuous in L_s, so is (5.3.17). Varying the integer k in (5.3.16) provides the expected infinite multiplicity of symmetric solutions. As the value of L_s barely changes the norm of the solution, the bifurcation diagram occurs in stacks of nested isolas, with varying L_s produce the 'nest' and varying L producing the 'stack' (to use the terminology of [15]). Isolas of even two-pulses are plotted using (5.3.16)-(5.3.17) in figure 5.3; results are similar for odd two-pulses. Note how the isolas become skewed to the right of the snaking region as the pulse width decreases, in the same way as was observed for one-pulses, due to the exponentially small term in L in (5.3.17). Numerical computations for large domains are rather difficult, as the isolas become exponentially close together (as seen

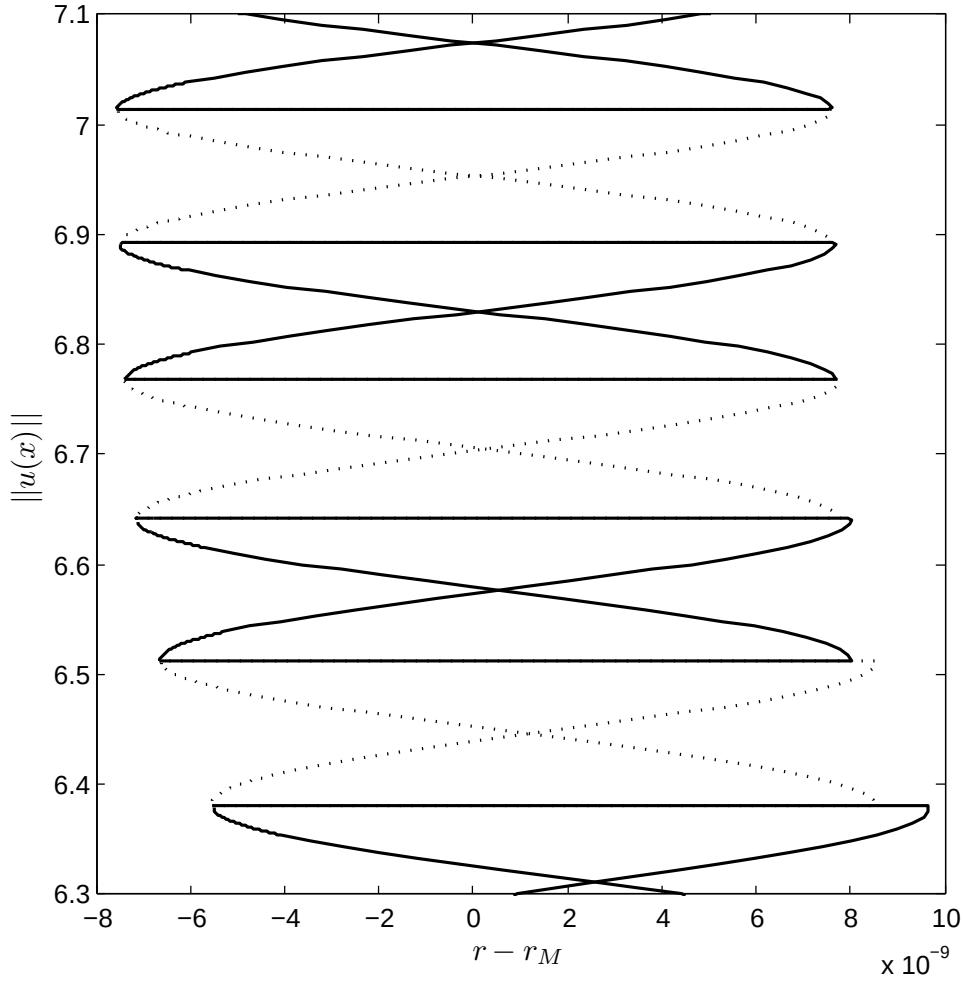

Figure 5.3: *Isolas of two-pulses with even symmetry in the SHE (3.0.1) with $s = 0.6$, drawn using the analytical formulae (5.3.16)-(5.3.17). Isolas are drawn alternating between solid and dotted lines for the purpose of clarity only; stability is not indicated.*

in figure 5.3), which makes the likelihood of skipping between branches very high. For this reason, we do not present a quantitative comparison of our results with numerical computations. However, qualitative agreement with figure 5.2 and [15], combined with the numerical verification of our results for one-pulses carried out in Section 5.2, provides good reason to be confident in the present result.

CHAPTER 6

One-dimensional homoclinic snaking on a planar lattice

Homoclinic snaking is not only a phenomenon of continuous systems; remarkably similar bifurcation structures also appear in discrete systems [85]. A pertinent physical example which has received much recent attention is nonlinear optics [26, 99, 100], not least due to the potential use of 'cavity solitons' as a basis for purely optical information storage and processing [73]. The main difference between discrete and continuous snaking is the form of the pinning mechanism. Rather than consisting of fronts pinned to underlying spatial oscillations, the lattice itself provides the requisite structure to which fronts may pin. Therefore spatial oscillations are unnecessary for pinning to take place and the simplest discrete system to exhibit snaking behaviour is second-order. This is in contrast to snaking in a continuum, in which a fourth-order system such as the SHE is required. Furthermore, numerical computations are much simpler in discrete problems than in continuous ones, as there is no need to discretise the problem. Thus discrete contexts provide a promising means of studying more complicated snaking phenomena in greater detail than has heretofore been achieved, in particular snaking in higher dimensions [26, 85]. In this chapter we perform an initial step in this direction by considering snaking of one-dimensional fronts of arbitrary orientation on

a two-dimensional square lattice, using the method of exponential asymptotics. We shall show that the width of the snaking region is a discontinuous function of the angle of orientation of the solution with respect to the lattice; in particular, that the snaking region vanishes when the tangent of the angle is irrational.

We remark that an exponential asymptotic analysis of discrete fronts has been carried out in [50] using a different method than that employed here, following [97, 98]. However, discrete effects in that work were modelled by allowing the coefficient of a nonlinear term to vary periodically in space, rather than through a difference operator as is the case here, and so differs from the present work. We expect our method to be equally applicable to both methods of modelling discreteness. An incomplete analysis [27] of snaking phenomena has also been performed in an non-autonomous system similar to that in [50]; this fails to fully describe the snakes-and-ladders bifurcation because it does not consider exponentially small effects.

A typical differential-difference equation on the plane is

$$\frac{\partial u}{\partial t} = \Delta u - F(u;r), \tag{6.0.1}$$

where $u \equiv u(x,y,t)$ for $(x,y,t) \in \mathbb{Z}^2 \times [0,\infty)$. Here $F(u;r)$ is some nonlinear function of u incorporating a bifurcation parameter r, which we assume to be bistable, and the difference operator Δu comprises the nearest-neighbour stencil

$$\Delta u(x,y,t) := u(x+1,y,t) + u(x-1,y,t) + u(x,y+1,t) + u(x,y-1,t) - 4u(x,y,t). \tag{6.0.2}$$

Although we have specified Δu, the methods presented here should be applicable to a reasonably general class of difference operators. Two different snaking scenarios for (6.0.1) with $u \equiv u(x)$ are shown in figures 6.1 and 6.3, with corresponding example solutions in figures 6.2 and 6.4. As already mentioned, we can see that the snakes-and-ladders structure is much the same as in the continuous case (see figure 1.1), although the symmetries preserved by the two snakes are different. Both snaking curves rep-

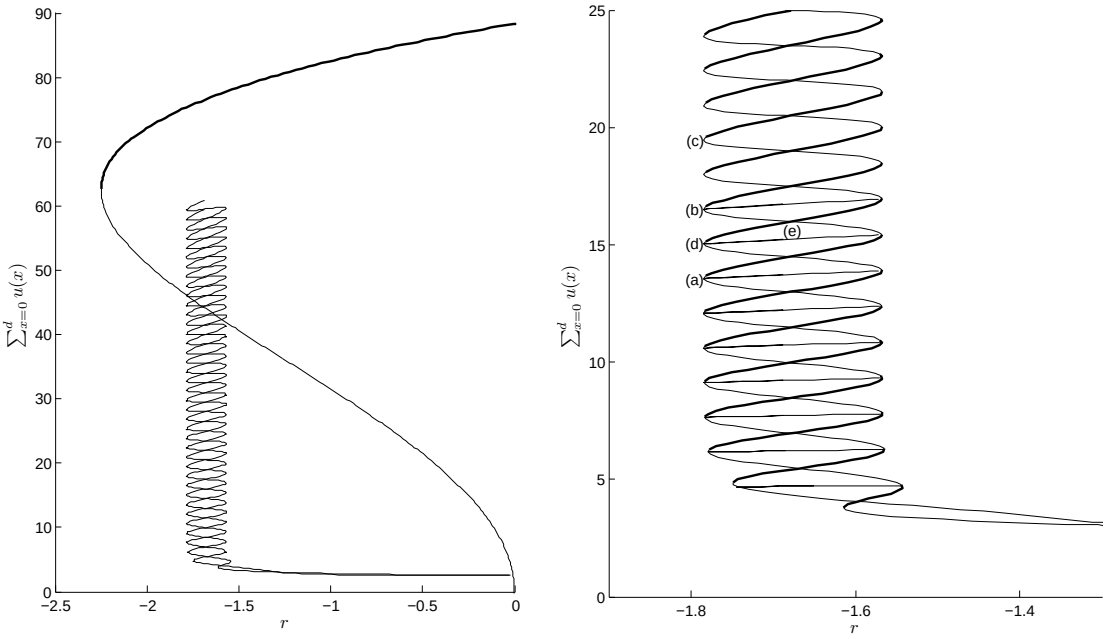

Figure 6.1: *Pitchfork-saddle snaking bifurcation diagram produced by solving (6.0.1) with* $u \equiv u(x)$ *and* $F(u;r) = -ru - 3u^3 + u^5$ *on the domain* $x \in [0,d]$ *with* $d = 50$*. Left: snaking bifurcation diagram showing both the constant solution and snaking symmetric localised solutions. For clarity, we omit the asymmetric 'rung' solution curves in this panel. Right: a zoomed-in view of the snaking region, rungs included. Thick (thin) lines indicate stable (unstable) solutions; we do not show stability of the snaking curves in the left-hand panel. Labels in the right-hand panel correspond to example solutions in figure 6.2.*

resent solutions with reflectional symmetry in x, but one solution type is symmetric about a particular lattice point, while the other is symmetric about the point midway between two neighbouring lattice points. We refer to the former as site-centred and the latter as bond-centred. As usual, the snakes are connected by rungs of asymmetric localised solutions.

Figures 6.1-6.4 were calculated numerically on the domain $x \in [0,d]$ with periodic boundary conditions. The first example, presented in figures 6.1 and 6.2, is the result of setting $F = -ru - 3u^3 + u^5$; here bistability is the product of a subcritical pitchfork bifurcation followed by a saddle-node, analogous to the SHE introduced in Chapter 1

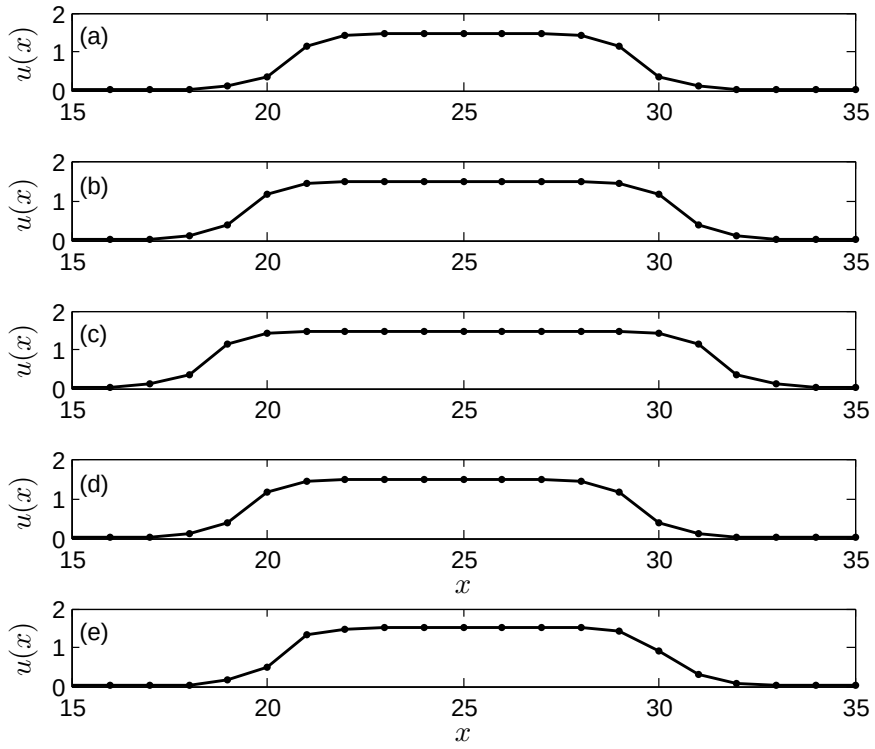

Figure 6.2: *Example solutions of (6.0.1), obtained numerically with $u \equiv u(x)$ and $F(u;r) = -ru - 3u^3 + u^5$ on the domain $x \in [0,d]$ with $d = 50$, zoomed in to the range $x \in [15,35]$. Labels correspond to points indicated in figure 6.1. Panels (a)-(c) show site-centred solutions, panel (d) a bond-centred solution and panel (e) an asymmetric 'rung' solution.*

studied in Chapters 3-5. On the other hand, figures 6.3 and 6.4 show the bifurcation diagram and example solutions for $F = -r - 2u + u^3$. In this case bistability is due to a pair of saddle-nodes which together form an S-shaped solution curve. The solution measure used is $\sum_{x=0}^{d} u(x)$; although not a norm in the strict sense, this choice is motivated by the desire that the visual representation of each loop of the snake is distinct in the latter example. We remark that the former example is invariant under the reflection $u \to -u$, and so figure 6.1 can be reflected in the r-axis, while the latter is invariant under the rotation in phase-space $(u,r) \to (-u,-r)$, and so there exists a second set of snaking curves emerging near the upper saddle-node in figure 6.3. We will apply the

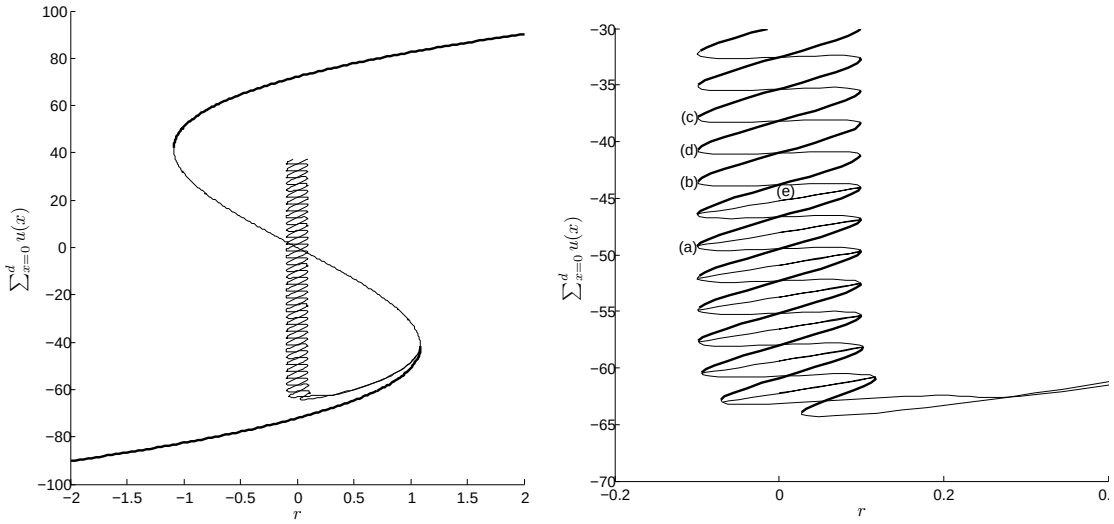

Figure 6.3: *Saddle-saddle snaking bifurcation diagram produced by solving (6.0.1) with* $u \equiv u(x)$ *and* $F(u;r) = -r - 2u^3 + u^3$ *on the domain* $x \in [0,d]$ *with* $d = 50$. *Left: snaking bifurcation diagram showing both the constant solution and snaking symmetric localised solutions. For clarity, we omit the asymmetric 'rung' solution curves in this panel. Right: a zoomed-in view of the snaking region, rungs included. Thick (thin) lines indicate stable (unstable) solutions; we do not show stability of the snaking curves in the left-hand panel. Labels in the right-hand panel correspond to example solutions in figure 6.4.*

analytical results derived in this chapter to both these examples in Chapter 7.

In order to study the pinning mechanism and resulting snaking behaviour asymptotically, we replace $F(u;r)$ by $\epsilon^2 F(u;r)$ in (6.0.1), where $0 < \epsilon \ll 1$, yielding

$$\frac{\partial u}{\partial t} = \Delta u - \epsilon^2 F(u;r). \tag{6.0.3}$$

Rescaling as $(X,Y,T) = (\epsilon x, \epsilon y, \epsilon^2 t) \in \mathbb{R}^2 \times [0,\infty)$ and dividing through by ϵ^2, we achieve

$$\begin{aligned}\frac{\partial u}{\partial T} = \frac{1}{\epsilon^2}\,[&u(X+\epsilon,Y,T) + u(X-\epsilon,Y,T) + u(X,Y+\epsilon,T) + u(X,Y-\epsilon,T)\\ &-4u(X,Y,T)] - F(u;r),\end{aligned} \tag{6.0.4}$$

which is the second-order finite difference approximation of the continuous reaction-

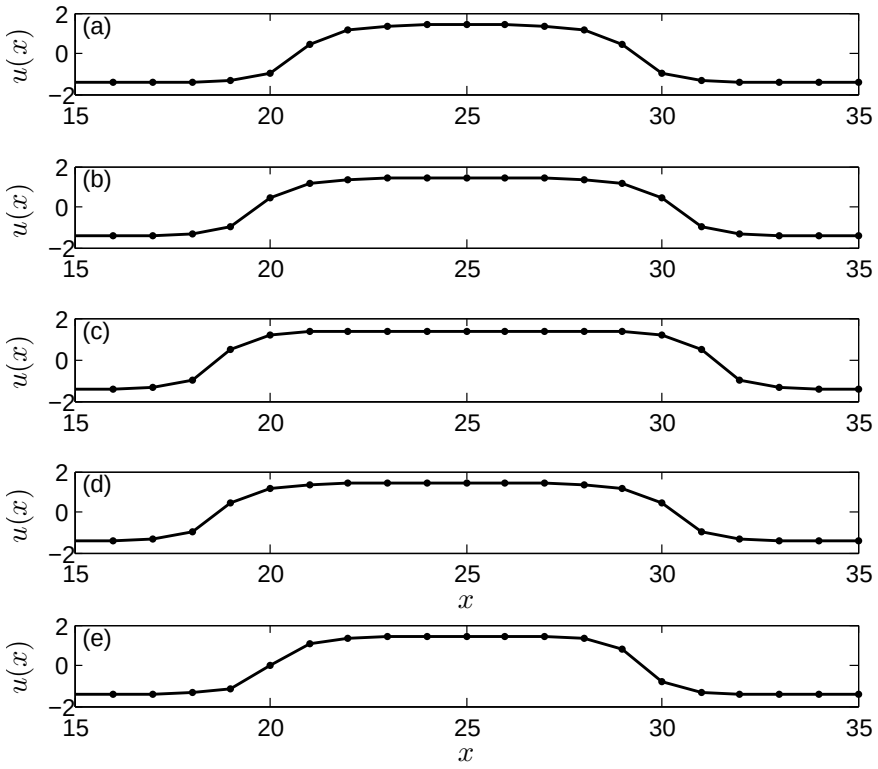

Figure 6.4: *Example solutions of (6.0.1), obtained numerically with $u \equiv u(x)$ and $F(u;r) = -ru - 2u + u^3$ on the domain $x \in [0,d]$ with $d = 50$, zoomed in to the range $x \in [15,35]$. Labels correspond to points indicated in figure 6.3. Panels (a)-(c) show site-centred solutions, panel (d) a bond-centred solution and panel (e) an asymmetric 'rung' solution.*

diffusion equation

$$\frac{\partial u}{\partial T} = \left(\frac{\partial^2}{\partial X^2} + \frac{\partial^2}{\partial Y^2} \right) u - F(u;r), \tag{6.0.5}$$

with a mesh spacing of ϵ. (6.0.5) can be derived directly from (6.0.4) in the limit $\epsilon \to 0$ by a Taylor expansion in ϵ truncated at leading order; thus (6.0.5) is the continuous analogue of (6.0.3) (and (6.0.1)). Note, however, that (6.0.5) is invariant under rotations, while (6.0.3) is not.

The formulation (6.0.3) corresponds to scaling the system close to bifurcation, a viewpoint common to nonlinear dynamical approaches in continuous systems, as in Chapters 3-5 (see also [13, 22, 39] for snaking examples, and [33] for a comprehensive review

of others). This is equivalent to the limit of small mesh spacing described by (6.0.4), but we shall continue to use the language of nonlinear dynamics in order to facilitate comparison of the present chapter with previous chapters on continuous snaking, as well as with other work. We note that any specific nonlinearity may require rescaling before it is in the form (6.0.3), as we shall see in Chapter 7 where we shall apply the results derived here to specific examples.

6.1 Rotation into the plane

Figures 6.1 and 6.3 comprise solutions to (6.0.1) which are functions of x only. Matters become somewhat more complicated when one-dimensional solutions are rotated into the plane. In the SHE (3.0.1) and similar continuous systems, and in the continuous analogue (6.0.5) of (6.0.1), a solution can be rotated at will without affecting it. In contrast, a one-dimensional solution to a discrete problem such as (6.0.1) cannot be freely rotated due to the presence of the lattice; a solution depends quantitatively on its orientation. In particular, fronts cannot pin to the lattice if the tangent of the angle of orientation is irrational, for reasons we shall elucidate presently, in which case the width of the snaking region collapses to zero. This phenomenon has been the subject of much study from a dynamical systems point of view [44, 48, 65]. The present calculation complements the more general results derived in such work, allowing us to observe explicitly the pinning mechanism and the vanishing of the snaking region at irrational orientations.

We shall consider a one-dimensional solution to (6.0.3) by defining

$$z = x\cos\psi + y\sin\psi, \qquad \psi \in [0, 2\pi). \tag{6.1.1}$$

and writing $u \equiv u(z,t)$. Here ψ is the angle of orientation of the solution in the plane, measured anticlockwise from the x-axis. The difference operator (6.0.2) is therefore

rendered

$$\Delta u(z,t) = u(z+\cos\psi,t) + u(z-\cos\psi,t) + u(z+\sin\psi,t) + u(z-\sin\psi,t) - 4u(z,t). \tag{6.1.2}$$

Thus ψ retains an explicit presence in the rotated, one-dimensional version of (6.0.3), in contrast to its continuous analogue (6.0.5) which is invariant under rotations. It is of course the lattice which prevents such free rotation of the axes.

The importance of the rationality of ψ can be inferred by considering the spatial domain of (6.1.2), which is the discrete, countable set

$$\Psi := \left\{ x\cos\psi + y\sin\psi \mid (x,y) \in \mathbb{Z}^2 \right\}. \tag{6.1.3}$$

We also define the extended set of rational numbers

$$\mathbb{Q}_\infty := \mathbb{Q} \cup \{\pm\infty\}, \tag{6.1.4}$$

where we assign $\tan(\pm\frac{\pi}{2}) = \pm\infty$. If $\tan\psi \in \mathbb{Q}_\infty$, then we can set

$$\tan\psi = \frac{m_2}{m_1}, \qquad (m_1,m_2) \in \mathbb{Z}^2\backslash\{(0,0)\}, \qquad \gcd(|m_1|,|m_2|) = 1, \tag{6.1.5}$$

without loss of generality, in which case Ψ is rendered

$$\Psi := \left\{ \frac{m_1 x + m_2 y}{\sqrt{m_1^2+m_2^2}} \;\middle|\; (x,y) \in \mathbb{Z}^2 \right\}. \tag{6.1.6}$$

Since $m_1x + m_2y$ is an integer, Ψ has a well-defined lattice spacing of $(m_1^2+m_2^2)^{-1/2}$. Note that a point on the 'effective', one-dimensional lattice Ψ is only a point on the 'actual', two-dimensional lattice $(x,y) \in \mathbb{Z}^2$ if $m_1x + m_2y = k\left(m_1^2+m_2^2\right)$ for some $k \in \mathbb{Z}$. However, the value of u at the actual lattice point (x,y) is equal to that of u at the (m_1x+m_2y)th effective lattice point in Ψ, as indicated in figure 6.5.

In contrast, if $\tan\psi$ is irrational and finite, then Ψ is a dense (and countably infinite) set. As a consequence, any point on the real line is arbitrarily close to a point in Ψ. Thus there is no well-defined lattice spacing for irrational $\tan\psi$, without which a front cannot pin to the lattice. We therefore expect snaking to occur only when $\tan\psi$ is rational or infinite, i.e. when $\tan\psi \in \mathbb{Q}_\infty$.

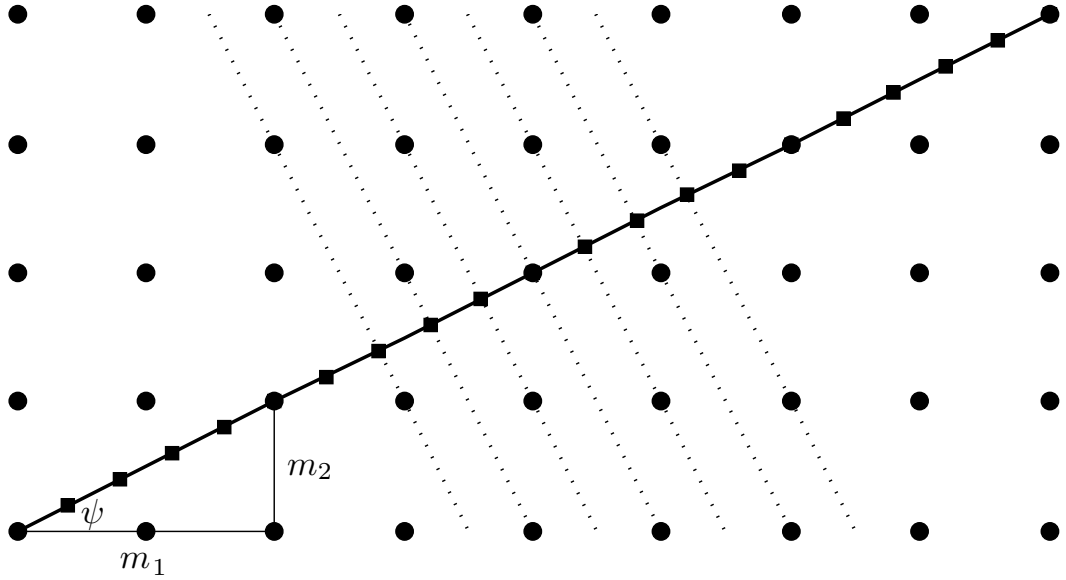

Figure 6.5: *The effective (one-dimensional) lattice* $(m_1 x + m_2 y)(m_1^2 + m_2^2)^{-1/2}$ *with rational* $\tan\psi = m_2/m_1$*, superimposed onto the actual (two-dimensional) lattice* $(x, y) \in \mathbb{Z}^2$*. Actual lattice points are represented by circles; effective ones by squares. The independent variable* z *varies in the direction of the solid line;* z *is constant in the direction of the dotted lines, which also indicate the correspondence of effective to actual lattice points.*

6.2 Exponential asymptotics

We shall now discuss the motivation behind applying exponential asymptotics to the discrete problem (6.0.3). With $u \equiv u(z,t)$, (6.0.3) becomes

$$\frac{\partial u(z,t)}{\partial t} = \Delta u(z,t) - \epsilon^2 F(u(z,t);r), \tag{6.2.1}$$

where z is defined as in (6.1.1) and $\Delta u(z,t)$ is given in (6.1.2). Note (6.2.1) has continuous analogue

$$\frac{\partial u}{\partial T} = \frac{\partial^2 u}{\partial Z^2} - F(u;r), \tag{6.2.2}$$

where

$$Z = \epsilon\,(z - z_0)\,. \tag{6.2.3}$$

We include the (constant) origin z_0 in order to enable the derivation of the pinning mechanism later on; although the continuous equation (6.2.2) is invariant under translations in space, the discrete equation (6.2.1) is not, due to the presence of the lattice. Fixing z_0 therefore corresponds to the pinning of a front to the lattice. This is analogous to fixing the phase of the spatial oscillations in the SHE in Chapter 4, and is done in a similar manner. We will expound upon the significance of z_0 and the means by which it can be fixed presently.

We define u_c to be a constant solution of (6.2.1), so that $F(u_c; r) = 0$. We can investigate the stability of u_c by setting $u = u_c + \hat{u}e^{\sigma t + ikz}$ in (6.2.1), where $k \in [0, 2\pi)$, and linearising with $|\hat{u}| \ll 1$. Thus we obtain the growth rate equation

$$\sigma \sim -2\left[2 - \cos(k\cos\psi) - \cos(k\sin\psi)\right] - \epsilon^2 F_u\left(u_c; r\right), \tag{6.2.4}$$

where the subscript u denotes the first derivative of F with respect to u. Hence u_c is linearly stable provided $F_u\left(u_c; r\right) > 0$, but becomes linearly unstable to perturbations with small wavenumber k as $F_u\left(u_c; r\right)$ becomes negative. We can therefore describe the dynamics of (6.2.1) close to bifurcation using the double limit $\epsilon \to 0$ and $k \to 0$, under which (6.2.4) becomes

$$\sigma \sim -k^2 - \epsilon^2 F_u\left(u_c; r\right). \tag{6.2.5}$$

This suggests that (6.2.1) evolves with the slow scales $(Z, T) = (\epsilon(z - z_0), \epsilon^2 t)$ as $\epsilon \to 0$, precisely the scales on which the continuous analogue (6.2.2) varies. Note again the origin z_0, as yet undetermined. The instability of u_c to modes with small wavenumber is in contrast to the equivalent situation in the SHE (3.0.1), in which the zero solution loses stability to modes with wavenumber ± 1 [13]; such an instability is pattern-forming and produces a spatial structure to which fronts may pin (see Chapter 3). No such pattern-forming mechanism is present in the second-order equation (6.2.2). As there is no spatial structure in the continuous analogue, there is nothing for a front to pin to; therefore the leading-order continuum approximation to (6.2.1) does not snake. However, snaking persists in numerical computations of (6.2.1) even very close to bifurca-

tion, indicating that the continuum approximation (6.2.2) does not tell the whole story. This discrepancy can be resolved by incorporating higher-order effects in the asymptotic solution to (6.2.1), in particular those which are exponentially small. To do this we shall employ the method of exponential asymptotics [1, 7, 72], in a similar manner as in Chapter 4.

To recap briefly, when the leading-order solution to a singular perturbation problem contains singularities, the resultant asymptotic expansion is divergent. If it is truncated optimally by truncating after the least term, the remainder can be shown to be exponentially small. The equation governing the remainder is inhomogeneous, with forcing arising as a consequence of truncation. This forcing is maximal near Stokes lines—certain lines in the complex plane emanating from singularities of the leading-order solution—and a careful rescaling in the vicinity of these lines shows that the coefficient of an exponentially growing complementary function of the remainder equation varies smoothly from zero to non-zero as they are crossed [7]. Such unbounded contributions must be eliminated if the expansion is to remain non-uniform, invariably resulting in a solvability condition on the leading-order solution [1, 22, 39, 51].

In the current context, we shall find that eliminating unbounded terms in the remainder fixes the location of the origin z_0 of a stationary front with respect to the lattice. This is precisely the pinning mechanism by which the snaking region is generated. Furthermore, in a similar manner as in Chapter 4, the inclusion of an exponentially small deviation from the Maxwell point leads to a relation between the origin of the front and the distance from the Maxwell point, which can only be satisfied within a certain exponentially small region—the snaking region. Once the full expansion for a front is known, two back-to-back fronts may be matched together. This results in a set of formulae which fully describe the snakes-and-ladders bifurcation of the structure snaking region, the ultimate aim of this study. Previous work by King and Chapman [51] derived the condition on the origin of the front in a purely one-dimensional sys-

tem; however, they did not study snaking explicitly, nor did they consider the rotation of solutions into the plane. Thus the current calculation represents a significant extension of that work.

The present calculation is in some respects simpler than analogous work in the SHE (see Chapters 4 and 5 and [22, 39]). For instance, the appropriate method of studying continuous pattern formation near onset is that of multiple scales, rather than the relatively simpler continuum approximation employed in discrete problems. Moreover, the nonlinearities present in the SHE lead to an ever-increasing number of harmonics e^{kix} at each order of ϵ, with the obvious consequence of an ever-increasing number of equations determining their coefficients (see Section 4.2.2). That said, the Taylor expansion of slow differences results in what is in effect an infinite-order differential equation, and so the current calculation is not without its own complexities.

6.3 Setting up the beyond-all-orders calculation

We shall now prepare the way for the application of the exponential asymptotic method to (6.2.1) as $\epsilon \to 0$. With $u \equiv u(Z,T)$, we have $u(z \pm \cos\psi, t) \to u(Z \pm \epsilon\cos\psi, T)$ and $u(z \pm \sin\psi, t) \to u(Z \pm \epsilon\sin\psi, T)$. The small-$\epsilon$ limit can therefore be exploited to expand the difference operator Δu (6.1.2) in powers of ϵ using Taylor's theorem, rendering (6.2.1) as

$$\epsilon^2\frac{\partial u}{\partial T} = 2\sum_{p=1}^{\infty}\epsilon^{2p}\frac{\cos^{2p}\psi + \sin^{2p}\psi}{(2p)!}\frac{\partial^{2p}u}{\partial Z^{2p}} - \epsilon^2 F(u;r). \tag{6.3.1}$$

Note that only even powers of ϵ are present. The leading order approximation to (6.2.1) is therefore simply the continuous analogue (6.2.2).

Seeking a stationary solution to (6.2.1) in the form of a (truncated) asymptotic expansion, we now write $u(Z,T) \equiv u(Z)$ and expand as

$$u(Z) \sim \sum_{n=0}^{N-1}\epsilon^{2n}u_n(Z) + R_N(z,Z). \tag{6.3.2}$$

In an abuse of notation, we have retained z-dependence in the remainder R_N, for reasons to be expounded upon presently. The expansion (6.3.2) has been truncated after N terms; if we choose the point of truncation optimally by truncating at the point at which it starts to diverge, the remainder will be exponentially small in ϵ, thus allowing us to investigate exponentially small effects. In particular, the evaluation of the remainder will allow the rigorous matching of back-to-back fronts, providing a formula for the (exponentially small) snaking region in the limit $\epsilon \to 0$.

Now, the leading order (steady) contribution to (6.3.1) is

$$0 = \frac{\mathrm{d}^2 u_0}{\mathrm{d}Z^2} - F(u_0; r), \tag{6.3.3}$$

which is of course simply the steady version of (6.2.2). We shall assume that $u_0(Z)$ takes the form of a stationary front, and hence impose the boundary conditions

$$u_0 \to u_\pm \text{ as } Z \to \pm\infty, \tag{6.3.4}$$

where $u_\pm$ are stable, constant solutions of (6.0.3) and therefore satisfy

$$F(u_\pm; r) = 0, \qquad F_u(u_\pm; r) > 0. \tag{6.3.5}$$

We shall also assume, without loss of generality, that $u_- < u_+$, as the front with opposite orientation in the plane is simply given by the rotation $\psi \to \psi + \pi$.

In order to investigate the phenomenon of homoclinic snaking, we shall restrict our attention to the class of functions $F(u; r)$ where front solutions to (6.3.3), connecting the two constant solutions $u_\pm$, exist only at a particular value of the bifurcation parameter, $r = r_M$ say. This is the Maxwell point, the point in parameter space at which travelling waves connecting u_- to u_+ have zero velocity, as discussed the introductory chapter and in Section 3.2. Because (6.3.3) can be integrated once, the constant solutions $u_\pm$ must also satisfy its first integral; thus we impose

$$\int_{u_-}^{u_+} F(v; r)\mathrm{d}v = 0. \tag{6.3.6}$$

r_M can therefore be defined as the value of r satisfying $F(u_\pm; r) = 0$ and (6.3.6). Note that these conditions form a system of three algebraic equations in the three unknowns $u_\pm$ and r_M, providing a means of determining the Maxwell point. From this we might (erroneously) infer that stationary fronts exist only at the Maxwell point, in direct contradiction of numerical results showing homoclinic snaking within a well-defined region of parameter space centred on the Maxwell point (see figures 6.1 and 6.3). A standard continuum approximation cannot reconstruct such behaviour, as snaking does not occur within an algebraically small distance from r_M but an exponentially small distance; such scales are indistinguishable by techniques based solely on algebraic powers of ϵ.

We remark that for some choices of F the integral condition (6.3.6) is satisfied without the need to impose a specific value of r. For example, if we choose $F = r \sin u$, $u_+ = 2\pi$ and $u_- = 0$ then (6.3.6) is true for all $r > 0$. For such an F snaking does not occur, as there is no Maxwell point and front solutions to the leading-order approximation may be found across an interval of r-values rather than at a specific point. However, fronts still pin to the lattice in such a case, and so much of the following calculation remains relevant.

In order to incorporate exponentially small deviations from the Maxwell point into subsequent calculations, we write $r = r_M + \delta r$ and expand $F(u; r)$ around r_M as

$$F(u; r_M + \delta r) \sim F_M(u) + \delta r F_{r,M}(u), \tag{6.3.7}$$

where we define

$$F_M(u) := F(u; r_M), \qquad F_{r,M}(u) := \left.\frac{\partial F}{\partial r}\right|_{r=r_M}. \tag{6.3.8}$$

We assume that $F_{r,M} \neq 0$ for simplicity, but note that the present work may in principle be extended to choices of F whose first non-zero derivative with respect to r at the Maxwell point is of higher order. δr is thus the bifurcation parameter we shall use to describe the snaking bifurcations; it will turn out to be exponentially small. In principle,

one should also include further algebraic corrections to the Maxwell point by writing $r = r_M + \epsilon^2 r_2 + \cdots + \epsilon^{2N-2} r_{2N-2} + \delta r$; each of the r_j can be fixed by successive solvability conditions at each order in ϵ^2 (see (4.1.8) and the subsequent discussion in Chapter 4). However, only the leading order term r_M and the exponentially small remainder δr are important to the present calculation, so we shall not discuss such algebraic terms further.

Although exponentially small in ϵ, the remainder $R_N(Z)$ will be shown to be exponentially growing in Z. Eliminating unbounded contributions results in an existence condition for stationary front solutions to (6.2.1), characterised by a fixing of the origin of the front in terms of the the bifurcation parameter δr. The existence criterion which determines the origin z_0 will therefore describe the pinning of the front solution to the underlying lattice, the mechanism responsible for snaking bifurcations. Furthermore, matching two fronts and eliminating the unbounded contributions to the remainder will produce a set of matching conditions relating δr, the origin of each front and the separation distance between the two. It is precisely these matching conditions which describe the snakes-and-ladders bifurcations analytically, the ultimate aim of the present calculation.

6.4 The remainder equation

Although an expression for the large-n terms in (6.3.2) is necessary in order to evaluate the remainder R_N explicitly, we are able at this point to derive the complementary functions of its governing equation. It is these which will be switched on as Stokes lines are crossed. Furthermore, we are able to determine the forcing due to the deviation δr from the Maxwell point and see how exponentially small terms can lead to a solvability condition on the leading-order front.

The leading-order contribution to R_N is simply the linearisation of the steady version

of (6.2.1) around u_0, with $F(u;r)$ linearised about the Maxwell point as in (6.3.7), which is

$$\begin{aligned}&[R_N(z+\cos\psi, Z+\epsilon\cos\psi)+R_N(z-\cos\psi, Z-\epsilon\cos\psi)+R_N(z+\sin\psi, Z+\epsilon\sin\psi)\\&+R_N(z-\sin\psi, Z-\epsilon\sin\psi)-4R_N(z,Z)]-\epsilon^2F'_M(u_0(Z))R_N(z,Z)\\&\qquad\qquad\sim \epsilon^2\delta r F_{r,M}(u_0(Z))+\text{ forcing due to truncation,}\end{aligned} \tag{6.4.1}$$

where the exact scalings of R_N and δr, while exponentially small, are yet to be determined. As (6.4.1) is linear, and autonomous with regard to the fast scale z, we can look for a solution to the homogeneous equation of the form

$$R_N(z,Z) = e^{i\kappa z}S_N(Z)+\text{c.c.}, \tag{6.4.2}$$

for some eigenvalue $\kappa\in\mathbb{C}$, and Taylor expand the slow-scale differences in powers of ϵ. This results in

$$\begin{aligned}&e^{i\kappa z}\Big\{2\left[\cos(\kappa\cos\psi)+\cos(\kappa\sin\psi)-2\right]S_N+2i\epsilon\left[\cos\psi\sin(\kappa\cos\psi)+\sin\psi\sin(\kappa\sin\psi)\right]S'_N\\&+\epsilon^2\left[\cos^2\psi\cos(\kappa\cos\psi)+\sin^2\psi\cos(\kappa\sin\psi)\right]S''_N-\epsilon^2F'_M(u_0(Z))S_N\Big\}+\mathrm{O}\left(\epsilon^3R_N\right)=0.\end{aligned} \tag{6.4.3}$$

Expanding S_N as

$$S_N(Z) = S_{N,0}(Z)+\epsilon S_{N,1}(Z)+\epsilon^2S_{N,2}(Z)+\cdots, \tag{6.4.4}$$

then, if $S_{N,0}$ is to be non-zero, we obtain at $\mathrm{O}(1)$ the condition

$$\cos(\kappa\cos\psi)+\cos(\kappa\sin\psi)-2=0. \tag{6.4.5}$$

Real solutions to (6.4.5) are given by $\kappa\cos\psi = 2M_1\pi$ and $\kappa\sin\psi = 2M_2\pi$, for any $(M_1,M_2)\in\mathbb{Z}^2$; these exist only when $\tan\psi\in\mathbb{Q}_\infty$. Hence there are no real, non-zero solutions to (6.4.5) for irrational $\tan\psi$. Note that (6.4.5) also admits complex solutions in general. If $\tan\psi\in\mathbb{Q}_\infty$ and $\kappa\in\mathbb{R}$, we may therefore set

$$\begin{aligned}\cos\psi = \frac{m_1}{\sqrt{m_1^2+m_2^2}},\qquad \sin\psi = \frac{m_2}{\sqrt{m_1^2+m_2^2}},\\(m_1,m_2)\in\mathbb{Z}^2\backslash\{(0,0)\},\qquad \gcd(|m_1|,|m_2|)=1,\end{aligned} \tag{6.4.6}$$

without loss of generality. This then gives

$$\kappa = 2M\pi\sqrt{m_1^2 + m_2^2}, \qquad M \in \mathbb{Z}. \tag{6.4.7}$$

Of particular note are the axes and principal diagonals $\psi = \frac{k\pi}{4}$, $k \in \{0, 1, \ldots, 7\}$, which correspond to either $\cos\psi$ having unit modulus and $\sin\psi$ vanishing, or vice versa, or both $\cos\psi$ and $\sin\psi$ having modulus $1/\sqrt{2}$. In each of these eight instances, (6.4.7) describes all solutions to (6.4.5); there are no complex solutions.

If ψ and κ satisfy (6.4.6) and (6.4.7) respectively, we find that $\mathrm{O}(\epsilon)$ terms also vanish in (6.4.3). Proceeding to $\mathrm{O}(\epsilon^2)$, we then obtain

$$S''_{N,0} - F'_M(u_0(Z))S_{N,0} = 0. \tag{6.4.8}$$

As u_0 satisfies (6.3.3), the complementary functions of (6.4.8) are

$$g(Z) := u_0'(Z), \qquad G(Z;\zeta) := u_0'(Z)\int_\zeta^Z \frac{1}{u_0'(t)^2}\mathrm{d}t, \tag{6.4.9}$$

where $g(Z)$ can be found by noting that (6.4.8) with $S_{N,0} = u_0'$ is simply the first derivative of (6.3.3), after which $G(Z;\zeta)$ can readily be found using the method of reduction of order. The parameter ζ is a (complex) singularity of $u_0(Z)$, included to simplify subsequent calculations. Thus each real κ provides a contribution to R_N of the form $e^{i\kappa z}(a_\kappa g + A_\kappa G)$, for some constants a_κ and A_κ.

We now turn our attention to complex ($\Im(\kappa) \neq 0$) solutions of (6.4.5), noting that there are no non-zero, purely imaginary solutions to (6.4.5). Requiring that $\mathrm{O}(\epsilon)$ terms in (6.4.3) vanish, we must have either

$$[\cos\psi\sin(\kappa\cos\psi) + \sin\psi\sin(\kappa\sin\psi)] = 0 \tag{6.4.10}$$

or

$$S'_{N,0} = 0. \tag{6.4.11}$$

It can be shown that if κ is complex and satisfies (6.4.5) then it does not satisfy (6.4.10); we defer this calculation to Appendix A. Thus, if κ is complex, we have $S_{N,0} = B_\kappa$, for some constant B_κ.

Finally, we may seek the particular integral of (6.4.1) due to the term involving δr. Setting $R_N(z, Z) = \delta r P(Z)$, we obtain at leading order

$$P'' - F'_M(u_0(Z))P = F_{r,M}(u_0(Z)), \tag{6.4.12}$$

which can be solved using the method of variation of parameters to give

$$P(Z) = u'_0(Z) \int^Z \frac{1}{u'_0(t)^2} \left[\int_{u_-}^{u_0(t)} F_{r,M}(v) \mathrm{d}v \right] \mathrm{d}t. \tag{6.4.13}$$

Combining the contributions for real and complex κ and the particular integral, the leading-order solution to (6.4.1) is thus

$$R_N(z, Z) \sim \delta r P(Z) + \sum_{\kappa \in \mathbb{R}} e^{i\kappa z} \left[a_\kappa g(Z) + A_\kappa G(Z; \zeta) \right] + \sum_{\kappa \notin \mathbb{R}} e^{i\kappa z} B_\kappa, \tag{6.4.14}$$

for arbitrary constants a_κ, A_κ and B_κ. Crucially, the form of the solution is dependent upon the rationality of $\tan\psi$. If $\tan\psi \in \mathbb{Q}_\infty$, we can define ψ as in (6.4.6), in which case real κ are given by (6.4.7). Recall that if $\psi = \frac{k\pi}{4}$ with $k \in \{0, 1, \ldots, 7\}$ then all solutions are purely real and the second summation does not contribute; however, this is not the case for $\tan\psi \in \mathbb{Q}_\infty$ in general. On the other hand, if $\tan\psi \notin \mathbb{Q}_\infty$, then the only real solution to (6.4.5) is $\kappa = 0$, and so the first summation consists of only this one value of κ.

We also note that if $\tan\psi$ is rational or infinite then $\kappa z = 2M\pi(m_1 x + m_2 y)$; hence $e^{i\kappa z} = 1$ on lattice points. However, writing R_N in the form (6.4.14) will prove to be useful later on, when we come to evaluate the effects of the as yet unknown forcing in (6.4.1), and so we shall continue to write $e^{i\kappa z}$ even when $\kappa \in \mathbb{R}$.

6.4.1 The form of the solvability condition

We are now able to infer the source of the beyond-all-orders solvability condition which determines the origin of the leading-order front. Linearising (6.3.3) around the constant solutions $u_0(Z) \equiv u_\pm$, we can find expressions for u_0 in the far-fields, namely

$$u_0 \sim u_\pm \mp D_\pm e^{\mp\alpha_\pm Z} \text{ as } Z \to \pm\infty, \tag{6.4.15}$$

where

$$\alpha_\pm := +\sqrt{F'_M(u_\pm)} > 0 \tag{6.4.16}$$

and $D_\pm > 0$. Therefore the complementary functions defined in (6.4.9) are given by

$$g \sim \alpha_\pm D_\pm e^{\mp\alpha_\pm Z}, \tag{6.4.17}$$

$$G \sim \pm\frac{1}{2\alpha_\pm^2 D_\pm} e^{\pm\alpha_\pm Z} \tag{6.4.18}$$

as $Z \to \pm\infty$, and the particular integral is

$$P \sim \begin{cases} \left(2\alpha_+^2 D_+\right)^{-1} \left(\int_{u_-}^{u_+} F_{r,M}(v)\mathrm{d}v\right) e^{\alpha_+ Z}, & Z \to \infty, \\ -F_{r,M}(u_-)/\left(\alpha_-^2\right), & Z \to -\infty. \end{cases} \tag{6.4.19}$$

Thus there appears exponential growth in G as $Z \to \pm\infty$, and in P as $Z \to \infty$. As a consequence, one may be tempted to set both the coefficient of G and δr to zero in order to eliminate this, and conclude erroneously that a different approach is required. In fact, the exponential growth is not so easily removed; we shall see that the as yet undetermined forcing due to truncation of the divergent series (6.3.2) results in a non-zero multiple of G being present as $Z \to \infty$. Furthermore, the exponentially small deviation δr from the Maxwell point also produces unbounded terms in the same limit. However, for certain values of the origin z_0 of u_0, which can be defined in terms of δr, these unbounded terms have coefficient zero. This is only the case if δr lies within an exponentially small range of values—the snaking region. Thus we shall see that homoclinic snaking is a direct result of the pinning of fronts to the lattice.

6.5 Calculation of late terms in the expansion

In order to determine the point of truncation and the unknown forcing in the remainder equation (6.4.1), we require an asymptotic formula for the nth term in the expansion (6.3.2) as $n \to \infty$. In light of the Taylor expansion (6.3.1) of the difference equation (6.2.1) in the continuum limit, we can see that the nth term is given by differentiating

the $(n-1)$th term four times and integrating twice, and so on. Therefore, if u_0 is singular at some point(s) in the complex plane, the expansion (6.3.2) is divergent in the form of a factorial over a power [7, 51]. Hence we propose the ansatz

$$u_n \sim (-1)^n \frac{\Gamma(2n+\beta)}{W(Z)^{2n+\beta}} \left(f_0(Z) + \frac{1}{2n} f_1(Z) + \frac{1}{(2n)^2} f_2(Z) + \cdots \right) \tag{6.5.1}$$

as $n \to \infty$, in which all dependence on n and Z has been written down explicitly and the large-n limit has been exploited in order to write u_n as a series in inverse powers of n. Therefore the equation for u_n as $n \to \infty$, $n \leq N-1$, given by equating terms in (6.2.1) at $\mathrm{O}\left(\epsilon^{2n+2}\right)$, is

$$0 = 2 \sum_{p=1}^{n+1} \frac{\cos^{2p}\psi + \sin^{2p}\psi}{(2p)!} \frac{\mathrm{d}^{2p} u_{n-p+1}}{\mathrm{d}Z^{2p}} - F_M'(u_0)\, u_n + \cdots, \tag{6.5.2}$$

where the neglected terms contribute at higher orders in $1/n$.

In light of (6.5.1), the derivative terms in (6.5.2) are therefore $\mathrm{O}\left(\Gamma(2n+2+\beta)\right)$, whereas the terms arising due to the expansion of $F_M(u)$ around u_0 are merely $\mathrm{O}\left(\Gamma(2n+\beta)\right)$. As a result, the leading-order contribution to (6.5.2) is

$$0 = 2(-1)^{n+1} \frac{\Gamma(2n+2+\beta)}{W^{2n+\beta+2}} \sum_{p=1}^{n+1} (-1)^p \frac{\cos^{2p}\psi + \sin^{2p}\psi}{(2p)!} (W')^{2p} f_0 \tag{6.5.3}$$

The summation is dominated by $p = \mathrm{O}(1)$, and so we can replace the upper limit with infinity to give

$$0 = \sum_{p=0}^{\infty} (-1)^p \frac{(W'\cos\psi)^{2p} + (W'\sin\psi)^{2p}}{(2p)!} - 2. \tag{6.5.4}$$

Evaluating the summation, we therefore have

$$0 = \cos(W'\cos\psi) + \cos(W'\sin\psi) - 2. \tag{6.5.5}$$

This is precisely the eigenvalue equation (6.4.5) derived in Section 6.4. Hence we set $W' = \kappa$, where κ is a (possibly complex) *non-zero* solution to (6.4.5). Recall the existence of real, non-zero solutions is dependent upon the rationality of $\tan\psi$, as discussed in that section. We note that both the eigenvalue equation (6.4.5) and the $\mathrm{O}(\epsilon)$ condition

(6.4.10) are invariant under $\kappa \to -\kappa$ and $\kappa \to \kappa^*$; furthermore, (6.4.5) admits no non-zero, purely imaginary solutions. Therefore we can restrict $W' = \kappa$ to the right half-plane $\Re(\kappa) > 0$ without loss of generality, as replacing W with $-W$ in (6.5.1) results in an additional factor of $(-1)^{-\beta}$, which can simply be absorbed into the f_k. Hence we have

$$W = \kappa\,(Z - \zeta)\,, \tag{6.5.6}$$

where $Z = \zeta$ is a singularity of u_0, and therefore also of each u_n. Since (6.5.2) is linear in u_n, the full solution consists of the sum of the contributions from each singularity ζ, which in turn is the sum of the contributions for each eigenvalue κ, with $\Re(\kappa) > 0$.

We now proceed to higher orders in $1/n$ in (6.5.2) in order to determine β and f_0. As W is a linear function of Z, we have

$$\begin{aligned}\frac{\mathrm{d}^{2p}u_{n-p+1}}{\mathrm{d}Z^{2p}} &= (-1)^{n+p+1}\frac{\Gamma(2n+2+\beta)}{W^{2n+\beta+2}}\kappa^{2p}\left(f_0 + \frac{1}{2n}f_1 + \frac{1}{(2n)^2}\left((2p-2)f_1 + f_2\right)\right)\\ &\quad + (-1)^{n+p}\frac{\Gamma(2n+1+\beta)}{W^{2n+\beta+1}}\kappa^{2p-1}2p\left(f_0' + \frac{1}{2n}f_1'\right)\\ &\quad + (-1)^{n+p-1}\frac{\Gamma(2n+\beta)}{2W^{2n+\beta}}\kappa^{2p-2}2p(2p-1)f_0'' + \mathrm{O}\left(\Gamma(2n-1+\beta)\right).\end{aligned} \tag{6.5.7}$$

After substitution of (6.5.7) and division by $\Gamma(2n+2+\beta)$, we may therefore solve (6.5.2) via derivation of the asymptotic series $f_0 + f_1/(2n) + f_2/(2n)^2 + \cdots$. Thus we obtain

$$\begin{aligned}0 = 2\Bigg\{&\frac{(-1)^{n+1}}{W^{2n+\beta+2}}\Bigg[\sum_{p=1}^{\infty}(-1)^p\frac{(\kappa\cos\psi)^{2p} + (\kappa\sin\psi)^{2p}}{(2p)!}\left(f_0 + \frac{1}{2n}f_1 + \frac{1}{(2n)^2}(f_2 - 2f_1)\right)\\ &- \left(\kappa\cos\psi\sum_{p=1}^{\infty}(-1)^{p-1}\frac{(\kappa\cos\psi)^{2p-1}}{(2p-1)!} + \kappa\sin\psi\sum_{p=1}^{\infty}(-1)^{p-1}\frac{(\kappa\sin\psi)^{2p-1}}{(2p-1)!}\right)\frac{1}{(2n)^2}f_1\Bigg]\\ &+ \frac{(-1)^{n+1}}{W^{2n+\beta+1}}\Bigg[\cos\psi\sum_{p=1}^{\infty}(-1)^{p-1}\frac{(\kappa\cos\psi)^{2p-1}}{(2p-1)!} + \sin\psi\sum_{p=1}^{\infty}(-1)^{p-1}\frac{(\kappa\sin\psi)^{2p-1}}{(2p-1)!}\Bigg]\\ &\times\left(\frac{1}{2n} - \frac{1+\beta}{(2n)^2}\right)\left(f_0' + \frac{1}{2n}f_1'\right) + \frac{(-1)^n}{2W^{2n+\beta}}\Bigg[\cos^2\psi\sum_{p=1}^{\infty}(-1)^{p-1}\frac{(\kappa\cos\psi)^{2p-2}}{(2p-2)!}\\ &+ \sin^2\psi\sum_{p=1}^{\infty}(-1)^{p-1}\frac{(\kappa\sin\psi)^{2p-2}}{(2p-2)!}\Bigg]\frac{1}{(2n)^2}f_0''\Bigg\} - F_M'(u_0)\frac{(-1)^n}{W(Z)^{2n+\beta}}\frac{1}{(2n)^2}f_0 + \cdots\end{aligned} \tag{6.5.8}$$

as $n \to \infty$. Each of these summations may be evaluated explicitly, yielding

$$\begin{aligned}0 = 2\Bigg\{ &\frac{(-1)^{n+1}}{W^{2n+\beta+2}}\Bigg[(\cos(\kappa\cos\psi)+\cos(\kappa\sin\psi)-2)\left(f_0+\frac{1}{2n}f_1+\frac{1}{(2n)^2}(f_2-2f_1)\right)\\ &-(\kappa\cos\psi\sin(\kappa\cos\psi)+\kappa\sin\psi\sin(\kappa\sin\psi))\,\frac{1}{(2n)^2}f_1\Bigg]\\ &+\frac{(-1)^{n+1}}{W^{2n+\beta+1}}\left(\cos\psi\sin(\kappa\cos\psi)+\sin\psi\sin(\kappa\sin\psi)\right)\left(\frac{1}{2n}-\frac{1+\beta}{(2n)^2}\right)\left(f_0'+\frac{1}{2n}f_1'\right)\\ &+\frac{(-1)^n}{2W^{2n+\beta}}\left(\cos^2\psi\cos(\kappa\cos\psi)+\sin^2\psi\cos(\kappa\sin\psi)\right)\frac{1}{(2n)^2}f_0''\Bigg\}\\ &-F_M'(u_0)(-1)^n\frac{1}{W(Z)^{2n+\beta}}\frac{1}{(2n)^2}f_0+\cdots.\end{aligned} \tag{6.5.9}$$

As κ satisfies (6.4.5), the first line on the right-hand side of (6.5.9) vanishes. Because this includes the $\mathrm{O}(1)$ terms, we proceed to $\mathrm{O}(1/n)$ and find that

$$0 = \left[\cos\psi\sin(\kappa\cos\psi)+\sin\psi\sin(\kappa\sin\psi)\right]f_0'. \tag{6.5.10}$$

If κ is real then (6.5.10) is automatically satisfied (see Section 6.4) and we must continue to $\mathrm{O}\left(1/n^2\right)$. The zero eigenvalue does not contribute to u_n, as this would lead to division by zero, so κ can only be real if $\tan\psi \in \mathbb{Q}_\infty$. Thus we can define $\tan\psi = m_2/m_1$ as in (6.4.6), in which case $\kappa = 2M\pi(m_1^2+m_2^2)^{1/2}$ as in (6.4.7), albeit with $M > 0$ as we have fixed $\Re(\kappa) > 0$. Consequently, the first three lines of (6.5.9) vanish and we are left with

$$0 = f_0'' - F_M'\left(u_0(Z)\right)f_0. \tag{6.5.11}$$

This we have already solved; the complementary functions $g(Z)$ and $G(Z;\zeta)$ are defined in (6.4.9). Hence if κ is real then either $f_0 = \lambda_{M,\psi}g$ or $f_0 = \Lambda_{M,\psi}G$, for some constants $\lambda_{M,\psi}$ and $\Lambda_{M,\psi}$, in general dependent on ψ. On the other hand, if κ has non-zero imaginary part then (6.5.10) can only be satisfied if $f_0' = 0$ (see Section 6.4), and we therefore set $f_0 = \Omega_{\kappa,\psi}$ in this case, for some constant $\Omega_{\kappa,\psi}$, also dependent on ψ.

It remains to evaluate β; this is readily achieved by consideration of the singularities of u_0. We shall assume that the singularities of u_0 are all either of the form

$$u_0 = \mathrm{O}\left((Z-\zeta)^{-\gamma}\right) \text{ as } Z \to \zeta, \quad -\gamma \notin \mathbb{N}\cup\{0\}, \tag{6.5.12}$$

or

$$u_0 = \mathrm{O}\left((Z-\zeta)^{-\gamma}\, h\left(\ln\left(Z-\zeta\right)\right)\right) \text{ as } Z \to \zeta, \quad \gamma \in \mathbb{R}, \tag{6.5.13}$$

for some function $h(\ln(t)) \neq At^{\alpha}$ for any constants $(A, \alpha) \in \mathbb{C}^2$. We shall henceforth refer to the constant γ (which we take to be real for simplicity; results are similar for complex γ) as the *strength* of the singularity at ζ. The systems giving rise to figures 6.1 and 6.3 are both examples of an algebraic singularity (6.5.12); [99] is an example of a logarithmic one (6.5.13). By inspection of (6.5.2), we can see that if u_0 has a singularity of strength γ then u_n must have one of strength $2n+\gamma$, as u_n is found by differentiating u_{n-1} four times and integrating twice. Considering the three possible solutions for f_0, g has a singularity of strength $\gamma+1$ and G has one of strength $-\gamma-2$, whereas the constant function has none at all. Thus, substituting (6.5.6) for W into the factorial-over-power (6.5.1) and expanding u_n near the singularity ζ for each f_0 in turn provides the following:

$$f_0 = \lambda_{M,\psi} g \;\Rightarrow\; 2n+\gamma = 2n+\beta+\gamma+1, \tag{6.5.14}$$

$$f_0 = \Lambda_{M,\psi} G \;\Rightarrow\; 2n+\gamma = 2n+\beta-\gamma-2, \tag{6.5.15}$$

$$f_0 = \Omega_{\kappa,\psi} \;\Rightarrow\; 2n+\gamma = 2n+\beta. \tag{6.5.16}$$

These give $\beta = -1$, $\beta = 2\gamma+2$ and $\beta = \gamma$, respectively. Therefore the contribution to u_n from each singularity ζ is

$$\begin{aligned} u_n(Z) \sim \sum_{M=1}^{\infty} \left[\frac{(-1)^n \Gamma(2n-1)\lambda_{M,\psi} g(Z)}{\left[2M\pi\sqrt{m_1^2+m_2^2}(Z-\zeta)\right]^{2n-1}} + \frac{(-1)^n \Gamma(2n+2\gamma+2)\Lambda_{M,\psi} G(Z;\zeta)}{\left[2M\pi\sqrt{m_1^2+m_2^2}(Z-\zeta)\right]^{2n+2\gamma+2}} \right] \\ + \sum_{\substack{\kappa \notin \mathbb{R} \\ \Re(\kappa)>0}} \frac{(-1)^n \Gamma(2n+\gamma)\Omega_{\kappa,\psi}}{\left[\kappa(Z-\zeta)\right]^{2n+\gamma}}. \end{aligned} \tag{6.5.17}$$

We note that when $\tan\psi \notin \mathbb{Q}_\infty$ then the first summation in (6.5.17) does not contribute, there being no real, non-zero eigenvalues. If, on the other hand, $\tan\psi \in \mathbb{Q}_\infty$ then we define ψ as in (6.4.6) and both summations contribute, unless $\psi = \frac{k\pi}{4}$, $k \in \{0, 1, \ldots, 7\}$, in which case there are no complex eigenvalues and the second summation does not contribute.

Clearly, it is the eigenvalues of smallest modulus which are dominant as $n \to \infty$. For eigenvalues of equal size, dominance is then determined by comparing the offsets within the Γ-functions. When $\kappa \in \mathbb{R}$, the dominant eigenvalue is given by $M = 1$. Therefore, if the modulus of the smallest complex eigenvalue is less than $2\pi(m_1^2 + m_2^2)^{1/2}$ then the third term is dominant over the other two. Otherwise, the third term is subdominant to the first two, in which case the second dominates the first provided $\gamma > -\frac{3}{2}$. The question of dominance plays no role in determining the remainder, as each contribution can be considered separately by making use of the superposition principle of linear equations. However, it does become significant when calculating the constant $\Lambda_{1,\psi}$, a prerequisite for accurate comparison with numerical results. This will be discussed in detail in the context of a cubic-quintic nonlinearity in the next chapter.

6.6 Optimal truncation and Stokes lines

We can now turn our attention to the effects of the unknown forcing in the remainder equation (6.4.1). Before we can evaluate it, we must first determine the point of truncation $n = N - 1$, desiring to truncate the expansion optimally so the resultant remainder is exponentially small. To this end, we shall treat the contribution to the expansion from each eigenvalue κ and each singularity ζ separately, as each contribution has a different least term. This we are free to do, since both the large-n equation (6.5.2) and the remainder equation (6.4.1) are linear. We shall therefore for the moment work in terms of a general solution pair (f_0, β), rather than one of the three specific solutions derived in the previous section. In light of the large-n solution (6.5.17), each contribution to u_n is minimal with respect to n when

$$\frac{\mathrm{d}}{\mathrm{d}n}\left|\frac{\epsilon^{2n}\Gamma(2n+\beta)}{[\kappa(Z-\zeta)]^{2n+\beta}}\right| = 0, \tag{6.6.1}$$

where β is determined by the choice of f_0 under consideration. The limit $n \to \infty$ can be exploited in order to approximate this using Stirling's formula, yielding

$$\frac{\mathrm{d}}{\mathrm{d}n}\left(\frac{\epsilon^{2n}\sqrt{2\pi}(2n+\beta)^{2n+\beta-1/2}e^{-2n-\beta}}{|\kappa(Z-\zeta)|^{2n+\beta}}\right)=0. \tag{6.6.2}$$

Collecting exponents gives

$$\frac{\mathrm{d}}{\mathrm{d}n}\exp\left[2n\ln\left(\frac{\epsilon\,(2n+\beta)}{|\kappa(Z-\zeta)|}\right)-2n+\left(\beta-\frac{1}{2}\right)\ln(2n+\beta)\right]=0. \tag{6.6.3}$$

Setting $n = N-1$, we therefore require

$$\ln\left(\frac{\epsilon\,(2N+\beta-2)}{|\kappa(Z-\zeta)|}\right)=0, \tag{6.6.4}$$

yielding

$$N \sim \frac{|\kappa(Z-\zeta)|}{2\epsilon}+\nu, \tag{6.6.5}$$

where $\nu = \mathrm{O}(1)$ is added to ensure N is an integer.

We are now able to evaluate the unknown forcing appearing in (6.4.1). This forcing arises as a result of truncation, and consists of those terms not accounted for by equating coefficients at $\mathrm{O}\left(\epsilon^{2n+2}\right)$ in (6.3.1) for $n = 0, 1, \ldots, N-1$. Considering the u_n equation (6.5.2), it follows that this forcing, denoted henceforth by RHS, is given by the double summation

$$\mathrm{RHS} \sim -2\sum_{m=N}^{\infty}\epsilon^{2m+2}\sum_{p=m-N+2}^{m+1}\frac{\cos^{2p}\psi+\sin^{2p}(\psi)}{(2p)!}\frac{\mathrm{d}^{2p}u_{m-p+1}}{\mathrm{d}Z^{2p}}+\cdots, \tag{6.6.6}$$

where the lower limit of summation in p arises because the asymptotic expansion has been truncated after the Nth term. Since $m \gg 1$ and the range $p = \mathrm{O}(1)$ is dominant, we can make use of (6.5.7) and Stirling's formula to give

$$\begin{aligned}\mathrm{RHS} \sim\ & -2\sqrt{2\pi}\sum_{m=N}^{\infty}\sum_{p=m-N+2}^{\infty}\left[\epsilon^{2m+2}(-1)^{m+1}\frac{(2m+2+\beta)^{2m+3/2+\beta}e^{-(2m+2+\beta)}}{[\kappa(Z-\zeta)]^{2m+2+\beta}}\right]\\ &\times\left[(-1)^{p}\frac{(\kappa\cos\psi)^{2p}+(\kappa\sin\psi)^{2p}}{(2p)!}\right]f_0+\cdots.\end{aligned} \tag{6.6.7}$$

After writing $m = N + \hat{m}$, this is dominated by the range $\hat{m} = \mathrm{O}(1)$ and, because $(t+c)^\alpha = \exp(\alpha \ln(t+c)) \sim t^\alpha e^{\alpha c/t}$ as $t \to \infty$, can be written

$$\begin{aligned}\mathrm{RHS} \sim\ & -2\sqrt{2\pi}(-1)^{N+1}\frac{\epsilon^{2N+2}(2N)^{2N+3/2+\beta}e^{-2N}}{[\kappa(Z-\zeta)]^{2N+2+\beta}}\sum_{\hat{m}=0}^{\infty}\sum_{p=\hat{m}+2}^{\infty}\left[(-1)^{\hat{m}}\frac{\epsilon^{2\hat{m}}(2N)^{2\hat{m}}}{[\kappa(Z-\zeta)]^{2\hat{m}}}\right] \\ & \times\left[(-1)^p\frac{(\kappa\cos\psi)^{2p}+(\kappa\sin\psi)^{2p}}{(2p)!}\right]f_0+\cdots \end{aligned} \tag{6.6.8}$$

as $N \to \infty$. Reversing the order of summation, we now have

$$\begin{aligned}\mathrm{RHS} \sim\ & -2\sqrt{2\pi}(-1)^{N+1}\frac{\epsilon^{2N+2}(2N)^{2N+3/2+\beta}e^{-2N}}{[\kappa(Z-\zeta)]^{2N+2+\beta}} \\ & \times\sum_{p=2}^{\infty}\left[(-1)^p\left(\frac{(\kappa\cos\psi)^{2p}}{(2p)!}+\frac{(\kappa\sin\psi)^{2p}}{(2p)!}\right)\sum_{\hat{m}=0}^{p-2}(-1)^{\hat{m}}\left(\frac{2\epsilon N}{\kappa(Z-\zeta)}\right)^{2\hat{m}}\right]f_0+\cdots. \end{aligned} \tag{6.6.9}$$

This we can evaluate, since

$$\begin{aligned}\sum_{p=2}^{\infty}\left[(-1)^p\frac{v^{2p}}{(2p)!}\sum_{m=0}^{p-2}\left(-w^2\right)^m\right] &= \sum_{p=2}^{\infty}(-1)^p\frac{v^{2p}}{(2p)!}\frac{1+(-1)^p w^{2p-2}}{1+w^2} \\ &= \frac{1}{1+w^2}\left[\cos v-1+\frac{1}{w^2}\left(\cosh(vw)-1\right)\right]. \end{aligned} \tag{6.6.10}$$

Therefore, since κ satisfies (6.4.5), the leading-order forcing due to truncation can be written as

$$\begin{aligned}\mathrm{RHS} \sim\ & 2\sqrt{2\pi}(-1)^N\frac{\epsilon^{2N}(2N)^{2N-1/2+\beta}e^{-2N}}{[\kappa(Z-\zeta)]^{2N-2+\beta}(\kappa^2(Z-\zeta)^2+4\epsilon^2N^2)}\left[\cosh\left(\frac{2\epsilon N\cos\psi}{Z-\zeta}\right)\right. \\ & \left.+\cosh\left(\frac{2\epsilon N\sin\psi}{Z-\zeta}\right)-2\right]f_0+\cdots. \end{aligned} \tag{6.6.11}$$

In order to simplify subsequent calculations we now define

$$\kappa(Z-\zeta) = \rho e^{i\theta}, \tag{6.6.12}$$

which gives $N \sim \rho/(2\epsilon)+\nu$. Therefore we can write the prefactor of (6.6.11) as

$$\begin{aligned}\frac{\epsilon^{2N}(2N)^{2N-1/2+\beta}e^{-2N}}{[\kappa(Z-\zeta)]^{2N-2+\beta}(\kappa^2(Z-\zeta)^2+4\epsilon^2N^2)} &\sim \frac{\epsilon^{1/2-\beta}}{\sqrt{\rho}}\frac{(2\epsilon N/\rho)^{2N-1/2+\beta}\,e^{-i\theta(2N-2+\beta)}e^{-2N}}{e^{2i\theta}+4\epsilon^2N^2/\rho^2} \\ &= \frac{\epsilon^{1/2-\beta}}{\sqrt{\rho}}\frac{(1+2\epsilon\nu/\rho)^{2N-1/2+\beta}\,e^{-i\theta(2N-2+\beta)}e^{-2N}}{e^{2i\theta}+1+4\epsilon\nu/\rho+4\epsilon^2\nu^2/\rho^2} \\ &\sim \frac{\epsilon^{1/2-\beta}}{\sqrt{\rho}}\frac{e^{2\epsilon\nu(\rho/\epsilon+2\nu-1/2+\beta)/\rho}e^{-i\theta(2N-2+\beta)}e^{-\rho/\epsilon-2\nu}}{e^{2i\theta}+1} \\ &\sim \frac{\epsilon^{1/2-\beta}}{\sqrt{\rho}}\frac{e^{-i\theta(2N-2+\beta)}e^{-\rho/\epsilon}}{e^{2i\theta}+1}. \end{aligned} \tag{6.6.13}$$

Thus we obtain

$$\text{RHS} \sim 2\sqrt{2\pi}(-1)^N \frac{\epsilon^{1/2-\beta}}{\sqrt{\rho}} \frac{e^{-i\theta(2N-2+\beta)}e^{-\rho/\epsilon}}{e^{2i\theta}+1} \left[\cosh\left(\kappa\cos\psi e^{-i\theta}\right)\right.$$
$$\left. + \cosh\left(\kappa\sin\psi e^{-i\theta}\right) - 2\right] f_0 + \cdots, \tag{6.6.14}$$

and we see from the factor $e^{-\rho/\epsilon}$ that RHS is exponentially small.

We now seek a solution to the remainder equation (6.4.1), this time with the 'forcing due to truncation' replaced by RHS, in the same way as in Section 6.4. Writing $R_N = e^{\mp i\kappa z}S_N(Z)$ in (6.4.1), where κ is as usual a solution of (6.4.5) with $\Re(\kappa) > 0$, and Taylor expanding the differences in Z, we find

$$2i\epsilon\left[\cos\psi\sin(\kappa\cos\psi) + \sin\psi\sin(\kappa\sin\psi)\right]S_N' + \epsilon^2\left[\cos^2\psi\cos(\kappa\cos\psi)\right.$$
$$\left. + \sin^2\psi\cos(\kappa\sin\psi)\right]S_N'' - \epsilon^2 F_M'(u_0(Z))S_N + \cdots = e^{\pm i\kappa z}\text{RHS} + \cdots. \tag{6.6.15}$$

Note that on the left-hand side, the $\mathrm{O}(R_N)$ contribution vanishes because κ satisfies (6.4.5). The $\mathrm{O}(\epsilon R_N)$ terms on the left-hand side vanish if κ is real, in which case the leading-order contribution is $\mathrm{O}\left(\epsilon^2 R_N\right)$; otherwise it is $\mathrm{O}(\epsilon R_N)$.

Now,

$$\exp(\pm i\kappa z - \rho/\epsilon) = \exp\left[\pm i\kappa z_0 + \left(\pm i\kappa\zeta \pm i\rho e^{i\theta} - \rho\right)/\epsilon\right]. \tag{6.6.16}$$

Therefore we can see that, although it remains exponentially small on the real line, $e^{\pm i\kappa z}$RHS is maximal with respect to θ at $\theta = \mp\frac{\pi}{2}$. These values of θ define the Stokes lines, two emanating from each singularity, at which the main change in S_N will occur. As we are concerned with the behaviour of the solution for real z, the Stokes lines of importance are those which cross the real line. Focusing on those singularities in the upper half-plane, so that $\Im(\zeta) > 0$, the Stokes line of interest is $\theta = -\frac{\pi}{2}$. We therefore concentrate on solutions $R_N = e^{-i\kappa z}S_N$. Symmetry considerations then allow the contribution from the conjugate singularity at ζ^*, which is of the form $R_N = e^{+i\kappa z}S_N$ and is due to the Stokes line $\theta = \frac{\pi}{2}$ originating at that singularity, to be recovered simply by taking the complex conjugate.

In order to capture the effects of maximal forcing, we rescale θ in the vicinity of the Stokes line as $\theta = -\frac{\pi}{2} + \eta(\epsilon)\hat{\theta}$, where the scaling $\eta(\epsilon)$ is to be determined. This gives

$$\begin{aligned} e^{+i\kappa z}(-1)^N e^{-i\theta(2N-2+\beta)} e^{-\rho/\epsilon} \\ &\sim \exp\left[i\kappa z_0 + \frac{i}{\epsilon}\left(\rho e^{-i\pi/2+i\eta\hat{\theta}} + \kappa\zeta\right) + iN\pi - i\left(-\frac{\pi}{2} + \eta\hat{\theta}\right)(2N-2+\beta) - \frac{\rho}{\epsilon}\right] \\ &\sim \exp\left[i\kappa\left(z_0 + \frac{\zeta}{\epsilon}\right) + \frac{1}{\epsilon}\left(\rho + i\rho\eta\hat{\theta} - \frac{1}{2}\rho\eta^2\hat{\theta}^2\right) - i\eta\hat{\theta}\left(\frac{\rho}{\epsilon} + 2\nu\right)\right. \\ &\quad \left. + i(\beta-2)\left(\frac{\pi}{2} - \eta\hat{\theta}\right) - \frac{\rho}{\epsilon}\right] \\ &\sim -e^{i\beta\pi/2} e^{i\kappa(z_0+\zeta/\epsilon)} e^{-\rho\eta^2\hat{\theta}^2/(2\epsilon)}, \end{aligned} \tag{6.6.17}$$

which suggests the scaling $\eta = \sqrt{\epsilon}$. We therefore also have

$$\begin{aligned} \frac{\cosh\left(\kappa\cos\psi e^{-i\theta}\right) + \cosh\left(\kappa\sin\psi e^{-i\theta}\right)}{e^{2i\theta}+1} &\sim \kappa\left[\cos\psi\sin(\kappa\cos\psi) + \sin\psi\sin(\kappa\sin\psi)\right] \\ &\quad \times\left(-\frac{1}{2} + \frac{3i}{4}\sqrt{\epsilon}\hat{\theta}\right) + \kappa^2\left[\cos^2\psi\cos(\kappa\cos\psi) + \sin^2\psi\cos(\kappa\sin\psi)\right] + \cdots, \end{aligned} \tag{6.6.18}$$

where we have made use of the fact that κ satisfies (6.4.5) in order to eliminate terms; note that if κ is real the first contribution to the right-hand side also vanishes and the second is simply equal to κ^2. We shall now consider the two types of eigenvalue in turn, $\kappa \in \mathbb{R}$ and $\kappa \notin \mathbb{R}$, in order to elucidate precisely what contribution to the remainder each makes.

6.6.1 Contribution to R_N from $\kappa \in \mathbb{R}$

As discussed in Section 6.4, κ can be real and non-zero only if $\tan\psi \in \mathbb{Q}_\infty$, in which case we define $\tan\psi = m_2/m_1$ as in (6.4.6). This gives $\kappa = M(m_1^2+m_2^2)^{1/2}$ as in (6.4.7), with $M > 0$ due to our restriction that $\Re(\kappa) > 0$. Thus if κ is real then the leading-order balance in (6.6.15) is

$$\epsilon^2 S_N''(Z) - \epsilon^2 F_M'(u_0(Z))S_N(Z) = -i\sqrt{\pi/2}e^{i\beta\pi/2}\frac{\epsilon^{1-\beta}}{\sqrt{\rho}}e^{i\kappa(z_0+\zeta/\epsilon)}\kappa^2 f_0(Z)\hat{\theta}e^{-\rho\hat{\theta}^2/2} + \cdots, \tag{6.6.19}$$

where f_0 is equal to one of $\lambda_{M,\psi}g(Z)$ or $\Lambda_{M,\psi}G(Z;\zeta)$, which give β equal to -1 or $2\gamma+2$ respectively. Writing

$$S_N(Z) = \epsilon^{-\beta}e^{i\kappa(z_0+\zeta/\epsilon)}f_0(Z)\hat{S}_N(\hat{\theta}), \tag{6.6.20}$$

we have

$$\epsilon^2 S_N''(Z) = \epsilon^{1-\beta}e^{i\kappa(z_0+\zeta/\epsilon)}f_0(Z)\frac{\kappa^2}{\rho^2}\frac{\mathrm{d}^2\hat{S}_N}{\mathrm{d}\hat{\theta}^2} + \mathrm{O}\left(\epsilon^{3/2-\beta}e^{i\kappa(z_0+\zeta/\epsilon)}\right). \tag{6.6.21}$$

Thus

$$\frac{\mathrm{d}^2\hat{S}_N}{\mathrm{d}\hat{\theta}^2} \sim -i\sqrt{\pi/2}e^{i\beta\pi/2}\rho^{3/2}\hat{\theta}e^{-\rho\hat{\theta}^2/2} + \cdots. \tag{6.6.22}$$

Imposing the boundary condition $\hat{S}_N \to 0$ as $\hat{\theta} \to -\infty$, this has leading-order solution

$$\hat{S}_N(\hat{\theta}) \sim \frac{i\pi}{2}e^{i\beta\pi/2}\mathrm{erfc}\left(-\hat{\theta}\sqrt{\frac{\rho}{2}}\right), \tag{6.6.23}$$

where $\mathrm{erfc}\,(t)$ is the complementary error function

$$\mathrm{erfc}\,(t) := \frac{2}{\sqrt{\pi}}\int_t^\infty e^{-s^2}\mathrm{d}s. \tag{6.6.24}$$

Therefore the exponentially small terms

$$R_N \sim \sum_{M=1}^{\infty} i\pi e^{i\beta\pi/2}\epsilon^{-\beta}e^{2M\pi\sqrt{m_1^2+m_2^2}i(z_0+\zeta/\epsilon)}e^{-i\kappa z}f_0(Z), \tag{6.6.25}$$

for each singularity ζ in the upper half-plane, are present to the right of the Stokes layer. By symmetry, the contribution from the conjugate singularity at $Z = \zeta^*$ is simply the complex conjugate of (6.6.25). Note that here $e^{-i\kappa z} = 1$ on lattice points, as $\tan\phi \in \mathbb{Q}_\infty$ for real κ.

6.6.2 Contribution to R_N from $\kappa \notin \mathbb{R}$

We now consider the forcing of the remainder equation (6.6.15) due to those eigenvalues with $\Im(\kappa) \neq 0$ (recall that we have set $\Re(\kappa) > 0$). We know that for such κ

$$\cos\psi\sin(\kappa\cos\psi) + \sin\psi\sin(\kappa\sin\psi) \neq 0, \tag{6.6.26}$$

(see Section 6.4) and so the leading order balance in (6.6.15) is

$$2\epsilon i S_N'(Z) = \sqrt{2\pi} e^{i\beta\pi/2} \frac{\epsilon^{1/2-\beta}}{\sqrt{\rho}} e^{i\kappa(z_0+\zeta/\epsilon)} e^{-\rho\hat{\theta}^2/2} f_0 + \cdots, \tag{6.6.27}$$

where $f_0 = \Omega_{\kappa,\psi}$, a constant, and $\beta = \gamma$. Writing

$$S_N(Z) = \epsilon^{-\beta} e^{i\kappa(z_0+\zeta/\epsilon)} f_0 \hat{S}_N(\hat{\theta}), \tag{6.6.28}$$

we have

$$\epsilon S_N'(Z) = \epsilon^{1/2-\beta} e^{i\kappa(z_0+\zeta/\epsilon)} f_0 \frac{\kappa}{\rho} \frac{\mathrm{d}\hat{S}_N}{\mathrm{d}\hat{\theta}} + \mathrm{O}\left(\epsilon^{1-\beta} e^{i\kappa(z_0+\zeta/\epsilon)}\right). \tag{6.6.29}$$

Thus

$$\frac{\mathrm{d}\hat{S}_N}{\mathrm{d}\hat{\theta}} \sim -i\sqrt{\pi/2} e^{i\beta\pi/2} \sqrt{\rho} e^{-\rho\hat{\theta}^2/2} + \cdots. \tag{6.6.30}$$

Since $R_N = e^{-i\kappa z} S_N$ and $\Re(\kappa) \neq 0$, for $\Im(\pm\kappa) > 0$ we have $R_N \to 0$ as $z \to \pm\infty$. Although these contributions to the remainder are bounded in the pertinent limit, in the opposite limit we have $e^{i\kappa z} \to \infty$ as $z \to \mp\infty$ for $\Im(\pm\kappa) > 0$. However, the resultant unbounded growth may be prevented by choosing the constant of integration when integrating (6.6.30) appropriately. Doing this, we have

$$\hat{S}_N(\hat{\theta}) \sim \begin{cases} \frac{i\pi}{2} e^{i\beta\pi/2} \mathrm{erfc}\left(\hat{\theta}\sqrt{\frac{\rho}{2}}\right), & \Im(\kappa) > 0, \\ -\frac{i\pi}{2} e^{i\beta\pi/2} \mathrm{erfc}\left(-\hat{\theta}\sqrt{\frac{\rho}{2}}\right), & \Im(\kappa) < 0. \end{cases} \tag{6.6.31}$$

Therefore the exponentially small terms

$$R_N \sim \sum_{\substack{\Re(\kappa)>0, \\ \Im(\kappa)>0}} i\pi e^{i\beta\pi/2} \epsilon^{-\beta} e^{i\kappa(z_0+\zeta/\epsilon)} e^{-i\kappa z} f_0, \tag{6.6.32}$$

are present to the left of the Stokes layer, and the exponentially small terms

$$R_N \sim \sum_{\substack{\Re(\kappa)>0, \\ \Im(\kappa)<0}} -i\pi e^{i\beta\pi/2} \epsilon^{-\beta} e^{i\kappa(z_0+\zeta/\epsilon)} e^{-i\kappa z} f_0, \tag{6.6.33}$$

to the right, for each singularity ζ in the upper half-plane. By symmetry, the contributions from the conjugate singularity at $Z = \zeta^*$ are the complex conjugates of (6.6.32) and (6.6.33). Note that, due to our selection of the constants of integration, the Stokes lines relevant to complex κ do not switch on any exponentially growing terms as they

are crossed. Thus contributions from $\kappa \notin \mathbb{R}$ remain exponentially small in the far-fields and play no role in determining the leading-order solution. We are therefore free to neglect such contributions when discussing leading-order behaviour, and shall do so henceforth.

6.7 The width of the snaking region

Although we have ensured that complex κ do not produce any unbounded terms in the remainder, there are still exponentially growing contributions from real κ which we have yet to deal with. Because $G(Z;\zeta)$ has zero coefficient to the left of the Stokes lines and the particular integral $P(Z)$ is bounded as $Z \to -\infty$ (see (6.4.19)), the remainder is bounded in this limit. On the other hand, G has non-zero coefficient to the right of the Stokes lines, and both G and P experience exponential growth as $Z \to \infty$. We must eliminate these unbounded terms if the asymptotic expansion is to remain uniform. Note that we shall now evaluate our solution on the lattice points, and so $e^{-i\kappa z} \equiv 1$ in (6.6.25), as $\tan\phi \in \mathbb{Q}_\infty$ for real κ.

G and P are given in the far-field by (6.4.18) and (6.4.19), respectively. In light of (6.6.25), the dominant terms which are switched on are given by those singularities closest to, and equidistant from, the real line, with $M = 1$. For the sake of simplicity, we shall assume henceforth that there are only two such singularities. In this instance, focusing on the exponentially growing complementary function G, the leading order contribution which is switched on as the Stokes lines are crossed is

$$\sim -i\pi e^{i\gamma\pi}\epsilon^{-2\gamma-2}e^{2\pi\sqrt{m_1^2+m_2^2}i(z_0+\zeta/\epsilon)}\Lambda_{1,\psi}G(Z;\zeta) + \text{c.c.}, \tag{6.7.1}$$

where we have written $\kappa = 2M\pi(m_1^2+m_2^2)^{1/2}$ with $M = 1$. Note that, as we are focusing solely on $f_0 = \Lambda_{1,\psi}G$, we have $\beta = 2\gamma + 2$. Including the particular integral $P(Z)$ due to the forcing $\epsilon^2\delta r F_{r,M}(u_0)$ in (6.4.1), the remainder in the far-field $Z \to \infty$ is

therefore

$$R_N \sim \left\{ \frac{\pi|\Lambda_{1,\psi}|e^{-2\pi\sqrt{m_1^2+m_2^2}\Im(\zeta)/\epsilon}}{\epsilon^{2\gamma+2}\alpha_+^2 D_+} \cos\left[2\pi z_0\sqrt{m_1^2+m_2^2}+\chi\right] + \frac{\delta r\int_{u_-}^{u_+} F_{r,M}(v)\mathrm{d}v}{2\alpha_+^2 D_+} \right\} e^{\alpha_+ Z}, \tag{6.7.2}$$

where

$$\chi = -\frac{\pi}{2} + \gamma\pi + \frac{2\pi}{\epsilon}\Re(\zeta)\sqrt{m_1^2+m_2^2} + \mathrm{Arg}\left(\Lambda_{1,\psi}\right). \tag{6.7.3}$$

For the expansion to remain uniform as $Z \to \infty$, we require the coefficient of these unbounded terms to be zero. This is true if

$$\delta r = -\frac{2\pi|\Lambda_{1,\psi}|e^{-2\pi\sqrt{m_1^2+m_2^2}\Im(\zeta)/\epsilon}}{\epsilon^{2\gamma+2}\int_{u_-}^{u_+} F_{r,M}(v)\mathrm{d}v} \cos\left[2\pi z_0\sqrt{m_1^2+m_2^2}+\chi\right], \tag{6.7.4}$$

thus fixing the origin of the front z_0 to be one of two values modulo $(m_1^2+m_2^2)^{-1/2}$. Furthermore, real solutions exist only if

$$|\delta r| \leq \frac{2\pi|\Lambda_{1,\psi}|e^{-2\pi\sqrt{m_1^2+m_2^2}\Im(\zeta)/\epsilon}}{\epsilon^{2\gamma+2}|\int_{u_-}^{u_+} F_{r,M}(v)\mathrm{d}v|}; \tag{6.7.5}$$

thus stationary fronts only exist for δr within this (exponentially small) region. As localised solutions are constructed from back-to-back stationary fronts, (6.7.5) provides a formula for the width of the snaking region. Note the constant $\Lambda_{1,\psi}$ is at present undetermined; in fact, it cannot be determined analytically due to the linear nature of the large-n equation (6.5.2). However, the leading-order contribution to (6.5.2) as $Z \to \zeta$ yields a recurrence relation which can in principle be used to obtain a good approximation to $\Lambda_{1,\psi}$, in a similar manner to the method used Section 4.4 for the cubic-quintic SHE. This must be done on a case-by-case basis for each choice of the nonlinearity $F(u;r)$, and so we defer further discussion of the calculation of $\Lambda_{1,\psi}$ to the next chapter, in which we shall consider two specific examples.

6.8 The snakes-and-ladders bifurcation equations

Armed with the full asymptotic expansion for a stationary front, including exponentially gorwing terms in the remainder, we are now able to construct localised solutions,

or spatially homoclinic connections to the constant solution u_- via u_+, by means of matching two stationary fronts back-to-back. Such a solution consists of an up-front $u(\epsilon z - \epsilon z_0)$ matched to a distant down-front $u(-\epsilon z + \epsilon z_0 + L/\epsilon)$, where $L > 0$ is an $\mathrm{O}(1)$ constant. Note that the down-front is produced by applying the rotation $(\psi, z_0) \to (\psi + \pi, -z_0)$ to $u(Z)$, followed by the translation $\epsilon z_0 \to \epsilon z_0 + L/\epsilon$. Therefore the origin of the up-front is at $z = z_0$, as before, whereas the translation of the down-front to the right shifts its origin to $-z = -z_0 - L/\epsilon^2$. The scaling of the front separation L/ϵ is motivated by the fact that the exponentially growing contribution to the remainder (6.7.2) is no longer exponentially small when $Z = \mathrm{O}(1/\epsilon)$ and is positive. This allows us to observe the interplay between three exponentially small effects: the locking of fronts to the lattice, the deviation from the Maxwell point and the front matching error. The first two are responsible for the existence of the snaking region, as already shown in Section 6.7; we shall see now that the third is responsible for the way the solution curves are skewed to the right of the snaking region when the localised patch is small enough.

From the far-field expansions (6.4.15) and (6.7.2), we see that an up-front $u \sim u_0 + \cdots + R_N$ is given by

$$u \sim u_+ - D_+ e^{-\alpha_+ Z} + \left\{ \frac{\pi |\Lambda_{1,\psi}| e^{-2\pi \sqrt{m_1^2+m_2^2}\,\Im(\zeta)/\epsilon}}{\epsilon^{2\gamma+2}\alpha_+^2 D_+} \cos\left[2\pi z_0 \sqrt{m_1^2+m_2^2} + \chi\right] + \frac{\delta r \int_{u_-}^{u_+} F_{r,M}(v)\mathrm{d}v}{2\alpha_+^2 D_+} \right\} e^{\alpha_+ Z} \tag{6.8.1}$$

as $Z \to \infty$. By symmetry, the down-front is given within the matching region by (6.8.1) under the combined rotation and translation $(\psi, z_0) \to (\psi + \pi, -z_0 - L/\epsilon^2)$. Thus $Z \to -Z + L/\epsilon$ and we have

$$u \sim u_+ - D_+ e^{-\alpha_+(-Z+L/\epsilon)} + \left\{ \frac{\pi |\Lambda_{1,\psi}| e^{-2\pi \sqrt{m_1^2+m_2^2}\,\Im(\zeta)/\epsilon}}{\epsilon^{2\gamma+2}\alpha_+^2 D_+} \times \cos\left[2\pi\left(-z_0 - \frac{L}{\epsilon^2}\right)\sqrt{m_1^2+m_2^2} + \chi\right] + \frac{\delta r \int_{u_-}^{u_+} F_{r,M}(v)\mathrm{d}v}{2\alpha_+^2 D_+} \right\} e^{\alpha_+(-Z+L/\epsilon)} \tag{6.8.2}$$

as $(-Z + L/\epsilon) \to \infty$. Note that we have not yet eliminated exponentially growing terms; these are necessary in order to match with exponentially growing and decaying terms between fronts. Unbounded terms are then removed by adding the up-front and down-front together and subtracting matched parts, following the usual method of matched asymptotic expansions.

Matching growing and decaying exponential terms in the matching region, we obtain

$$-D_+ e^{-\alpha_+ L/\epsilon} = \frac{\pi|\Lambda_{1,\psi}|e^{-2\pi\sqrt{m_1^2+m_2^2}\Im(\zeta)/\epsilon}}{\epsilon^{2\gamma+2}\alpha_+^2 D_+}\cos\left[2\pi z_0\sqrt{m_1^2+m_2^2}+\chi\right] + \frac{\delta r\int_{u_-}^{u_+}F_{r,M}(v)\mathrm{d}v}{2\alpha_+^2 D_+}, \tag{6.8.3}$$

$$-D_+ e^{-\alpha_+ L/\epsilon} = \frac{\pi|\Lambda_{1,\psi}|e^{-2\pi\sqrt{m_1^2+m_2^2}\Im(\zeta)/\epsilon}}{\epsilon^{2\gamma+2}\alpha_+^2 D_+}\cos\left[-2\pi\left(z_0+\frac{L}{\epsilon^2}\right)\sqrt{m_1^2+m_2^2}+\chi\right] + \frac{\delta r\int_{u_-}^{u_+}F_{r,M}(v)\mathrm{d}v}{2\alpha_+^2 D_+}. \tag{6.8.4}$$

We therefore have

$$\cos\left[2\pi z_0\sqrt{m_1^2+m_2^2}+\chi\right] = \cos\left[-2\pi\left(z_0+\frac{L}{\epsilon^2}\right)\sqrt{m_1^2+m_2^2}+\chi\right], \tag{6.8.5}$$

providing the requisite detail from which to derive the snaking bifurcation equations. There are two cases to consider, firstly

$$z_0 = -\frac{L}{2\epsilon^2} + \frac{k}{2\sqrt{m_1^2+m_2^2}}, \tag{6.8.6}$$

and secondly

$$\frac{L}{\epsilon} = \left(\frac{\chi}{\pi}+k\right)\frac{\epsilon}{\sqrt{m_1^2+m_2^2}}, \tag{6.8.7}$$

where k is some integer.

6.8.1 The snakes

Suppose first that (6.8.6) holds. Substituting for z_0 in (6.8.3) and rearranging, we gain the bifurcation equation

$$\delta r = -\frac{2}{\int_{u_-}^{u_+} F_{r,M}(v)\mathrm{d}v}\left\{\frac{\pi|\Lambda_{1,\psi}|}{\epsilon^{2\gamma+2}}e^{-2\pi\sqrt{m_1^2+m_2^2}\Im(\zeta)/\epsilon}\cos\left[-\frac{\pi L}{\epsilon^2}\sqrt{m_1^2+m_2^2}-k\pi+\chi\right]\right.$$
$$\left.+\,\alpha_+^2 D_+^2 e^{-\alpha_+ L/\epsilon}\right\}, \tag{6.8.8}$$

from which the front separation L may be determined. As (6.8.8) is periodic in k with period 2, only the parity of k is of importance when determining L; thus (6.8.8) describes two distinct snaking solution curves with phases that differ by π. Each solution is unique up to translations in $Z = \epsilon(z - z_0)$ by integer multiples of the effective lattice spacing $\epsilon(m_1^2 + m_2^2)^{-1/2}$. Furthermore, inspection of (6.8.6) indicates that the localised solution is site-centred if k is even and bond-centred if k is odd. The second term on the right-hand side of (6.8.8), corresponding to the front matching error, skews the solution curves to the right for small enough L. However, as L increases this term rapidly becomes negligible, in which case the snaking curves are confined to the same exponentially small parameter range defined in (6.7.5)—the snaking region. L is free to increase without bound, producing an infinite multiplicity of localised solutions within this range.

6.8.2 The ladders

Now suppose that (6.8.7) holds. Since k is arbitrary, in this case the front separation L/ϵ may take one of a discrete set of values, provided the constraints $L > 0$ and $k = \mathrm{O}\left(1/\epsilon^2\right)$ (as $L = \mathrm{O}\left(1\right)$) are satisfied. The origin z_0 of the up-front may then be found

by solving (6.8.3), rewritten here as

$$\delta r = -\frac{2}{\int_{u_-}^{u_+} F_{r,M}(v)\mathrm{d}v}\left\{\frac{\pi|\Lambda_{1,\psi}|}{\epsilon^{2\gamma+2}}e^{-2\pi\sqrt{m_1^2+m_2^2}\Im(\zeta)/\epsilon}\cos\left[2\pi z_0\sqrt{m_1^2+m_2^2}+\chi\right]\right.$$
$$\left.+\,\alpha_+^2 D_+^2 e^{-\alpha_+ L/\epsilon}\right\}. \tag{6.8.9}$$

This equation therefore describes the rungs of the snakes-and-ladders bifurcation diagram. Each k corresponds to a single rung, which may be parameterised by z_0 in the range $[0,(m_1^2+m_2^2)^{-1/2})$. The deviation δr from the Maxwell point for each z_0 is then provided by (6.8.9), which has solutions in the same range of values of δr as (6.8.8), as expected. Furthermore, each rung in fact represents two solution curves, corresponding to the two solutions of (6.8.9) in the range $z_0 \in [0,(m_1^2+m_2^2)^{-1/2})$. These two solutions coincide at the maximum and minimum of the cosine, representing the bifurcation points at which the rungs meet the snakes. Note that each rung originates on one snake at $z_0 = 0$ and terminates on the other at $z_0 = (m_1^2+m_2^2)^{-1/2}/2$, linking the two snaking solution curves.

Thus we have derived a set of formulae describing the snakes-and-ladders bifurcation diagram for one-dimensional solutions to the general differential-difference (6.0.3). The width of the snaking region is given by (6.7.5) if $\tan\psi \in \mathbb{Q}_\infty$, and is zero if not. In the next chapter we shall apply these results to the two specific examples shown in figures 6.1 and 6.3, and compare the asymptotic prediction with numerical computations. In particular, we shall discuss the calculation of the as yet undetermined constant $\Lambda_{1,\psi}$.

CHAPTER 7

Specific examples of discrete snaking: numerical verification of asymptotic results

In Chapter 6 we used the method of exponential asymptotics to analyse homoclinic snaking of solutions to

$$\frac{\partial u}{\partial t} = \Delta u - \epsilon^2 F(u; r) \tag{7.0.1}$$

which are localised in one spatial direction only, where Δu is the nearest-neighbour stencil (6.0.2), $0 < \epsilon \ll 1$ and $F(u; r)$ is some bistable nonlinearity incorporating a bifurcation parameter r. We found that when the tangent of the angle of orientation ψ of these solutions is irrational then the snaking width is zero; otherwise, it is exponentially small and the snakes-and-ladders bifurcation diagram is described by the formulae (6.8.8)-(6.8.9). In the present chapter we shall apply these general results to two specific choices of F. We shall focus exclusively on angles with non-zero snaking width, and so henceforth set

$$\begin{aligned} \cos\psi = \frac{m_1}{\sqrt{m_1^2 + m_2^2}}, \qquad \sin\psi = \frac{m_2}{\sqrt{m_1^2 + m_2^2}}, \\ (m_1, m_2) \in \mathbb{Z}^2 \backslash \{(0,0)\}, \qquad \gcd(|m_1|, |m_2|) = 1; \end{aligned} \tag{7.0.2}$$

see Sections 6.1 and 6.4 for further details. In particular, for both examples we shall calculate the analytically undeterminable constants $\Lambda_{1,\psi}$ appearing in (6.8.8)-(6.8.9) for $\psi = \frac{k\pi}{4}$, $k \in \{0, 1, \ldots, 7\}$, and discuss why their calculation is more difficult for other values of ψ.

7.1 Example: a cubic nonlinearity with constant forcing

Our first example is (7.0.1) with a cubic nonlinearity and constant forcing, given by

$$\frac{\partial \hat{u}}{\partial t} = \Delta \hat{u} + \hat{r} + \hat{s}\hat{u} - \hat{u}^3, \tag{7.1.1}$$

fixing $\hat{s} > 0$ in order to ensure bistability. Note this is not yet of the same form as (7.0.1); a rescaling is required to describe dynamics close to bifurcation. Defining

$$\hat{u} = \epsilon u, \qquad \hat{r} = \epsilon^3 r, \qquad \hat{s} = \epsilon^2 s, \tag{7.1.2}$$

substituting into (7.1.1) and dividing by ϵ, we have

$$\frac{\partial u}{\partial t} = \Delta u - \epsilon^2 \left(-r - su + u^3\right); \tag{7.1.3}$$

this is now equivalent to (7.0.1) with $F(u; r) = -r - su + u^3$. (7.1.3) is probably the simplest form of (7.0.1) which exhibits snaking behaviour. The bifurcation diagram and example solutions for (7.1.1) with $\psi = 0$ can be seen in figures 6.3 and 6.4; unhatted variables in those figures correspond to hatted ones in (7.1.1). The two constant, stable solutions (which are both non-zero) are connected via an unstable branch, thus forming an S-shaped solution curve in parameter space. This results in a region of bistability, in turn containing the snaking region. We note that a similar system with this nonlinearity was studied in [27], in which discreteness was incorporated by allowing a coefficient in a partial differential equation to vary periodically in space, rather than through a difference operator as is the case here. However, that work presents an incomplete description of the snaking phenomenon, due to its failure to incorporate exponentially small terms.

In order to apply the results of Chapter 6, we must first derive a one-dimensional, stationary front from which localised solutions may be constructed. To this end, we define Z as in (6.2.3), set $u \equiv u(Z)$ in (7.1.3) and impose the boundary conditions $u_\pm$ as $Z \to \pm\infty$. Taylor expanding as in Section 6.3, the leading-order continuum approximation is

$$0 = \frac{\mathrm{d}^2 u_0}{\mathrm{d}Z^2} + r + s u_0 - u_0^3. \tag{7.1.4}$$

This can be integrated once after multiplication by u_0', yielding

$$0 = \frac{1}{2}\left(\frac{\mathrm{d}u_0}{\mathrm{d}Z}\right)^2 + r u_0 + \frac{1}{2} s u_0^2 - \frac{1}{4} u_0^4 - \left(r u_- + \frac{1}{2} s u_-^2 - \frac{1}{4} u_-^4\right), \tag{7.1.5}$$

where the constant of integration has been chosen to ensure that $u_0 \equiv u_-$ is a solution of (7.1.5). Requiring that the far-fields of the front satisfy both (7.1.4) and (7.1.5), we find that $u_\pm$ and the Maxwell point $r = r_M$ are given by the algebraic system

$$\begin{aligned} 0 &= r_M + s u_+ - u_+^3, \\ 0 &= r_M + s u_- - u_-^3, \\ 0 &= r_M u_+ + \frac{1}{2} s u_+^2 - \frac{1}{4} u_+^4 - \left(r_M u_- + \frac{1}{2} s u_-^2 - \frac{1}{4} u_-^4\right) \end{aligned} \tag{7.1.6}$$

(see the discussion around (6.3.6)). This can readily be solved to give

$$u_\pm = \pm\sqrt{s}, \qquad r_M = 0; \tag{7.1.7}$$

in consequence (7.1.5) becomes

$$2\left(\frac{\mathrm{d}u_0}{\mathrm{d}Z}\right)^2 = \left(s - u_0^2\right)^2. \tag{7.1.8}$$

This is easily integrated, providing the leading-order front

$$u_0 = \sqrt{s}\tanh\left(\sqrt{\frac{s}{2}} Z\right), \tag{7.1.9}$$

where the sign of the square root has been chosen so that $u_+ > u_-$; the front of opposite orientation can be obtained by exploiting the reversibility of (7.1.1).

We now need to evaluate the various constants appearing in the bifurcation equations (6.8.8)-(6.8.9). From (7.1.9), we see that the singularities ζ of u_0 are

$$\zeta = \zeta_m = \sqrt{\frac{1}{2s}}(2m+1)\pi i \tag{7.1.10}$$

each of which has strength $\gamma = 1$. Thus (6.7.3) yields $\chi = \frac{\pi}{2} + \text{Arg}\left(\Lambda_{1,\psi}\right)$. The dominant singularities are those nearest (and equidistant from) the real line, namely ζ_0 and $\zeta_{-1} = \zeta_0^*$. In addition, because

$$u_0 \sim \sqrt{s}\left(1 - 2e^{-\sqrt{2s}Z}\right) \tag{7.1.11}$$

as $Z \to \infty$ and $F_{r,M}(u) \equiv -1$ we have

$$\alpha_+ = \sqrt{2s}, \qquad D_+ = 2\sqrt{s}, \qquad \int_{u_-}^{u_+} F_{r,M}(v)\mathrm{d}v = -2\sqrt{s}. \tag{7.1.12}$$

Note that, although α_+ is defined by (6.4.16), it is simpler in practice to simply read it off from the leading-order exponential in the far-field. Hence we may now write down the bifurcation equations (6.8.8)-(6.8.9) in terms of the parameters of the scaled equation (7.1.3). For the sake of brevity, we shall not write these out in full, and instead content ourselves with the width of the snaking region. From (6.7.5), we find that this is

$$|\delta r| \leq \frac{\pi|\Lambda_{1,\psi}|e^{-\pi^2\sqrt{2(m_1^2+m_2^2)}/\epsilon\sqrt{s}}}{\epsilon^4\sqrt{s}}. \tag{7.1.13}$$

It is instructive to write this in terms of the original, hatted variables appearing in (7.1.1), in which case $\hat{s}$ provides the small variable. Thus we obtain the unscaled snaking width as

$$|\hat{r}| \leq \frac{\pi|\Lambda_{1,\psi}|e^{-\pi^2\sqrt{2(m_1^2+m_2^2)/\hat{s}}}}{\sqrt{\hat{s}}}, \tag{7.1.14}$$

since the Maxwell point in this case is zero. However, we are not yet able to compare our analytical results with numerical computations, as $\Lambda_{1,\psi}$ remains undetermined. We turn our attention to its evaluation now.

7.1.1 Finding $\Lambda_{1,\psi}$

All that remains for a comprehensive comparison between numerical computations of (7.1.1) and our analytical predictions is the evaluation of the constants $\Lambda_{1,\psi}$. Unfortunately, this cannot be done analytically due to the linear nature of the large-n equation (6.5.2). However, it may be calculated directly through the iteration of a certain recurrence relation arising from the behaviour of the solution near the singularity ζ_m.

As the singularity in the leading order front u_0 (7.1.9) has strength $\gamma = 1$, we have (see the discussion around (6.5.12)-(6.5.16))

$$u_n \sim \frac{U_n}{(Z-\zeta_m)^{2n+1}}, \tag{7.1.15}$$

as $Z \to \zeta_m$, for some sequence of constants U_n. Upon substitution of this ansatz into the steady version of (7.1.3), Taylor expanding the slow differences, equating powers of ϵ and taking the leading-order terms in $(Z-\zeta_m)^{-1}$ leads to

$$0 = 2\sum_{p=1}^{n+1} \frac{\cos^{2p}\psi + \sin^{2p}\psi}{(2p)!} \frac{\Gamma(2n+3)}{\Gamma(2n-2p+3)} U_{n-p+1} - \sum_{p_1=0}^{n} \sum_{p_2=0}^{n-p_1} U_{p_1} U_{p_2} U_{n-p_1-p_2}. \tag{7.1.16}$$

Iteration of this recurrence relation therefore yields the sequence U_n. In principle, we may then compare (7.1.15) for large n with the analytical formula for u_n (6.5.17) in order to find $\Lambda_{1,\psi}$.

There are three types of contribution to (6.5.17), two arising from real and one from complex eigenvalues (where each eigenvalue κ is a solution of (6.4.5)). The real eigenvalues are characterised by the integers M, and it is clear that the dominant one is given by $M = 1$. Furthermore, the term involving $G(Z;\zeta_m)$ dominates the one involving $g(Z)$ (see the discussion after (6.5.17)). As we are not in general able to determine complex eigenvalues analytically, we shall for now merely denote by K the eigenvalue $\kappa \notin \mathbb{R}$ of smallest modulus in the quadrant $\Re(K) > 0$, $\Im(K) > 0$. Recall that we set $\Re(\kappa) > 0$ without loss of generality in Section 6.5. Hence there is only one other complex eigenvalue with modulus equal to that of K, and this is simply K^*, as solutions of (6.4.5)

occur in complex conjugate pairs. Therefore, taking only the dominant contribution to (6.5.17) from real κ and the dominant contribution from complex κ, we have

$$u_n(Z) \sim \frac{(-1)^n\Gamma(2n+4)\Lambda_{1,\psi}G(Z;\zeta_m)}{\left[2\pi\sqrt{m_1^2+m_2^2}(Z-\zeta_m)\right]^{2n+4}} + \frac{(-1)^n\Gamma(2n+1)}{(Z-\zeta_m)^{2n+1}}\left(\frac{\Omega_{K,\psi}}{K^{2n+1}} + \frac{\Omega_{K^*,\psi}}{K^{*2n+1}}\right). \tag{7.1.17}$$

Note that (7.1.17) is not meant to represent a two-term asymptotic series, as there may be many more terms in (6.5.17) which are much smaller than one of those on the right-hand side of (7.1.17), but much larger than the other. Now, from (7.2.9) we have

$$u_0 \sim \frac{\sqrt{2}}{Z-\zeta_m} \tag{7.1.18}$$

as $Z \to \zeta_m$; thus $U_0 = \sqrt{2}$, and

$$G(Z;\zeta_m) \sim -\frac{1}{8}\sqrt{2}\,(Z-\zeta_m)^3 \tag{7.1.19}$$

in the same limit. Because U_0 is real, inspection of (7.1.16) indicates that U_n is real for all n; hence $\Omega_{K^*,\psi} = \Omega^*_{K,\psi}$. Comparing (7.1.17) with (7.1.18), the dominant contributions to U_n from real and complex κ are

$$U_n \sim \frac{(-1)^{n+1}\sqrt{2}\Gamma(2n+4)\Lambda_{1,\psi}}{8\left(2\pi\sqrt{m_1^2+m_2^2}\right)^{2n+4}} + \frac{2(-1)^n\Gamma(2n+1)|\Omega_{K,\psi}|}{|K|^{2n+1}} \times \cos\left[\mathrm{Arg}\left(\Omega_{K,\psi}\right) - (2n+1)\,\mathrm{Arg}\,(K)\right] \tag{7.1.20}$$

as $n \to \infty$. As discussed after (6.5.17), if $|K| < 2\pi(m_1^2+m_2^2)^{1/2}$ then the second term dominates; otherwise, the first does. Immediately we see a difficulty in obtaining $\Lambda_{1,\psi}$. If the second term is dominant, rearranging (7.1.20) provides an expression for $\Omega_{K,\psi}$; we require $\Lambda_{1,\psi}$. To obtain $\Lambda_{1,\psi}$ in this way, the first term must be the dominant one.

Unfortunately, it seems that if (6.4.5) admits complex solutions, then $|K| < 2\pi(m_1^2 + m_2^2)^{1/2}$ no matter the choice of m_1, m_2. Although we are unable to prove this rigorously, two strands of investigation provide evidence that this is indeed the case. First, in the limit $m_2 \ll m_1$, complex solutions to (6.4.5) of smallest modulus are $\kappa \sim 2\pi(1 + im_2/m_1)$, which have modulus much less than $2\pi(m_1^2+m_2^2)^{1/2}$. Second,

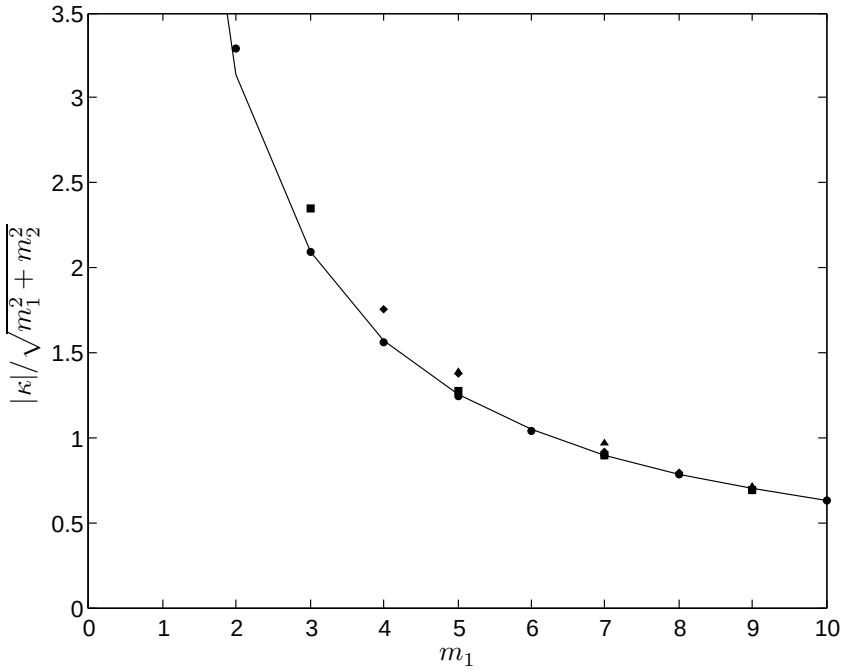

Figure 7.1: *Complex solutions to (6.4.5) of smallest modulus, for various values of m_1, m_2, scaled by $(m_1^2+m_2^2)^{1/2}$. Circles represent $m_2 = 1$, squares $m_2 = 2$, diamonds $m_2 = 3$ and triangles $m_2 = 4$; recall we have set $\gcd(|m_1|,|m_2|) = 1$. Although the data points are in many cases difficult to distinguish from one another on this scale, the salient detail, that each eigenvalue has modulus less than $2\pi(m_1^2+m_2^2)^{1/2}$, is clear. The solid line represents the asymptotic approximation of complex soltuions to (6.4.5) with smallest modulus, $\kappa \sim 2\pi(1+im_2/m_1)$, valid for $m_2 \ll m_1$.*

solving (6.4.5) numerically for various choices of m_1, m_2 has not produced a counter-example, and furthermore suggests that the aymptotic formula for κ is a good approximation even for moderate values of m_2/m_1, as shown in figure 7.1. Thus it would appear that we cannot calculate $\Lambda_{1,\psi}$ using the above method if (6.4.5) admits complex solutions. Furthermore, as the eigenvalues κ are independent of the choice of $F(u;r)$, this is so for all problems of the form (7.0.1).

There are, however, special cases with no complex eigenvalues at all; the axial and diagonal alignments $\psi = \frac{k\pi}{4}$, $k \in \{0,1,\ldots,7\}$. For such alignments (7.1.20) contains

only the term in which $\Lambda_{1,\psi}$ appears. Rearranging, we therefore see that in such a case

$$\Lambda_{1,\psi} \sim \lim_{n\to\infty} \frac{(12)^{1/4}(-1)^{n+1}\left(2\pi\sqrt{m_1^2+m_2^2}\right)^{2n+4}}{\Gamma(2n+4)} U_n, \tag{7.1.21}$$

yielding a good approximation for $\Lambda_{1,\psi}$ if U_n can be calculated for large enough n. Now, (7.1.16) must in general be iterated separately for each ψ. However, as (7.0.1) is invariant under rotations $\psi \to \psi + \frac{\pi}{2}$, it suffices to iterate (7.1.16) only for $\psi = 0$ and $\psi = \frac{\pi}{4}$, as the other six alignments can be recovered using said invariance. Doing so, we calculate $\Lambda_{1,0} \approx -2535$ and $\Lambda_{1,\pi/4} \approx -10141$. Thus we may carry out a quantitative comparison between the analytical formula (7.2.15) and numerical computations for these values of ψ. We note that inspection of the ratio $\Lambda_{1,\pi/4}/\Lambda_{1,0} \approx 4$ and the equivalent ratio in the next example suggests the simple relationship $\Lambda_{1,\psi} = \Lambda_{1,e}(m_1^2+m_2^2)^{1+\gamma}$; however, this is found to drastically underestimate the width of the snaking region for $\psi \neq \frac{k\pi}{4}$, $k \in \{0,1,\ldots,7\}$.

7.1.2 Comparison of analytical and numerical results

We have solved the one-dimensional, steady version of (7.1.1) for $\psi = 0, \frac{\pi}{4}$ numerically, using pseudo-arclength continuation to compute the bifurcation diagram. The domain size is chosen to be large enough that boundary effects have negligible effect on the width of the snaking region. In order to preserve this independence, the domain must be increased as $\hat{s} = \epsilon s$ decreases to counterbalance the spreading out of fronts; for example, we used three hundred points for $\hat{s} = 1$, but seven hundred for $\hat{s} = 0.2$. We imposed symmetric boundary conditions and sought stationary front solutions to (7.1.1); such a solution is equivalent to a site-centred solution on a domain of twice the size. Exploiting the symmetry of the solution to calculate only half the lattice points in this manner has the dual benefit of faster computation times and a vastly decreased chance of skipping between solution branches, which may otherwise occur all too readily given the high density of solutions within such a narrow parameter range. We have

chosen to focus here only on site-centred solutions; similar results are easy to find for the bond-centred solution branch. Of course, there is no symmetry to exploit when computing ladders, and so greater care must be used when calculating these at small values of $\hat{s}$.

Numerical results are compared to (7.1.14) in figures 7.2, with good agreement. Although an analytical formula is unavailable for $\psi \neq \frac{k\pi}{4}, k \in \{0, 1, \dots, 7\}$ as $\Lambda_{1,\psi}$ remains undetermined in these cases, we see that the snaking width appears to scale with $\hat{s}$ as predicted by (7.1.14) for all values of ψ shown. Note that numerical results are unavailable for very small $\hat{s}$, and that the smallest value of $\hat{s}$ for which numerical results are available increases with $m_1^2 + m_2^2$; this is due to the snaking width approaching values in which machine error is significant. The full analytical bifurcation diagram (6.8.8)-(6.8.9) for (7.1.1) is drawn in figure 7.3a, and a comparison between an analytical and a numerical snaking solution curve shown in figure 7.3b, again with good agreement.

7.2 Example: a cubic-quintic nonlinearity

Our second example is the discrete analogue of the SHE (3.0.1) studied in Chapters 3-5 and, for example, [14, 39], namely (7.0.1) with cubic and quintic nonlinearities, given by

$$\frac{\partial \hat{u}}{\partial t} = \Delta \hat{u} + \hat{r}\hat{u} + \hat{s}\hat{u}^3 - \hat{u}^5, \tag{7.2.1}$$

fixing $\hat{s} > 0$ to ensure bistablity. This equation was also studied in [85] to investigate snaking of fully two-dimensional localisations. Now, as in the last example, we must rescale (7.2.1) close to bifurcation to put it in the form (6.0.3). To this end, we define

$$\hat{u} = \sqrt{\epsilon}u, \qquad \hat{r} = \epsilon^2 r, \qquad \hat{s} = \epsilon s, \tag{7.2.2}$$

and, after substitution into (7.2.1), cancel the common factor of $\sqrt{\epsilon}$ to give

$$\frac{\partial u}{\partial t} = \Delta u - \epsilon^2 \left(-ru - su^3 + u^5\right). \tag{7.2.3}$$

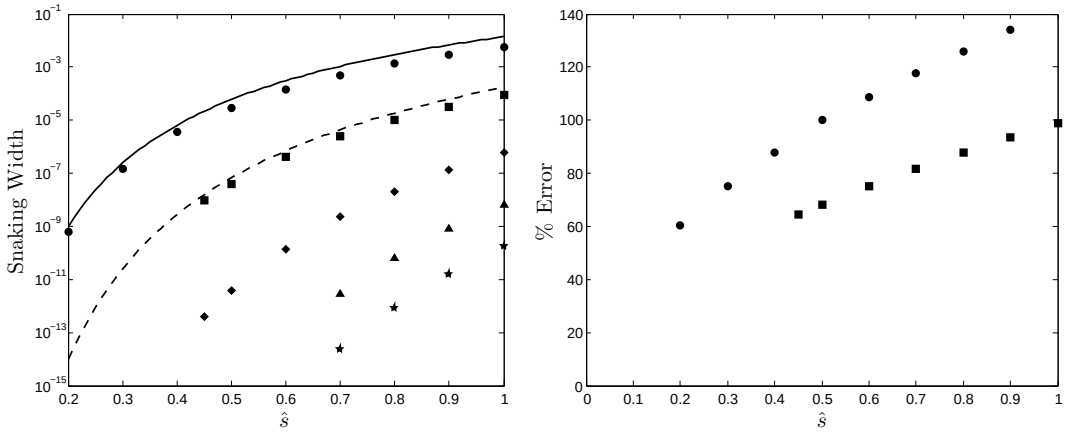

Figure 7.2: *Left: analytical (lines) and numerical (points) snaking widths for one-dimensional solutions to (7.1.1) at various orientations* $\psi = \arctan(m_2/m_1)$. *The solid line and circles represent* $(m_1, m_2) = (1, 0)$; *the dashed line and squares represent* $(m_1, m_2) = (1, 1)$; *diamonds represent* $(m_1, m_2) = (2, 1)$; *triangles represent* $(m_1, m_2) = (3, 1)$; *stars represent* $(m_1, m_2) = (3, 2)$. *Note an analytical formula is only available for the first two choices of* ψ. *Right: percentage error in analytical formula (7.1.14) for (7.1.1) with* $(m_1, m_2) = (1, 0)$ *represented by circles and* $(m_1, m_2) = (1, 1)$ *by squares.*

This is now equivalent to (6.0.3) with $F(u; r) = -ru - su^3 + u^5$. The bifurcation diagram for (7.2.1) with $\psi = 0$ can be seen in figure 6.1; unhatted variables in that figure correspond to hatted in (7.2.1). The system is bistable due to a subcritical pitchfork bifurcation at $\hat{r} = 0$ and a subsequent saddle-node bifurcation at some $\hat{r} < 0$, at which point the nontrivial solution curve turns over to form a region of bistability, within which is the snaking region.

The first task is to seek a one-dimensional, stationary front. We define Z as in (6.2.3), set $u \equiv u(Z)$ in (7.2.3) and impose the boundary conditions $u \to u_\pm$ as $Z \to \pm\infty$. In this case $u_- = 0$, which simplifies the algebra somewhat. Taylor expanding the differences in the same manner as in Section 6.3, the leading order continuum approximation is

$$0 = \frac{\mathrm{d}^2 u_0}{\mathrm{d}Z^2} + ru_0 + su_0^3 - u_0^5. \tag{7.2.4}$$

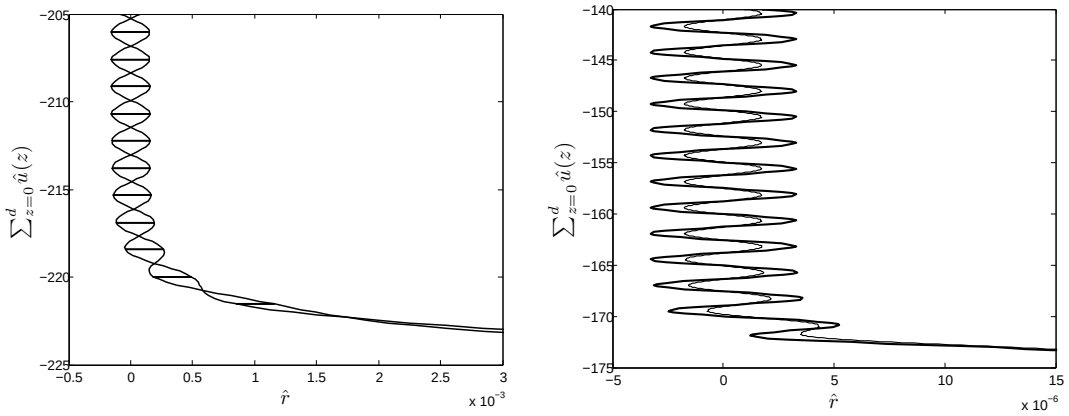

Figure 7.3: *Left: snakes-and-ladders bifurcation diagram for (7.1.1) with $\hat{s} = 0.6$ and $\psi = 0$, drawn using the analytical formulae (6.8.6)-(6.8.9). Right: comparison of analytical (thick line) and numerical (thin line) site-centred snaking curve for $\hat{s} = 0.4$ and $\psi = 0$.*

This can be integrated once after multiplication by u_0', leading to

$$0 = \frac{1}{2}\left(\frac{\mathrm{d}u_0}{\mathrm{d}Z}\right)^2 + \frac{1}{2}ru_0^2 + \frac{1}{4}su_0^4 - \frac{1}{6}u_0^6, \tag{7.2.5}$$

where the constant of integration vanishes because $u_- = 0$. The constant solutions $u = u_\pm$ must satisfy both (7.2.4) and (7.2.5); $u_- = 0$ does so trivially, but u_+ will only do so at $r = r_M$, the Maxwell point. Thus u_+ and r_M are determined by the coupled algebraic equations

$$\begin{aligned} 0 &= r_M + su_+^2 - u_+^4, \\ 0 &= \frac{1}{2}r_M + \frac{1}{4}su_+^2 - \frac{1}{6}u_+^4, \end{aligned} \tag{7.2.6}$$

which are readily solved to give

$$u_+ = +\sqrt{\frac{3}{4}s}, \quad r_M = -\frac{3}{16}s^2. \tag{7.2.7}$$

Setting $r = r_M$ and rearranging, (7.2.5) becomes

$$\frac{3}{2}\left(\frac{\mathrm{d}u_0}{\mathrm{d}Z}\right)^2 = u_0^2\left(\frac{3}{4}s - u_0^2\right)^2, \tag{7.2.8}$$

which may be integrated to give

$$u_0(Z) = \left(\frac{3}{4}\right)^{1/4} \frac{\sqrt{\mu}}{\sqrt{1 + e^{-\mu Z}}}, \tag{7.2.9}$$

where

$$\mu = \frac{\sqrt{3}}{2}s, \tag{7.2.10}$$

and we have chosen the positive square root in order that $u_+ > u_-$; the front of opposite orientation may be recovered by exploiting the reversibility of (7.2.1).

We now need to evaluate the various constants which appear in the bifurcation equations (6.8.8) and (6.8.9). From (7.2.9), we can see that the singularities ζ of u_0 are

$$\zeta = \zeta_m := (2m+1)\pi i/\mu, \qquad m \in \mathbb{Z}, \tag{7.2.11}$$

each of which has strength $\gamma = \frac{1}{2}$. Thus (6.7.3) gives $\chi = \mathrm{Arg}\left(\Lambda_{1,\psi}\right)$. The dominant singularities are those nearest (and equidistant from) the real line, namely ζ_0 and $\zeta_{-1} = \zeta_0^*$. Also, since

$$u_0 \sim \left(\frac{3}{4}\right)^{1/4}\sqrt{\mu}\left(1 - \frac{1}{2}e^{-\mu Z}\right) \tag{7.2.12}$$

as $Z \to \infty$ and $F_{r,M}(u) = -u$, we have

$$\alpha_+ = \mu, \qquad D_+ = \frac{1}{2}\left(\frac{3}{4}\right)^{1/4}\sqrt{\mu}, \qquad \int_{u_-}^{u_+} F_{r,M}(v)\mathrm{d}v = -\frac{1}{2}\left(\frac{3}{4}\right)^{1/2}\mu. \tag{7.2.13}$$

Thus the bifurcation equations (6.8.8) and (6.8.9) can now be written in terms of the parameters of the scaled equation (7.2.3). Again, we shall not write these out in full and simply write down the width of the snaking region from (6.7.5), which now reads

$$|\delta r| \leq \frac{8\pi\left|\Lambda_{1,\psi}\right| e^{-2\pi^2\sqrt{(m_1^2+m_2^2)}/\epsilon\mu}}{\sqrt{3}\epsilon^3\mu}. \tag{7.2.14}$$

Writing this in terms of the original, hatted variables appearing in (7.2.1) yields

$$|\hat{r} - \hat{r}_M| \leq \frac{16\pi\left|\Lambda_{1,\psi}\right| e^{-4\pi^2\sqrt{3(m_1^2+m_2^2)}/3\hat{s}}}{3\hat{s}}, \tag{7.2.15}$$

where $\hat{r}_M = -3\hat{s}^2/16 + \mathrm{O}\left(\hat{s}^4\right)$ is the unscaled Maxwell point and $\hat{s}$ provides the small variable. This formula corresponds to that derived in [67] using variational approximations (equation (50) in that work); however, the method presented here yields a complete formula, whereas that in [67] is unable to determine the constant factor $16\pi|\Lambda_{1,\psi}|/\sqrt{3}$. We also note that the functional dependence of (7.2.15) on $\hat{s}$ when

$(m_1, m_2) = (1, 0)$ is identical to that of the corresponding formula (4.7.6) derived in Chapter 4 for the cubic-quintic SHE (3.0.1). However, the snaking width is much smaller in the present case, as $e^{-1/\hat{s}}$ is raised to the power ≈ 22.8 in (7.2.15), and only to the power ≈ 15.3 in (4.7.6).

All that remains is to derive the constants $\Lambda_{1,\psi}$. In a similar manner as in Section (7.1.1), we have

$$u_n \sim \frac{U_n}{(Z-\zeta_m)^{2n+1/2}}, \tag{7.2.16}$$

as $Z \to \zeta_m$, for some sequence of constants U_n which can be found by iteration of the recurrence relation

$$\begin{aligned} 0 = 2\sum_{p=1}^{n+1} \frac{\cos^{2p}\psi + \sin^{2p}\psi}{(2p)!} \frac{\Gamma\left(2n+\frac{5}{2}\right)}{\Gamma\left(2n-2p+\frac{5}{2}\right)} U_{n-p+1} \\ - \sum_{p_1=0}^{n} \sum_{p_2=0}^{n-p_1} \sum_{p_3=0}^{n-p_1-p_2} \sum_{p_4=0}^{n-p_1-p_2-p_3} U_{p_1} U_{p_2} U_{p_3} U_{p_4} U_{n-p_1-p_2-p_3-p_4}, \end{aligned} \tag{7.2.17}$$

where $U_0 = \left(\frac{3}{4}\right)^{1/4}$. Again, due to the dominant contribution from complex eigenvalues at other values of ψ, we are only able to calculate $\Lambda_{1,\psi}$ when $\psi = \frac{k\pi}{4}$, $k \in \{0, 1, \ldots, 7\}$. For such orientations

$$\Lambda_{1,\psi} \sim \lim_{n\to\infty} \frac{(12)^{1/4}(-1)^{n+1}\left(2\pi\sqrt{m_1^2+m_2^2}\right)^{2n+3}}{\Gamma(2n+3)} U_n. \tag{7.2.18}$$

By iteration of (7.2.17), we are therefore able to calculate $\Lambda_{1,0} \approx -89$ and $\Lambda_{1,\pi/4} \approx -252$; $\Lambda_{1,\psi}$ for $\psi = \frac{k\pi}{4}$, $k \in \{2, 3, \ldots, 7\}$ then follow using the invariance of (7.0.1) under rotations $\psi \to \psi + \frac{\pi}{2}$.

Numerical computations for $\psi = 0, \frac{\pi}{4}$ are compared to (7.2.15) in figure 7.4, with good agreement. Note that machine error becomes significant at much larger values of $\hat{s}$ than in the example of Section 7.1; this is because the exponent in (7.2.15) is larger than that in (7.1.14). The full analytical bifurcation diagram is drawn in figure 7.5a using the value of $\Lambda_{1,\psi}$ calculated from the recurrence relation (7.1.16), and a comparison between an analytical and a numerical snaking solution curve shown in figure 7.5b.

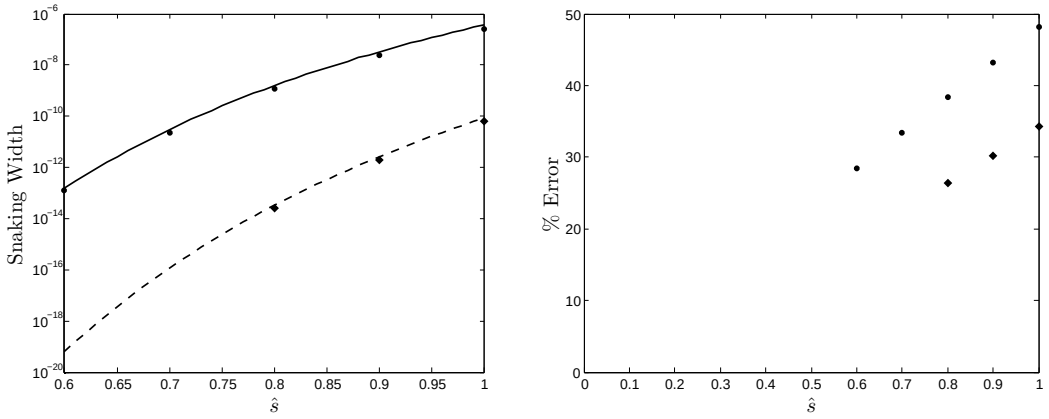

Figure 7.4: *Left: comparison of analytical (lines) and numerical (data points) snaking widths for (7.2.1). Right: percentage error in analytical formula compared to numerical results. Solid lines or circles correspond to $\psi = 0$, and dashed lines or diamonds to $\psi = \frac{\pi}{4}$.*

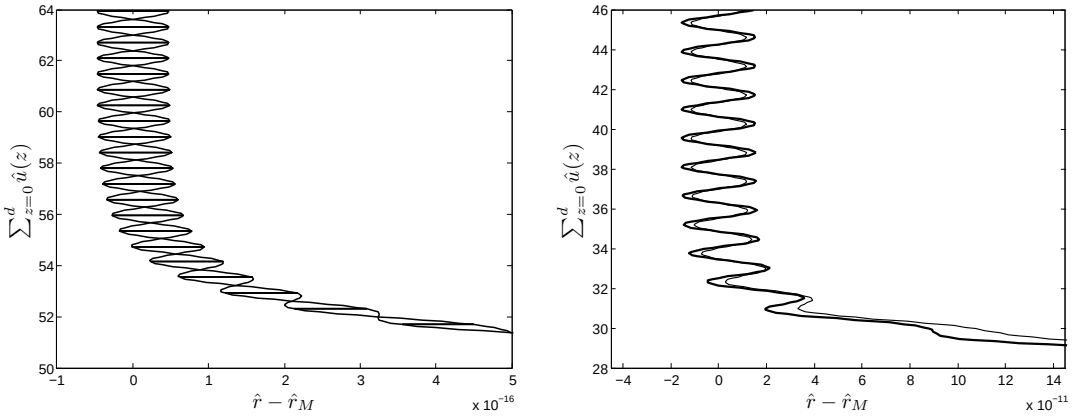

Figure 7.5: *Left: snakes-and-ladders bifurcation diagram for (7.2.1) with $\hat{s} = 0.5$ and $\psi = 0$, drawn using the analytical formulae (6.8.6)-(6.8.9). Right: comparison of analytical (thick line) and numerical (thin line) site-centred snaking curve for $\hat{s} = 0.7$ and $\psi = 0$.*

CHAPTER 8

Discussion

We have successfully applied the method of exponential asymptotics to homoclinic snaking problems in both continuous (Chapters 3-5) and discrete systems (Chapters 6-7). The continuous system we chose was the cubic-quintic SHE (3.0.1). Close to onset of a pattern-forming instability, conventional multiple-scales techniques at algebraic orders reveal a leading-order steady front (Section 3.2) connecting the patterned state to the trivial solution. However, this was predicted to exist only at the Maxwell point, thus failing to produce the snaking region. Because the snaking region is exponentially small, beyond-all-orders effects in the tail of the (divergent) asymptotic expansion must be accounted for in order to fully describe it.

To this end, we first derived the behaviour of the late terms in the expansion using the usual factorial-over-power ansatz (4.5.1) [1, 51]. These late terms were seen to consist of contributions (4.5.14) from each of the complex singularities of the leading-order solution, the dominant ones being those closest to the real line. Truncating optimally by truncating each of these contributions after their least term, we saw that the remainder is not algebraically small but exponentially small.

Due to truncation, the remainder equation (4.6.6) is inhomogeneous. Rescaling the slow variable $X = \epsilon^2 x$ in the vicinity of the Stokes lines, i.e. close to maximal forcing,

we saw explicitly how the coefficient of a complementary function to the remainder equation varies smoothly from zero to non-zero as the Stokes lines are crossed (4.6.30). Both this complementary function and a particular integral due to a deviation from the Maxwell point are exponentially growing in the far-field. Requiring that these unbounded contributions vanish provides a condition relating the phase of the pattern to the deviation from the Maxwell point, thus yielding the pinning mechanism which is ultimately responsible for the snaking phenomenon. Furthermore, pinning may only occur within an exponentially small distance from the Maxwell point, providing a formula (4.7.7) for the width of the snaking region.

Armed with the full asymptotic expansion of a stationary front, we were then able to construct localised patterns by matching two fronts placed back-to-back. The resultant matching conditions (5.2.7)-(5.2.9) relate the (not necessarily equal) phase of each front and the front separation to one another; these equations describe the snakes-and-ladders bifurcation structure as the front separation varies. Thus we were able to draw the bifurcation diagram analytically and compare the results with numerical simulations. These comparisons are underpinned by a constructive derivation of the constant Λ_1. We were also able to extend this process to construct symmetric two-pulses by matching together the exponentially decaying tails of two localised patches, and showed how this interaction causes the snakes-and-ladders bifurcation to break up into an infinite sequence of figure-of-eight isolas, in agreement with [4, 15, 53].

We found that the analytical formula for the snaking width gave good agreement in the limit $s \to 0$, as expected, albeit consistently giving a slight overestimate. However, while the error for $s = 1$ is $\approx 100\%$, for $s = 0.5$ it is $\approx 50\%$ (see figure 4.2), indicating that we may have confidence in our predictions in the small-s limit. This confidence is bolstered by the striking similarity that our formula bears to that derived by Susanto and Matthews using variational methods [83], reproduced here in (4.7.9), although the result of Chapter 4) is the more accurate as it takes into account exponentially small

terms as well as those at leading order.

We then switched focus to study discrete snaking in the differential-difference equation (6.0.3) in Chapters 6-7. Application of the method follows a similar process as that in Chapters 4-5, and also produces a set of formulae (6.8.8)-(6.8.9) describing the snakes-and-ladders bifurcation within the exponentially small snaking region (6.7.5). However, rather than confining solutions to the real line as in Chapters 4-5, we considered solutions to (6.0.3) which were localised in one direction at an arbitrary orientation ψ to a square lattice. In this case, we showed that no exponentially growing terms are switched on in the remainder when $\tan\psi$ is irrational, resulting in a snaking width of zero. In addition, we found that when $\tan\psi = m_2/m_1$, where $\gcd(|m_1|,|m_2|) = 1$ and $\tan\pm\frac{\pi}{2} = \pm\infty$, the snaking width (6.7.5) decreases exponentially as $(m_1^2 + m_2^2)^{1/2}$ increases.

The results of Chapter 6 were derived for an arbitrary nonlinearity in (6.0.3). Thus, in order to validate them numerically, we considered two specific examples in Chapter 7. Unfortunately, we were unable to provide a quantitative comparison with numerical results for all values of ψ, due to the lack of a method to compute the Stokes multiplier $\Lambda_{1,\psi}$ when $\psi \neq \frac{k\pi}{4}$, $k \in \{0,1,\ldots,7\}$; however, comparison with numerical results indicates that the analytical formulae (6.7.5) for the snaking width scales in the correct manner. Moreover, agreement between numerical and analytical results is good for values of ψ for which we were able to calculate $\Lambda_{1,\psi}$.

Thus we have demonstrated how the method of exponential asymptotics may be used to describe homoclinic snaking near bifurcation, following the work in [22, 51, 56]. Furthermore, we have found that the method is applicable even when the leading-order solution is not known explicitly. Motivated by our results, we shall now discuss some possible directions for further work.

8.1 Further work

Much of the current understanding of homoclinic snaking is in the context of systems which are variational in time, conservative in space and reversible [4, 13, 96]. Although progress has been made in extending results to problems in which these properties no longer hold [10, 11, 54, 79] the picture is still far from clear. The methods used in this thesis should also apply to problems of this type; for example the SHE with additional terms such as those studied in [11]. It should be a relatively simple matter to keep track of the extra terms through the exponential asymptotic equation, and thus see how these terms affect the structure of the snaking region. The method should also be applicable to the slanted snaking seen in systems with a conserved quantity or nonlocal terms [35, 43].

The description of multi-pulses presented in Chapter 5 is far from complete, as we have only considered symmetric two-pulses, and there are infinitely many other multi-pulses in an infinite domain. While the matching process for solutions with more than two pulses is unlikely to be analytically tractable, we expect further progress can be made than has been reported in Chapter 5. Although the matching conditions (5.3.5)-(5.3.6) and (5.3.8)-(5.3.9) are relatively complicated, preliminary investigations in the limit of large pulse-width (i.e. setting the left-hand side of each matching condition to zero) look promising. Further work is required to fully elucidate the phenomenon, as are detailed numerical calculations against which to compare analytical results. Indeed, little work has been done on multi-pulses, so further numerical work would be of value in itself [4, 15, 53].

Some perhaps more interesting extensions of our work are motivated by the fact that our calculation in Chapter 6 was done without specifying the nonlinearity $F(u;r)$ in the discrete system (6.0.3); see also [21, 51]. In fact, we were able to derive a general set of formulae for the snakes-and-ladders bifurcation diagram without knowing explicitly

what the leading-order front looked like. This is a great strength of the exponential asymptotic method, as it allows much information to be gleaned from systems which are otherwise impervious to asymptotic analysis. One immediate use for the results of Chapter 6 is to systems such as the saturated nonlinearity studied in [99], in which a leading-order front is unavailable. If a numerical front solution can be found, and extended into the complex plane to determine the position of the singularities, the bifurcation equations (6.8.8)-(6.8.9) could be used to provide a 'semi-analytical' description of the snaking region. We note also that there is no reason why a similar result may not be obtained for generalisations of the SHE studied in Chapters 3-5.

Moreover, it is likely that the exponential asymptotic method may prove especially useful in the study of higher-dimensional and time-dependent snaking behaviour. Very little is known about such problems [2, 16, 38, 61, 62, 68, 69, 90], in large part due to the failure of dynamical systems techniques in systems with more than one 'time-like' variable; of course, the situation is not helped by the substantially more difficult numerical calculations required. However, since the exponential asymptotic method does not require an explicit leading-order solution, commonly unavailable in higher dimensions, to be successful, it provides a very promising technique with which to investigate such problems. Indeed, higher-dimensional and time-dependent exponential asymptotics is a worthy candidate of research in its own right, as very little has been done [9, 23]. We remark also that discrete systems such as (6.0.3) are an ideal candidate for such studies, as they are simpler than, say, the two-dimensional SHE, and much easier to solve numerically, while exhibiting very similar snaking behaviour. The obvious starting point is to consider asymptotic solutions to (6.0.3) which are radially symmetric at leading-order; higher-order equations are obviously not radially symmetric, and it would be interesting to see how this affects the form of the solution and resultant snaking behaviour.

Another potential use for the calculation of Chapter 6 is in elucidating how fully two-

dimensional localisations evolve along their solution curves. In a numerical study [85] of the specific example (7.2.1), Taylor and Dawes describe this rather complex behaviour and observe several distinct snaking widths. Moreover, the localised patch consists of different superpositions of one-dimensional fronts such as those studied in Chapter 6 at different points along the snaking curve. Thus the analytical description of fronts with arbitrary orientation in the plane developed in Chapter 6 may shed light on how two-dimensional localised patches increase in extent.

We have seen that the method presented first by Kozyreff and Chapman [22, 56] and applied further here provides a self-consistent and rigorous derivation of the behaviour the snaking region in the cubic-quintic SHE. In deriving explicitly the effects of Stokes lines in the asymptotic expansions of stationary fronts, we have provided further support of Pomeau's intuitive explanation that it is phase-locking between spatial scales which is responsible for fronts remaining stationary close to the Maxwell point [74], and that this pinning leads to homoclinic snaking. We expect that the techniques given here will prove extremely useful in the investigation of other localised phenomena about which little is presently known, as well as having broader application to problems in pattern formation and nonlinear dynamics.

APPENDIX A

On complex solutions of the eigenvalue equation (6.4.5)

Suppose that $\kappa = a + ib$ is such that (6.4.5) holds, i.e.

$$\cos(\kappa \cos\psi) + \cos(\kappa \sin\psi) - 2 = 0 \tag{A.0.1}$$

and a and b are real, non-zero constants. As $\sin^2\Theta + \cos^2\Theta \equiv 1$, (6.4.10) can be rewritten to give

$$\cos^2\psi\left(1 - \cos^2(\kappa\cos\psi)\right) = \sin^2\psi\left(1 - \cos^2(\kappa\sin\psi)\right). \tag{A.0.2}$$

Thus (A.0.1) and (A.0.2) taken together may be formulated as a system of two algebraic equations, treating $\cos(\kappa\cos\psi)$ and $\cos(\kappa\sin\psi)$ as two unknown constants. Of course, in actuality there is only one unknown, the eigenvalue κ; any solution must therefore provide a consistent value of κ.

Solving this system is a simple exercise, and we find upon doing so that either $\cos(\kappa\cos\psi) = \cos(\kappa\sin\psi) = 1$, or

$$\cos(\kappa\cos\psi) = \frac{3\tan^2\psi + 1}{\tan^2\psi - 1}, \qquad \cos(\kappa\sin\psi) = -\frac{\tan^2\psi + 3}{\tan^2\psi - 1}. \tag{A.0.3}$$

The first instance gives real κ and is simply the solution given by (6.4.6) and (6.4.7), which we have already discussed fully in Chapter 6. In the second instance, separating

κ into its real and imaginary parts, we have

$$\cos(a\cos\psi)\cosh(b\cos\psi) - i\sin(a\cos\psi)\sinh(b\cos\psi) = \frac{3\tan^2\psi + 1}{\tan^2\psi - 1}, \tag{A.0.4}$$

$$\cos(a\sin\psi)\cosh(b\sin\psi) - i\sin(a\sin\psi)\sinh(b\sin\psi) = -\frac{\tan^2\psi + 3}{\tan^2\psi - 1}. \tag{A.0.5}$$

However, the imaginary part of both of the above equations must vanish, as the right-hand side of each is real. Therefore $\sin(a\cos\psi) = \sin(a\sin\psi) = 0$, giving $a\cos\psi = 2M_1\pi$, $a\sin\psi = 2M_2\pi$ for $(M_1, M_2) \in \mathbb{Z}^2$. However, (A.0.1) now reads

$$\cos(\kappa\cos\psi) + \cos(\kappa\sin\psi) = \cosh(b\cos\psi) + \cosh(b\sin\psi) = 2. \tag{A.0.6}$$

This has real solutions only if $b\cos\psi = b\sin\psi = 0$, which gives $b = 0$, a contradiction as $b = \Im\kappa \neq 0$. Thus there are no solutions κ to (6.4.5) with $\Im(\kappa) \neq 0$ that also satisfy (6.4.10).

References

[1] K.L. Adams, J.R. King, and R.H. Tew. Beyond-all-orders effects in multiple-scales asymptotics: travelling-wave solutions to the Kuramoto-Sivashinsky equation. *J. Eng. Math.*, 45(3):197–226, 2003.

[2] D. Avitabile, D.J.B. Lloyd, J. Burke, E. Knobloch, and B. Sandstede. To snake or not to snake in the planar Swift–Hohenberg equation. *SIAM J. Appl. Dyn. Syst.*, 9(3):704–733, 2010.

[3] O. Batiste, E. Knobloch, A. Alonso, and I. Mercader. Spatially localized binary-fluid convection. *J. Fluid Mech.*, 560:149–158, 2006.

[4] M. Beck, J. Knobloch, D.J.B. Lloyd, B. Sandstede, and T. Wagenknecht. Snakes, ladders, and isolas of localized patterns. *SIAM J. Math. Anal*, 41(3):936–972, 2009.

[5] D. Bensimon, B.I. Shraiman, and V. Croquette. Nonadiabatic effects in convection. *Phys. Rev. A*, 38(10):5461–5464, 1988.

[6] A. Bergeon, J. Burke, E. Knobloch, and I. Mercader. Eckhaus instability and homoclinic snaking. *Phys. Rev. E*, 78(4):046201, 2008.

[7] M.V. Berry. Uniform asymptotic smoothing of Stokes's discontinuities. *Proc. R. Soc. Londn. A*, 422:7–21, 1989.

[8] S. M. Blanchflower. Magnetohydrodynamic convectons. *Phys. Lett. A*, 261(1), 1999.

[9] G.L. Body, J.R. King, and R.H. Tew. Exponential asymptotics of a fifth-order partial differential equation. *Euro. J. Appl. Math.*, 16(05):647–681, 2005.

[10] J. Burke and J.H.P. Dawes. Localised states in an extended Swift-Hohenberg equation. *SIAM J. Appl. Dyn. Syst.*, 11(1):261–284, 2012.

[11] J. Burke, S.M. Houghton, and E. Knobloch. Swift-Hohenberg equation with broken reflection symmetry. *Phys. Rev. E*, 80(3):036202, 2009.

[12] J. Burke and E. Knobloch. Localized states in the generalized Swift-Hohenberg equation. *Phys. Rev. E*, 73(5):056211, 2006.

[13] J. Burke and E. Knobloch. Homoclinic snaking: structure and stability. *Chaos*, 17(3):037102, 2007.

[14] J. Burke and E. Knobloch. Snakes and ladders: localized states in the Swift–Hohenberg equation. *Phys. Lett. A*, 360(6):681–688, 2007.

[15] J. Burke and E. Knobloch. Multipulse states in the Swift-Hohenberg equation. *Dynamical Systems*, pages 109–117, 2009.

[16] J. Burke, A. Yochelis, and E. Knobloch. Classification of spatially localized oscillations in periodically forced dissipative systems. *SIAM J. Appl. Dyn. Syst*, 7:651–711, 2008.

[17] D.C. Calvo, T.S. Yang, and T.R. Akylas. On the stability of solitary waves with decaying oscillatory tails. *Proc. Roy. Soc. Lond. A*, 456(1995):469–487, 2000.

[18] A.R. Champneys. Homoclinic orbits in reversible systems and their applications in mechanics, fluids and optics. *Physica D*, 112(1-2):158–186, 1998.

[19] S.J. Chapman. On the non-universality of the error function in the smoothing of Stokes discontinuities. *Proc. R. Soc. Lond.*, 452.

[20] S.J. Chapman, C.J. Howls, J.R. King, and A.B. Olde Daalhuis. Why is a shock not a caustic? The higher-order Stokes phenomenon and smoothed shock formation. *Nonlinearity*, 20:2425, 2007.

[21] S.J. Chapman, J.R. King, and K.L. Adams. Exponential asymptotics and Stokes lines in nonlinear ordinary differential equations. *Proc. R. Soc. Lond. A*, 454.

[22] S.J. Chapman and G. Kozyreff. Exponential asymptotics of localised patterns and snaking bifurcation diagrams. *Physica D*, 238(3):319–354, 2009.

[23] S.J. Chapman and D.B. Mortimer. Exponential asymptotics and Stokes lines in a partial differential equation. *Proc. R. Soc. Lond. A*, 461(2060):2385–2421, 2005.

[24] S.J. Chapman and J. Vanden-Broeck. Exponential asymptotics and gravity waves. *J. Fluid Mech.*, 567:299–326, 2006.

[25] S.J. Chapman and J.M. Vanden-Broeck. Exponential asymptotics and capillary waves. *SIAM J. Appl. Math.*, 62(6):1872–1898, 2002.

[26] C. Chong, R. Carretero-González, B.A. Malomed, and P.G. Kevrekidis. Multistable solitons in higher-dimensional cubic-quintic nonlinear Schrödinger lattices. *Physica D*, 238(2):126–136, 2009.

[27] M.G. Clerc, R.G. Elías, and R.G. Rojas. Continuous description of lattice discreteness effects in front propagation. *Phil. Trans. R. Soc. A*, 369(1935):412–424, 2011.

[28] M.G. Clerc and C. Falcon. Localized patterns and hole solutions in one-dimensional extended systems. *Physica A*, 356(1):48–53, 2005.

[29] M.G. Clerc, C. Falcon, and E. Tirapegui. Comment on 'Asymptotics of large bound states of localized structures'. *Phys. Rev. Lett.*, 100(4):049401, 2008.

[30] S. Coombes, G.J. Lord, and M.R. Owen. Waves and bumps in neuronal networks with axo-dendritic synaptic interactions. *Physica D*, 178(3-4):219–241, 2003.

[31] P. Coullet, C. Riera, and C. Tresser. Stable static localized structures in one dimension. *Phys. Rev. Lett.*, 84(14):3069–3072, 2000.

[32] S.M. Cox and P.C. Matthews. Instability and localisation of patterns due to a conserved quantity. *Physica D*, 175(3-4):196–219, 2003.

[33] M.C. Cross and P.C. Hohenberg. Pattern formation outside of equilibrium. *Rev. Mod. Phys.*, 65(3):851–1112, 1993.

[34] J.H.P. Dawes. Localized convection cells in the presence of a vertical magnetic field. *J. Fluid Mech.*, 570(1):385–406, 2007.

[35] J.H.P. Dawes. Localized pattern formation with a large-scale mode: slanted snaking. *SIAM J. Appl. Dyn. Syst.*, 7:186, 2008.

[36] J.H.P. Dawes. Modulated and localized states in a finite domain. *SIAM J. Appl. Dyn. Syst*, 8:909–930, 2009.

[37] J.H.P. Dawes. The emergence of a coherent structure for coherent structures: localized states in nonlinear systems. *Phil. Trans. R. S. A*, 368(1924):3519–3534, 2010.

[38] J.H.P. Dawes and S. Lilley. Localized states in a model of pattern formation in a vertically vibrated layer. *SIAM J. Appl. Dyn. Syst.*, 9:238, 2010.

[39] A.D. Dean, P.C. Matthews, S.M. Cox, and J.R. King. Exponential asymptotics of homoclinic snaking. *Nonlinearity*, 24:3323, 2011.

[40] A.D. Dean, P.C. Matthews, S.M. Cox, and J.R. King. One-dimensional snaking on a planar lattice. *preprint*, 2012.

[41] S. Fauve and O. Thual. Solitary waves generated by subcritical instabilities in dissipative systems. *Phys. Rev. Lett.*, 64(3):282–284, 1990.

[42] W.J. Firth, L. Columbo, and T. Maggipinto. On homoclinic snaking in optical systems. *Chaos*, 17:037115, 2007.

[43] W.J. Firth, L. Columbo, and A.J. Scroggie. Proposed resolution of theory-experiment discrepancy in homoclinic snaking. *Phys. Rev. Lett.*, 99(10):104503, 2007.

[44] A. Hoffman and J. Mallet-Paret. Universality of crystallographic pinning. *J. Dyn. Diff. Equat.*, 22(2):79–119, 2010.

[45] S.M. Houghton and E. Knobloch. Homoclinic snaking in bounded domains. *Phys. Rev. E*, 80(2):026210, 2009.

[46] R.B. Hoyle. *Pattern formation: an introduction to methods*. Cambridge Univ. Pr., 2006.

[47] G.W. Hunt, M.A. Peletier, A.R. Champneys, P.D. Woods, M. Ahmer Wadee, C.J. Budd, and G.J. Lord. Cellular buckling in long structures. *Nonlinear Dynamics*, 21(1):3–29, 2000.

[48] H.J. Hupkes, D. Pelinovsky, and B. Sandstede. Propagation failure in the discrete Nagumo equation. *Proc. Amer. Math. Soc*, 139(10):3537–3551, 2011.

[49] G. Hwang, TR Akylas, and J. Yang. Gap solitons and their linear stability in one-dimensional periodic media. *Physica D*, 240(12):1055–1068, 2011.

[50] G. Hwang, T.R. Akylas, and J. Yang. Solitary waves and their linear stability in nonlinear lattices. *Stud. Appl. Math.*, 128(3):275–298, 2012.

[51] J.R. King and S.J. Chapman. Asymptotics beyond all orders and Stokes lines in nonlinear differential-difference equations. *Euro. J. Appl. Math.*, 12(04):433–463, 2001.

[52] E. Knobloch. Spatially localized structures in dissipative systems: open problems. *Nonlinearity*, 21(4):45, 2008.

[53] J. Knobloch, D.J.B. Lloyd, B. Sandstede, and T. Wagenknecht. Isolas of 2-pulse solutions in homoclinic snaking scenarios. *J. Dyn. Diff. Equat.*, 23(1):93–114, 2011.

[54] J. Knobloch, M. Vielitz, and T. Wagenknecht. Non-reversible perturbations of homoclinic snaking scenarios. *preprint*.

[55] G. Kozyreff, P. Assemat, and SJ Chapman. Influence of boundaries on localized patterns. *Phys. Rev. Lett.*, 103(16):164501, 2009.

[56] G. Kozyreff and S.J. Chapman. Asymptotics of large bound states of localized structures. *Phys. Rev. Lett.*, 97(4):044502, 2006.

[57] G. Kozyreff and S.J. Chapman. Kozyreff and Chapman reply. *Phys. Rev. Lett.*, 100(4):049402, 2008.

[58] C.R. Laing and W.C. Troy. PDE methods for nonlocal models. *SIAM J. Appl. Dyn. Syst.*, 2(3):487–516, 2003.

[59] C.R. Laing, W.C. Troy, B. Gutkin, and G.B. Ermentrout. Multiple bumps in a neuronal model of working memory. *SIAM J. Appl. Math.*, 63(1):62–97, 2002.

[60] K.J. Lee, W.D. McCormick, J.E. Pearson, and H.L. Swinney. Experimental observation of self-replicating spots in a reaction-diffusion system. *Nature*, 369(6477):215–218, 1994.

[61] D.J.B. Lloyd and B. Sandstede. Localized radial solutions of the Swift–Hohenberg equation. *Nonlinearity*, 22(2):485–524, 2009.

[62] D.J.B. Lloyd, B. Sandstede, D. Avitabile, and A.R. Champneys. Localized hexagon patterns of the planar Swift–Hohenberg equation. *SIAM J. Appl. Dyn. Syst.*, 7:1049–1100, 2008.

[63] C.J. Lustri, S.W. McCue, and B.J. Binder. Free surface flow past topography: a beyond-all-orders approach. *Euro. J. of Appl. Math.*, 1(1):1–27, 2012.

[64] Y.P. Ma, J. Burke, and E. Knobloch. Defect-mediated snaking: A new growth mechanism for localized structures. *Physica D*, 239(19):1867–1883, 2010.

[65] J. Mallet-Paret. *Crystallographic pinning: direction dependent pinning in lattice differential equations*. Lefschetz Center for Dynamical Systems and Center for Control Sciences, Division of Applied Mathematics, Brown University, 2001.

[66] P.C. Matthews and S.M. Cox. Pattern formation with a conservation law. *Nonlinearity*, 13(4):1293–1320, 2000.

[67] P.C. Matthews and H. Susanto. Variational approximations to homoclinic snaking in continuous and discrete systems. *Phys. Rev.E*, 84(6):066207, 2011.

[68] S. McCalla. Spots in the Swift–Hohenberg equation. *preprint*, 2012.

[69] S. McCalla and B. Sandstede. Snaking of radial solutions of the multi-dimensional Swift-Hohenberg equation: a numerical study. *Physica D*, 239(16):1581–1592, 2010.

[70] J.B. McLeod. Smoothing of Stokes discontinuities. *Proc. Roy. Soc. Lond. A*, 437(1900):343–354, 1992.

[71] I. Mercader, O. Batiste, A. Alonso, and E. Knobloch. Localized pinning states in closed containers: homoclinic snaking without bistability. *Phys. Rev. E*, 80(2):025201, 2009.

[72] A.B. Olde Daalhuis, S.J. Chapman, J.R. King, J.R. Ockendon, and R.H. Tew. Stokes phenomenon and matched asymptotic expansions. *SIAM J. Appl. Math.*, 55(6):1469–1483, 1995.

[73] U. Peschel, D. Michaelis, and C.O. Weiss. Spatial solitons in optical cavities. *IEEE J. Quant. Elect.*, 39(1):51–64, 2003.

[74] Y. Pomeau. Front motion, metastability and subcritical bifurcations in hydrodynamics. *Physica D*, 23(1-3):3–11, 1986.

[75] R. Richter and I.V. Barashenkov. Two-dimensional solitons on the surface of magnetic fluids. *Phys. Rev. Lett.*, 94(18):184503, 2005.

[76] H. Riecke and G.D. Granzow. Localization of waves without bistability: worms in nematic electroconvection. *Phys. Rev. Lett.*, 81(2):333–336, 1998.

[77] A. Roxin and H. Riecke. Destabilization and localization of traveling waves by an advected field. *Physica D*, 156(1-2):19–38, 2001.

[78] H. Sakaguchi and H.R. Brand. Stable localized solutions of arbitrary length for the quintic Swift-Hohenberg equation. *Physica D*, 97(1-3):274–285, 1996.

[79] B. Sandstede and Y. Xu. Snakes and isolas in non-reversible conservative systems. *preprint*, 2011.

[80] H. Schmidt and S. Coombes. Snaking behavior of homoclinic solutions in a neural field model. *BMC Neuroscience*, 10(Suppl 1):P297, 2009.

[81] T.M. Schneider, J.F. Gibson, and J. Burke. Snakes and ladders: localized solutions of plane Couette flow. *Phys. Rev. Lett.*, 104(10):104501, 2010.

[82] V.S. Solomatov. Localized subcritical convective cells in temperature-dependent viscosity fluids. *Phys. Earth Planet. Inter.*, 200–201:63–71, 2012.

[83] H. Susanto and P.C. Matthews. Variational approximations to homoclinic snaking. *Phys. Rev. E*, 83(3):035201, 2011.

[84] J. Swift and P.C. Hohenberg. Hydrodynamic fluctuations at the convective instability. *Phys. Rev. A*, 15(1):319–328, 1977.

[85] C.R.N. Taylor and J.H.P. Dawes. Snaking and isolas of localized states in bistable discrete lattices. *Phys. Lett. A*, 375:14–22, 2010.

[86] M. Tlidi, P. Mandel, and R. Lefever. Localized structures and localized patterns in optical bistability. *Phys. Rev. Lett.*, 73(5):640–643, 1994.

[87] P.H. Trinh, S.J. Chapman, and J.M. Vanden-Broeck. Do waveless ships exist? Results for single-cornered hulls. *J. Fluid Mech.*, 685(1):413–439, 2011.

[88] P.B. Umbanhowar, F. Melo, and H.L. Swinney. Localized excitations in a vertically vibrated granular layer. *Nature*, 382(6594):793–796, 1996.

[89] J.B. van den Berg and J.R. King. Vanishing beyond all orders: Stokes lines in a water-wave model equation. *Nonlinearity*, 23(1), 2010.

[90] P. van Heijster and B. Sandstede. Planar radial spots in a three-component FitzHugh–Nagumo system. *J. Nonlinear Science*, pages 1–41, 2011.

[91] V.K. Vanag and I.R. Epstein. Stationary and oscillatory localized patterns, and subcritical bifurcations. *Phys. Rev. Lett.*, 92(12):128301, 2004.

[92] A.G. Vladimirov, J.M. McSloy, D.V. Skryabin, and W.J. Firth. Two-dimensional clusters of solitary structures in driven optical cavities. *Phys. Rev. E*, 65(4):046606, 2002.

[93] M.K. Wadee and A.P. Bassom. Effects of exponentially small terms in the perturbation approach to localized buckling. *Proc. R. Soc. Lond. A*, 455(1986):2351–2370, 1999.

[94] M.K. Wadee, C.D. Coman, and A.P. Bassom. Solitary wave interaction phenomena in a strut buckling model incorporating restabilisation. *Physica D*, 163(1-2):26–48, 2002.

[95] D.M. Winterbottom, S.M. Cox, and P.C. Matthews. Pattern formation in a model of a vibrated granular layer. *SIAM J. Appl. Dyn. Syst.*, 7(1):63–78, 2008.

[96] P.D. Woods and A.R. Champneys. Heteroclinic tangles and homoclinic snaking in the unfolding of a degenerate reversible Hamiltonian–Hopf bifurcation. *Physica D*, 129(3-4):147–170, 1999.

[97] T.S. Yang. On traveling-wave solutions of the Kuramoto-Sivashinsky equation. *Physica D*, 110(1-2):25–42, 1997.

[98] T.S. Yang and T.R. Akylas. On asymmetric gravity–capillary solitary waves. *J. Fluid Mech.*, 330:215–232, 1997.

[99] A.V. Yulin and A.R. Champneys. Discrete snaking: multiple cavity solitons in saturable media. *SIAM J. Appl. Dyn. Syst.*, 9:391–431, 2010.

[100] A.V. Yulin and A.R. Champneys. Snake-to-isola transition and moving solitons via symmetry-breaking in discrete optical cavities. *Discrete and Continuous Dynam. Syst.*, 4(5):1341–1357, 2011.